University of São Paulo
"Luiz de Queiroz" College of Agriculture

Tropical landscape evolution and its relationship with paleosurfaces, Ferralsols and ferruginous duricrusts in the Alto Paranaíba region (Central Plateau, Minas Gerais State, Brazil)

Karina Patrícia Prazeres Marques

Thesis presented to obtain the degree of Doctor in Science.
Area: Soil and Plant Nutrition

Piracicaba
2021

Karina Patrícia Prazeres Marques
Geographer

Tropical landscape evolution and its relationship with paleosurfaces, Ferralsols and ferruginous duricrusts in the Alto Paranaíba region (Central Plateau, Minas Gerais State, Brazil)

versão revisada de acordo com a resolução CoPGr 6018 de 2011

Advisor:
Prof. Dr. **PABLO VIDAL TORRADO**

Thesis presented to obtain the degree of Doctor in Science.
Area: Soil and Plant Nutrition

Piracicaba
2021

Dados Internacionais de Catalogação na Publicação
DIVISÃO DE BIBLIOTECA – DIBD/ESALQ/USP

Marques, Karina Patrícia Prazeres

Tropical landscape evolution and its relationship with paleosurfaces, Ferralsols and ferruginous duricrusts in the Alto Paranaíba region (Central Plateau, Minas Gerais State, Brazil) / Karina Patrícia Prazeres Marques. - - versão revisada de acordo com a resolução CoPGr 6018 de 2011. - - Piracicaba, 2021.

123 p.

Tese (Doutorado) - - USP / Escola Superior de Agricultura “Luiz de Queiroz”.

1. Paisagens antigas 2. Pedogênese 3. Minerais secundários 4. Geocronologia de intemperismo I. Título

To my family for supporting my choices and cheering for my ascension,
I dedicate.

ACKNOWLEDGMENTS

To the graduate program of Soil and Plant Nutrition from the “Luiz de Queiroz” College of Agriculture/University of São Paulo (ESALQ/USP) for the opportunity and all the support during the Ph.D. course.

To the São Paulo Research Foundation (FAPESP) for providing my scholarship in Brazil (process number 2017/22292-4) as well as another (process number 2019/10708-7) to do an internship at the Sorbonne Université (Paris, France) during one year.

To the *L'Institut de Minéralogie, de Physique des Matériaux et de Cosmochimie* from the Sorbonne Université for having received me and all the support during my internship.

To my family, partner and friends for all the incentives and love.

To Prof. Dr. Pablo Vidal Torrado for all opportunities, support and encouragement. Thank you very much!

To Prof. Dr. Marcilene dos Santos for the valuable knowledge and contribution in the geomorphology and geology sections. My special thanks!

To Dr. Thierry Allard and Dr. Cécile Gautheron for the enthusiasm to work together, motivate me to move forward and for all the support during my internship in Paris.

To Dr. Giuditta Fellin for all her help with iron oxides dating and partnership in my project.

To Prof. Tiago Osório and Prof. Antônio Carlos Azevedo for all the conversations and incentive.

To Dr. Daniel Peifer and Prof. Dr. Clauzionor Silva for all their support in geomorphological analysis.

To Prof. Dr. Jairo Calderari and Elida Marina Nogueira for their support in mineralogical analysis.

To Benoît Baptiste, Ludovic Delbes, Rosella Pinna-Jame, Giullaume Morin, Jéssica Brest, Pierre Le Pape, Imène Esteve, Stéphanie Delbrel and Béatrice Doisneau for all support during my internship in France.

To my collegues and friends from France, Beatrix Heller, Camille Baya, Maximilien Mathian, Tiago da Silva, Pierre Lefebvre and Caroline Sanchez.

To my collegues and friends from ESALQ/USP, Daniela Schievano, Mariane Chiapini, Hermano Melo, Juliana Costa, Gabriela Silva, Márcia Dias, Marta Arruda, Thaís Pessoa, Taís Almeida, Sara Almeida, Julio Fernandes, Thairis Gomes and André Reis. I would like to thank also Matheus Coletti for his support with sample preparation and soil analysis.

To Dorival Grisotto, Paulo Pessotti and Alan Silveira for all the support during field campaigns, and Sônia Moraes, José Luis Vicente “Chiquinho”, Reginaldo Natalino Nogueira “Rossi”, Ednéia, Luiz Silva and José Roberto Santos “Zé” for the support in sample preparation and lab.

To all those who contributed to the accomplishment of this work.

"Life is not easy for any of us. But what of that?

We must have perseverance and above all confidence in ourselves.

We must believe that we are gifted for something and that this thing must be attained".

Marie Skłodowska-Curie

SUMMARY

RESUMO

Evolução da paisagem tropical e sua relação com paleosuperfícies, Latossolos e duricrusts ferruginosos na região do Alto Paranaíba (Planalto Central, Estado de Minas Gerais, Brasil)

Os Latossolos, também denominados como *Oxisols* e *Ferralsols*, ocorrem em paisagens antigas na zona intertropical. Eles são normalmente desenvolvidos em superfícies mais ou menos planas e em diferentes níveis de elevação, formados a partir de materiais de origem diversos. Apesar desses solos serem extensivamente estudados, várias questões permanecem pouco compreendidas sobre sua formação e evolução em paisagens tão antigas. Por isso, uma área com predominancia de Latossolos, incluindo duricrusts ferruginosos, no Planalto Central (Sudoeste do Estado de Minas Gerais, Brasil) foi selecionada para investigar a formação e evolução desses espessos solos intensamente intemperizados, e sua relação com a paisagem na qual ocorrem. A contextualização e compreensão dos fatores controladores responsáveis pela evolução da paisagem foi realizada (Capítulo 2) e, a partir desse entendimento geomorfológico, a seleção de locais para estudo de pedons representativos de Latossolos foi feita nas duas principais formas topográficas identificadas, sendo uma de cimeira e outra em nível intermediário. Amostragem sistemática alcançando vários metros de profundidade foi realizada e amostras foram coletadas em diferentes horizontes. Amostras do horizonte pisolítico de um duricrust ferruginoso subjacente a um dos pedons amostrados na superfície mais elevada e antiga foram detalhadamente investigadas quanto à sua mineralogia. Datação por (U-Th/He) foi realizada para restringir o tempo de formação e transformação de minerais secundários em estruturas pisolíticas, qual fornecem indícios para desvendar os principais períodos de intemperismo da área de estudo (Capítulo 3). Amostras dos horizontes não endurecidos foram analisadas em relação à sua composição química e características mineralógicas, incluindo propriedades cristalográficas e termais. As condições de intemperismo que prevaleceram durante sua formação foram discutidas considerando os diferentes fatores de formação (Capítulo 4).

Palavras-chave: Geomorfologia quantitativa, Paisagem reliquial, Pedogênese, Ferralitização, Mineralogia de argilas, Geocronologia de intemperismo

ABSTRACT

Tropical landscape evolution and its relationship with paleosurfaces, Ferralsols and ferruginous duricrusts in the Alto Paranaíba region (Central Plateau, Minas Gerais, Brazil)

Latossols, also known as Oxisols and Ferralsols, occur in ancient landscapes in the intertropical zone. They are usually developed on more or less flat surfaces, and at different elevation levels, developed from different parent materials. Although these soils have been extensively studied, several issues remain poorly understood about their formation and evolution in ancient landscapes. Therefore, an area with predominance of Ferralsols, including ferruginous duricrusts, in the Central Plateau (Southwest of the Minas Gerais State, Brazil) was selected to investigate the formation and evolution of thick highly weathered soils, and their relationship with the landscape in which they occur. The contextualization and understanding of the controlling factors responsible for the landscape evolution were carried out (Chapter 2) and, based on this geomorphological understanding, the selection of sites for the study of pedons representative of Ferralsols on the two main identified landforms was carried out, one at the summit and the other at an intermediate level. Systematic sampling reaching several meters deep was carried and samples were collected from different horizons. Samples of the pisolitic horizon from a ferruginous duricrust underlying one of the pedons sampled on the upper and older surface were thoroughly investigated for their mineralogy. (U-Th)/He dating was carried out to constrain the formation and transformation of pisolitic structures, which provide clues to unveil the main weathering periods of the study area (Chapter 3). Samples of the non-indurated horizons were analysed regarding to their chemical composition and mineralogical characteristics, including crystallographic and thermal properties. The weathering conditions that prevailed during their formation were discussed considering the different forming factors (Chapter 4).

Keywords: Quantitative geomorphology, Relict landscape, Pedogenesis, Ferralitization, Clay mineralogy, Weathering geochronology

1. INTRODUCTION

Paleosurfaces are preserved in the present-day landscape in most stable continental intraplate regions under humid and sub-humid tropical climate conditions as a result of slow denudation rate, relatively tectonic stability and stark lithological variability (e.g., Beauvais and Chardon, 2013; Monteiro et al., 2014; Beauvais et al., 2016; Vasconcelos et al., 2019). The remnants of the upper and older surfaces are covered by thick highly weathering profiles, including indurated horizons known as either Fe or Al duricrusts, which record the major weathering periods through time (Beauvais, 2009; Allard et al., 2018; Mathian et al., 2019; Jean et al., 2019). Despite its formation and transformation processes have been extensively studied in the last sixty years (Maignien, 1958; Alexander and Cady, 1962; McFarlane, 1976; Ambrosi and Nahon, 1986; Beauvais and Tardy, 1993; Bitom and Volkoff, 1993 and references therein), the constraints of distinct weathering periods remain dispersed (e.g., Bonnet et al., 2016; Vasconcelos et al., 2019; Allard et al., 2020). Therefore, several issues about the long and complex evolution of thick regoliths and their relation with the major paleoclimates and landscape evolution in the intertropical zone remain poorly understood.

The non-indurated horizons of the highly weathered profiles are recognised as ferralitic soils, lateritic soils, and *latéritique meuble*. In the broad sense, they may be classified as Oxisols (Soil Survey Staff, 2014), Ferralsols (IUSS Working Group WRB, 2015), or *Latossolos* (Santos et al., 2018). Although Ferralsols (term used hereinafter) and the underlying horizons are well known in tropical areas through the systematic description and analysis of profiles, several issues about them were not fully addressed, such as: (1) what are the controlling factors responsible for the development of distinct landforms in which Ferralsols are developed?; (2) what can thick soils including duricrusts reveal to us about the major weathering periods as well as the processes that have governed its evolution?; (4) how did the parent materials, topography, and length of time of the surface exposure to weathering agents influenced the characteristics and attributes of soils?; and (6) are Ferralsols developed under the present-day weathering conditions or different horizons from prevailing conditions coexist in the same profile?.

Concerning the Brazilian territory, the Central Plateau situated in the Neoproterozoic Brasília Belt, between São Francisco and Paranapanema Cratons, is an important area of Ferralsols with diverse underlying horizons developed on landforms at different elevation and parent materials (Curi and Franzmeier, 1984; Lepsch and Buol, 1986; Macedo and Bryant, 1987; Ferreira et al., 1999; Motta et al., 2002; Gomes et al., 2004; Reatto et al., 2008; Rolim

Neto et al., 2009). The extensive upper landform was recognised by King (1956) as *Sul-Americana Surface* (SAS; ~1,000 to 1,200 m), supposedly developed from the Upper Cretaceous to Oligocene, and the lower landform as *Velhas Surface* (VS), supposedly developed from the Neogene (King, 1956; Braun, 1971; Motta et al., 2002). The Ferralsols in the SAS are usually reported as developed from Cenozoic deposits with low or no genetic relationship with the underlying material (e.g., Motta et al., 2002; Marques et al., 2004; Reatto et al., 2008). However, many studies have been carried out in the first two meters of very thick soils and thus several issues could remain oversimplified. In addition, other evidence about its origin has not been fully investigated, such as from the degradation of ferruginous duricrusts, which is widely observed in other intertropical zones (e.g., Beauvais and Nahon, 1985; Bilong et al., 1992; Beauvais, 2009; Bitom et al., 2003) or even from the underlying bedrock, although the indications of genetic affiliation can be obliterated due to the intense weathering. Regarding to the soils developed in the lower landscape position, some studies (e.g., Motta et al., 2002; Reatto et al., 2008; Rolim Neto et al., 2009) pointed out that there is an influence of the mixture of pre-weathered material from the upper landform with the contribution of the weathering of the underlying bedrock in the soil formation. However, further studies are still needed to assess whether the contribution of the transported material is generalised and whether there are soils developed exclusively from the underlying bedrock.

It is expected that with the present thesis a contribution to some of the main issues and clues for future investigations can be provided. Therefore, the main objective of the thesis is to investigate the hidden history of an ancient landscape and their related soils. To achieve this purpose, the Quebra-Anzol catchment was chosen as the study area, due to be the largest (~10,600 km²) complete catchment in the Alto Paranaíba region (Minas Gerais State, Brazil). The thesis was structured in three chapters covering from a macro-regional to a detailed scale. The macro-regional scale is related to a detailed geomorphological study through the analysis of various topographic metrics in order to investigate the landscape evolution (Chapter 2). After geomorphological contextualization and interpretation, a ferruginous duricrust profile belongs to the upper landform (~1,100 m elevation) was chosen and their pisolitic facies was sampling for mineralogical characterization of supergene phases on undisturbed grains prior to dating the same grains by (U-Th)/He method. The results of (U-Th)/He dating unveil the weathering periods related to the formation and transformation of secondary minerals from the pisolitic facies of the ferruginous duricrust developed on the upper surface. The older and upper paleosurface and Ferralsols are developed under ferruginous duricrusts profiles, and thus such surface is at least the same age as ferruginous duricrust, suggesting that Ferralsols may have

been developed since the Oligocene (Chapter 3). In addition, eight sites for studies at scale of soil profiles were selected on two landforms at different elevations and parent materials. Trenches were excavated with a hydraulic excavator, reaching up to 10 meters for the soils on the upper landform and half for soils on the lower landform, and then soil description and sampling were carried out on the field. Thereafter, samples of all soils were investigated concerning their chemical characteristics and mineralogy of clay fraction, including crystallographical and thermal properties, in order to compare and discuss the pedogenetic processes responsible for the formation and transformation of Ferralsols on different conditions (Chapter 4).

References

Alexander, L.T., Cady, J.G., 1962. Genesis and hardening of laterite in soils (Technical Bulletin No. 1282). Washington, DC: Soil Conservation Service.

Allard, T., Gautheron, C., Riffel, S.B., Balan, E., Soares, B.F., Pinna-Jamme, R., Derycke, A., Morin G., Bueno, G.T., Nascimento, N., 2018. Combined dating of goethites and kaolinites from ferruginous duricrusts. Deciphering the Late Neogene erosion history of Central Amazonia. Chemical Geology 479, 136-150.

Allard, T., Pereira, L., Mathian, M., Balan, E., Bueno, G.T., Falguères, C. Nascimento, N., 2020. Dating kaolinite from the Neogene Içá Formation and overlying laterites, central Amazonia, Brazil: Constraints for a stratigraphic correlation. Palaeogeography, Palaeoclimatology, Palaeoecology 554, 109818.

Ambrosi, J.P., Nahon, D., Herbilon, A.J., 1986. The epigenetic replacement of kaolinite by hematite in laterite. Petrographic evidence and the mechanisms involved. Geoderma 37, 283-294.

Beauvais A., Nahon, D., 1985. Nodules et pisolites de dégradation des profils d'altération manganéslfères sous conditions latéritiques. Exemples de Côte d'Ivoire et du Gabon / Nodules and pisolites from manganlferous weathering profiles under lateritic influences. Examples from Ivory Coast and Gabon. Sei. Géol., Bull. 38, 359-381.

Beauvais, A., 2009. Ferricrete biochemical degradation on the rainforest–savannas boundary of Central African Republic. Geoderma 150, 379–388.

Beauvais, A., Bonnet, N.J., Chardon, D., Arnaud, N., Jayananda, M., 2016. Very long-term stability of passive margin escarpment constrained by $^{40}Ar/^{39}Ar$ dating of K-Mn oxides. Geology 44, 299–302.

Beauvais, A., Chardon, D., 2013. Modes, tempo, and spatial variability of Cenozoic cratonic denudation: The West African example. Geochemistry, Geophysics, Geosystems 14, 1590-1608.

Beauvais, A., Tardy, Y., 1993. Degradation and dismantling of iron crusts under climatic changes in Central Africa. Chemical Geology 107, 277-280.

Bilong, P., Belinga, S.E., Volkoff, B., 1992. Séquence d'évolution des paysages cuirassés et des sols ferrallitiques en zones forestières tropicales d'Afrique centrale. Place des sols à horizons d'argile tachetée. C. R. Acad. Sci. Paris 314, 109-115.

Bitom, D., Volkoff, B., 1993. Altération déferruginisante des cuirasses massives et formation des horizons gravillonnaires ferrugineux dans les sols de l'Afrique Centrale humide. C. R. Acad. Sci. Paris 316, 1447-1454.

Bitom, D., Volkoff, B., Abossolo-Angue, M., 2003. Evolution and alteration in situ of a massive iron duricrust in Central Africa. Journal of African Earth Sciences 37, 89–101.

Bonnet, N.J., Beauvais, A., Arnaud, N., Chardon, D., Jayananda, M., 2016. Cenozoic lateritic weathering and erosion history of Peninsular India from $^{40}Ar/^{39}Ar$ dating of supergene K–Mn oxides. Chemical Geology 446, 33–53.

Braun, O.P.G., 1971. Contribuição à geomorfologia do Brasil Central. Revista Brasileira de Geografia 32, 3–39.

Curi, N., Franzmeier, D.P., 1984. Toposequence of Oxisols from the Central Plateau of Brazil. Soil Sci. Soc. Am. J. 48, 3411-346.

Ferreira, M.M., Fernandes, M., Curi, N., 1999. Mineralogia da fração argila e estrutura de Latossolos da região sudeste do Brasil. R. Bras. Ci. Solo 23, 507-514.

Gomes, J.B.V., Curi, N., Schulze, D.G., Marques, J.J.G.S.M., Ker, J.C., Motta, P.E.F., 2004. Mineralogia, morfologia e análise microscópica de solos do bioma cerrado. R. Bras. Ci. Solo, 28, 679-694.

IUSS Working Group WRB. 2015. World Reference Base for Soil Resources 2014, update 2015. International soil classification system for naming soils and creating legends for soil maps. World Soil Resources Reports No. 106. FAO, Rome.

Jean, A., Beauvais, A., Chardon, D., Arnaud, N., Jayananda, M., Mathe, P.E., 2019. Weathering history and landscape evolution of Western Ghats (India) from $^{40}Ar/^{39}Ar$ dating of supergene K–Mn oxides. Journal of the Geological Society 23, 523-536.

King, L.C., 1956. A geomorfologia do Brasil oriental. Rev. Bras. Geogr. 18, 147–266.

Lepsch, I.F., Buol, S.W., 1988. Oxisol-landscape relationships in Brazil, in (F. H. Beinroth, M., N. Camargo, M.N., Eswaran, H. (Eds.), Proceedings of the Eighth International Soil Classification Workshop, Brazil. Part 1: Papers. Soil Management Support Services, U.S. Dep. Agric., Washington, DC, pp. 174-189.

Macedo, J., Bryant, R.B., 1987. Morphology, Mineralogy, and Genesis of a hydrosequence of Oxisols in Brazil. Soil Sci. Soc. Am. J. 51, 690-698.

Maignien, R., 1958. Contribution a l'étude du cuirassement des sols en Guinée française. State doct. thesis. Fac. Sci. Strasbourg.

Marques, J.J., Schulze, D.G., Curi, N., Mertzman, S.A., 2004. Major element geochemistry and geomorphic relationships in Brazilian Cerrado soils. Geoderma 119, 179-195.

Mathian, M., Aufort, J., Braun, J., Riotte, J., Selo, M., Balan, E., Fritsch, E., Bhattacharya, S., Allard, T., 2019. Unraveling weathering episodes in Tertiary regoliths by kaolinite dating (Western Ghats, India). Gondwana Research 69, 89-105.

McFarlane, M.J., 1976. Laterite and Landscape. Academic Press, London.149p.

Monteiro, H.S., Vasconcelos, P.M.P., Farley, K.A., Spier, C.A., Mello, C.L., 2014. (U-Th)/He geochronology of goethite and the origin and evolution of cangas. Geochimica et Cosmochimica Acta 131, 267–289.

Motta, P.E.F., Carvalho Filho, A., Ker, J.C., Pereira, N.R., Carvalho Junior, W., Blancaneaux, P., 2002. Relações solo-superfície geomórfica e evolução da paisagem em uma área do Planalto Central Brasileiro. Pesquisa Agropecuária Brasileira 37, 869–878.

Reatto, A., Bruand, A., Martins, E.S., Muller, F., Silva, E.M., Carvalho Jr., O.A., Brossard, M., 2008. Variation of the kaolinite and gibbsite content at regional and local scale in Latosols of the Brazilian Central Plateau. C. R. Geoscience 340, 741–748.

Rolim Neto, F.C., Schaefer, C.E.G.R., Fernandes Filho, E.I., Corrêa, M.M., Costa, L.M., Parahyba, R.B.V., Guerra, S.M.S., Heck, R., 2009. Topolitossequências de solos do Alto Paranaíba: atributos físicos, químicos e mineralógicos. Revista Brasileira de Ciência do Solo 33, 1795-1809.

Santos, H.G., Jacomine, P.K.T., Anjos, L.H.C., Oliveira, V.A., Lumbreras, J.F., Coelho, M.R., Almeida, J.A., Araújo Filho, J.C., Oliveira, J.B., Cunha, T.J.F., 2018. Sistema Brasileiro de Classificação de Solos, fifth ed. Embrapa Solos, Rio de Janeiro.

Soil Survey Staff, 2014. Keys to Soil Taxonomy, 12th ed. USDA National Resources Conservation Services, Washington DC.

Vasconcelos, P.M., Farley, K.A., Stone, J., Piacentini, T., Fifield, L.K., 2019. Stranded landscapes in the humid tropics: Earth's oldest land surfaces. Earth and Planetary Science Letters 519, 152–164.

2. TRANSIENT AND RELICT LANDFORMS IN A LITHOLOGICALLY HETEROGENEOUS POST-OROGENIC LANDSCAPE IN THE INTERTROPICAL BELT (ALTO PARANAÍBA REGION, BRAZIL)

ABSTRACT

High elevations and steep slopes are currently observed in ancient mountain ranges despite active tectonics having ceased tens to hundreds of millions of years ago. Explanations for landscape dynamics in these settings generally postulate that post-orogenic relief is either the product of a recent topographic rejuvenation episode (or episodes) or was formed by ancient orogenesis after which the landscape has survived ever since, perhaps in a topographic equilibrium condition where erosion is spatially uniform. Here, we explore the morphology of a tropical wet and dry, high relief post-orogenic landscape in the Brazilian continental interior capped by ferruginous duricrusts and characterised by stark lithological variability. We explore whether a decline in relief has remained constant or increased during its post-orogenic evolution. We show that river knickpoints demarcate regional topographic transitions between 1) flat, relict uplands, 2) a rugged transition zone where channels and adjacent hillslopes are steep, and 3) gentle lowland morphologies in downstream areas. Relict areas are primarily capped by ferruginous duricrusts that are likely Eocene, as suggested by weathering geochronology in surrounding areas. Topography in the study area records at least two regional, transient topographic disequilibrium events, where the oldest drop in relative base level is expressed by knickpoints lying in high elevations fixed within ferruginous duricrusts that slow the propagation of the transient base level lowering signal. This transience is consistent with regional uplift events, likely driven by denudational isostatic rebound or compressional far-field stresses, with local effects superimposed linked with the strike-slip reactivation of old faults and the formation of the Pratinha Pull-Apart Basin. Relief is growing as the topography is slowly decaying, yet the topographic configuration of the area was established before these disequilibrium events. Our study demonstrates that ancient and younger landforms coexist in a post-orogenic setting, implying that the competing hypotheses for post-orogenic development are not mutually exclusive.

Keywords: Topographic rejuvenation, Ferruginous duricrust, Quantitative geomorphology, Knickpoints.

2.1. Introduction

Topographic equilibrium, a condition where topographic forms are constant through time because erosion everywhere equals tectonic uplift irrespective of lateral variations in rock type or relief, is generally expected where boundary conditions are constant or changed extremely slowly over millions of years (Hack, 1960; Howard, 1965). However, a complete

topographic equilibrium is likely never achieved in nature (Willett and Brandon, 2002). Reasons for this include 1) the complexity of tectonic displacement, which has vertical and horizontal components (e.g., Willett et al., 2001); 2) the nature of most surface processes, which occur as discrete events (e.g., Montgomery, 2001); and, 3) mainly, the tectonic and climatic conditions imposed on a landscape vary over a range of timescales, implying that boundary conditions are unlikely to remain unchanged over long timespans (e.g., Whipple, 2001). Nonetheless, various authors argue that convergent mountain belts such as in Taiwan, New Zealand, or the Olympic Mountains (NW USA), achieved a topographic equilibrium or a less strict topographic quasi-steady state, where one may observe within a relevant time frame the steadiness of the mean elevation (e.g., Suppe, 1981; Pazzaglia and Brandon, 2001).

In intraplate landscapes where convergent tectonics ceased tens to hundreds of millions of years ago, referred to as "post-orogenic" landscapes, boundary conditions tend to be steady or change very slowly through time. The topographic equilibrium concept was defined in the context of one such post-orogenic landscape, the Appalachian Mountains (Hack, 1960), and various post-orogenic mountains were interpreted afterwards to be in topographic equilibrium or quasi-steady state. Examples include the Namibian highlands (e.g., Bierman and Caffee, 2001), the Appalachians (e.g., Matmon et al., 2003), the Cape Mountains (e.g., Scharf et al., 2013) and other areas in South Africa (e.g., Chadwick et al., 2013; Heimsath et al., 2020), and the Western Ghats (e.g., Mandal et al., 2015). Supporting this hypothesis are, generally, morphometric observations that topographic forms are adjusted to rock strength, with steep topography in resistant units and gentle morphologies in more erodible units these being characterised by smooth, concave-upward river profiles unless disrupted by lithological boundaries, and geochronological data which shows the steadiness of erosion rates over time and across the landscape (e.g., Bierman and Caffee, 2001; Matmon et al., 2003; Scharf et al., 2013; Mandal et al., 2015). However, rock uplift is necessary to maintain equilibrium (Hack, 1975), making the equilibrium hypothesis problematic for tectonically stable landscapes, although equilibrium may be driven by denudational isostatic rebound (e.g., Hack, 1975; Matmon et al., 2003; Mandal et al., 2015). In contrast, a range of empirical constraints including thermochronological, cosmogenic, topographic, and sedimentary data record variations in erosion rates in space and time in various post-orogenic settings, which is generally interpreted as an episode or episodes of topographic rejuvenation long after cessation of crustal thickening (e.g., Hack, 1982; Quigley et al., 2007; Cogné et al., 2012; Gallen et al., 2013; Miller et al., 2013; Gallen, 2018; van Ranst et al., 2020). This topographic rejuvenation hypothesis implies a geomorphic differentiation whereby rivers and hillslopes responding to the rejuvenation are

associated with coupled increasing relief and higher erosion rates (e.g., Gallen et al., 2013), supporting thus a view of an unsteady post-orogenic evolution (Tucker and van Der Beek, 2013; Gallen, 2018).

Nevertheless, there is compelling geochronological and geomorphic evidence that large areas of post-orogenic landscapes are of considerable antiquity, particularly in slowly eroding humid tropical areas in Australia, Africa, India and South America (e.g., Twidale, 1976; Beauvais and Chardon, 2013; Monteiro et al., 2014; Beauvais et al., 2016; Bonnet et al., 2016; Vasconcelos et al., 2019). These ancient areas commonly refer to low-relief uplands capped by highly weathered profiles, including duricrusts containing iron oxides (e.g., hematite and goethite), K-Mn oxides or aluminium hydroxides (e.g., gibbsite) as their principal constituent. Supergene mineral dating in these profiles documents intense chemical weathering-initiated tens of millions of years ago, resulting in the formation of chemically and physically resistant duricrusts, likely exposed subaerially continuously over a long period (e.g., Beauvais et al., 2016; Bonnet et al., 2016; Monteiro et al., 2018; Vasconcelos and Carmo, 2018). These discontinuous low-relief uplands have often been interpreted as remnants of a pre-existing, roughly continuous ancient surface with a continental extent, not much different from a classical planation surface, that later undergone some form of episodic rock uplift, surviving in high elevations principally due to the exposure of resistant bedrocks and a relative tectonic quiescence (e.g., Twidale, 1976; Monteiro et al., 2014; Bonnet et al., 2014; Vasconcelos and Carmo, 2018; Vasconcelos et al., 2019).

These examples demonstrate the lack of consensus on how landscapes that are not experiencing continuing tectonically-driven rock uplift evolve over long timescales (cf., Bishop, 2007). We focus on this issue in this contribution, and we perform a quantitative study of the topography of a tropical wet and dry, ancient landscape located deep in the continental interior that last experienced active tectonics ~80 Ma, to test whether its current morphology shows topographic characteristics that are either signatures of landscapes in equilibrium or landscapes that have undergone topographic rejuvenation. We focus on the spatial distribution of knickpoints and potential relationships with upstream low-relief upland areas and downstream steepened river segments and adjacent hillslopes. We examine this question in the context of the Alto Paranaíba Uplift (APU), a lithologically heterogeneous post-orogenic setting located in what is considered the least seismically active stable continental region in the world, the Brazilian Platform (Johnston et al., 1994; Schulte and Mooney, 2005; Talwani, 2014). We explore whether spatial patterns in topography are related to variations in bedrock lithology, and, in particular, we investigate how ferruginous duricrusts, which we define

coupling imagery analysis and fieldwork mapping, are related to the APU's topographic configuration.

2.2. Geomorphological and geological setting

The study area is located in the APU, an Upper Cretaceous tectonic feature along the Az 125º Lineament (Moraes Rocha et al., 2019) associated with the opening of the Atlantic Ocean and embedded within a "dead" Neoproterozoic orogen that has been tectonically stable since the Early Paleozoic (~460 Ma) (Fonseca et al., 2021), referred to as the Brasília Orogenic Belt, forming a still topographically prominent landscape (Fig. 1a). The APU is located between two Proterozoic cratons, the São Francisco and the Paranapanema cratons, and the Brasília Belt is bound to the Paranapanema craton by the Itumbiara Suture (Fig. 1b). Topographically the APU lies on the highlands of the Central Plateau, dividing two of the largest Brazilian catchments, the São Francisco and Paraná catchments. The major river flowing through the APU is the Paranaíba River (Minas Gerais State, Brazil), the northernmost tributary of the Paraná River.

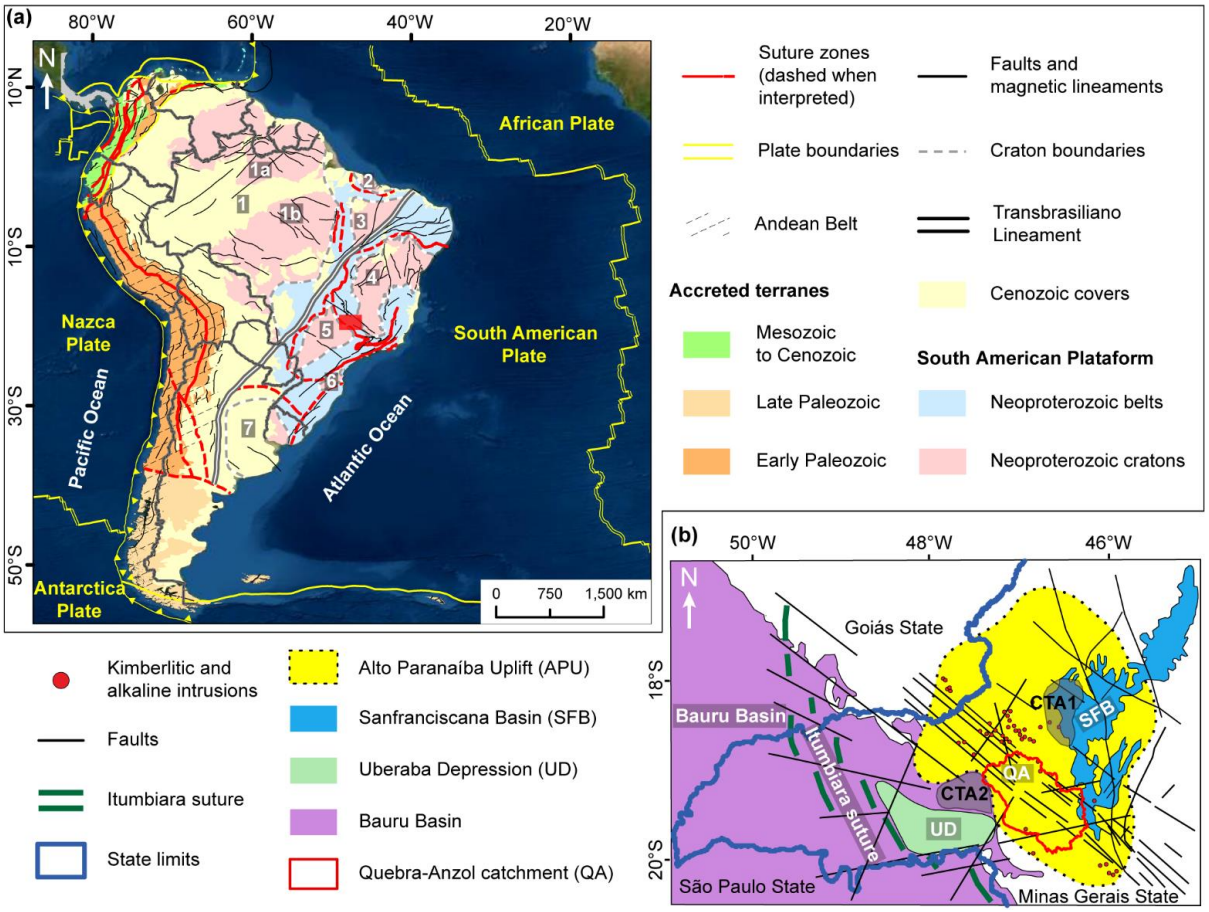

Figure 1. Geological framework of the study area. (a) Simplified tectonic framework of the South American Platform. (b) Sketch representing the geological context of the Alto Paranaíba Uplift (APU). The red rectangle in panel (a) indicates the location of (b). Cratons: 1 = Amazon Craton; 1a = Guyana Shield; 1b = Central Brazil Shield; 2 = São Luis Craton; 3 = Paranaíba block; 4 = São Francisco Craton; 5 = Paranapanema Craton; 6 = Luis Alves Craton; 7 = Rio de La Plata Craton. CTA1 = Abaeté Depression; CTA2 = Perdizes Depression. Adapted from Hasui and Haralyi (1991), Batezelli (2003) and Cordani et al. (2016).

This study investigated the Quebra-Anzol (QA) catchment, which is the largest (~10,600 km²) complete catchment in the APU, located in the axis of this Upper Cretaceous tectonic feature, and a large tributary of the Araguari River on the left side of the Paranaíba River. Elevation ranges from 535 to 1,427 m in the QA catchment and surrounding areas, with a mean elevation of 986 m (Fig. 2). The landscape is characterised by an upstream area of high elevation (with elevations > 986 m) surrounding the regional drainage divides defined by the QA interfluves, and downstream areas with gentle relief, at valley bottoms (Fig. 2). The climate is Aw (Köppen–Geiger's classification), characterised by warm and seasonally dry winters and moist and warm summers, with an average annual rainfall of 1,600 mm and a mean annual temperature of 22 °C (Oliveira et al., 2020).

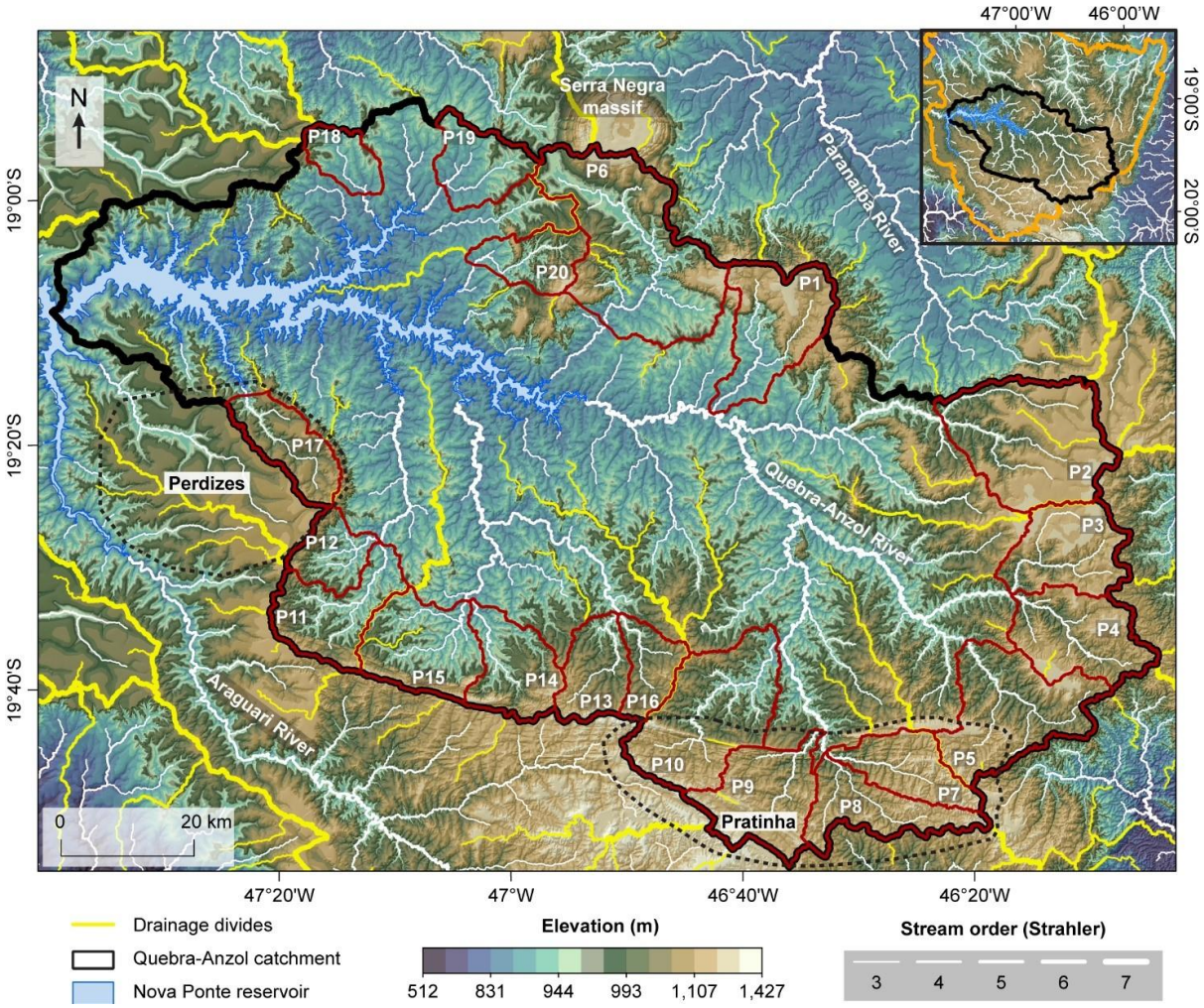

Figure 2. Elevation in the QA catchment and surrounding areas. Drainage divide segments were extracted using the "DIVIDEobj" algorithm in TopoToolbox, and the line width is proportional to the divide segment order, similar to stream order, computed using the "topo" method (Scherler and Schwanghart, 2020). Note that this divide segment sorting helps to visualise the topographic configuration in the region. Polygons in dark red, identified as P1-P20, represent fourth-order catchments for which we show long profiles in χ-elevation space in Fig. 11. Black dotted lines represent the limits of the Perdizes and Pratinha sectors. The inset map shows the topographic configuration of the APU region (orange lines).

The bedrock of the QA region is complex and spatially variable, including metamorphic, crystalline, volcanic, and sedimentary units (Fig. 3). The oldest units exposed are Neoproterozoic metamorphic rocks and local granites arranged in sub-vertical boundaries. Diamond-bearing kimberlites and alkaline intrusions from the Upper Cretaceous (e.g., Serra Negra, Salitre I and II and Tapira) related to the Alto Paranaíba Igneous Province crop out, following the NW-SE structural trend of the Az 125º Lineament (Moraes Rocha et al., 2019), forming an important province of mineral extraction (e.g., Riccomini et al., 2005). The APU acted as a source area supplying distributive fluvial sediments to the Sanfranciscana Basin to the northeast, and the Bauru Basin to the southwest (Sgarbi and Dardenne, 1996; Batezelli,

2017; Batezelli et al., 2019). These occur as sub-horizontal sedimentary deposits that overlie the Neoproterozoic and the volcanic units locally (Hasui and Haralyi, 1991; Riccomini, 1997).

The study area is thus characterised by substantial lithological variability, with lithologies ranging from Neoproterozoic (Tonian units: phyllites, schists, quartzites, banded iron formations; Cryogenian units: schists and leucogranites; and Ediacaran units: metapelites and schists) to Mesozoic (basalts, alkaline intrusions, conglomerates, sandstones and pelites) (Fig. 3). A wide compositional range is also present, with different secondary mineral compositions for metasediments or the alternation of coarse- and fine-grained beds cemented by iron or calcium carbonate for Upper Cretaceous sequences. For instance, sericite and carbonaceous phyllites intercalate with quartzites and mica quartzites, calcischists alternate with chlorite and mica schists, and conglomerates intercalate with sandstones, siltstones and shales of different compositions and variably affected by ferruginous duricrusts.

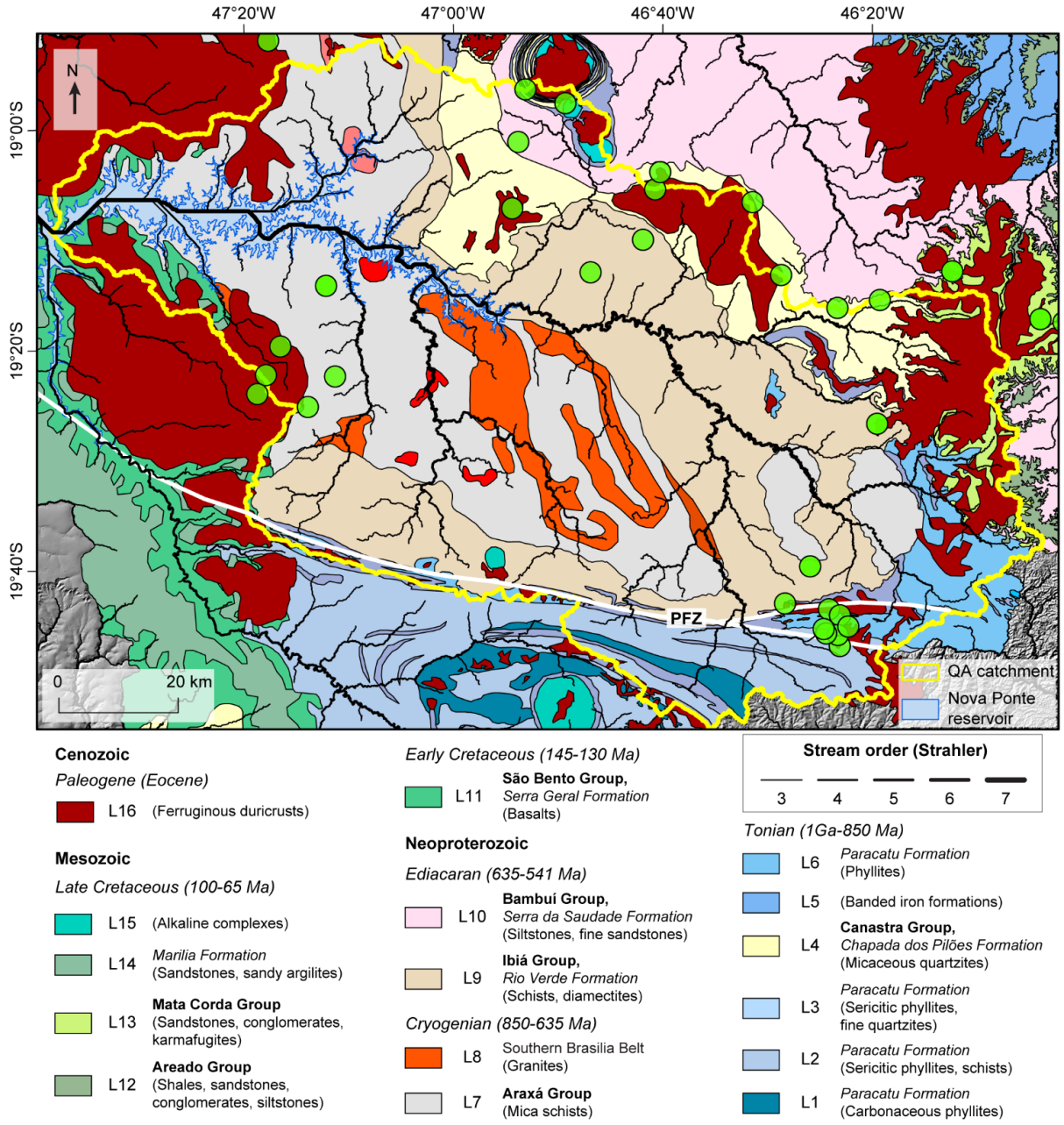

Figure 3. Simplified geological units exposed in the study area. Lithological units were adapted from CPRM (2014), classified based on age and composition. Green circles show locations we visited in the field to validate our mapping of *in situ* ferruginous duricrusts (see section 3.3). Thick white lines represent the Pratinha Fault Zone (PFZ).

The late phase of the volcanic-magmatic event related to the rifting, associated with the alkaline intrusions (e.g., Riccomini et al., 2005), was defined as Upper Cretaceous to Paleocene through apatite fission-track thermochronological data (Fonseca et al., 2021). A period of tectonic quiescence and seasonal wet and warm climate likely followed this phase, which is generally inferred from the formation of extensive surfaces capped by thick weathering profiles, including ferruginous duricrusts (Macedo and Bryant, 1987; Motta et al., 2002),

affecting the distributive fluvial sequences of the Upper Cretaceous Basins. Various authors have argued that remnants of these extensive surfaces have survived subaerially as low-relief uplands in the APU region, often interpreted in the study area as a relict of Lester King's Sul-Americana Surface (e.g., King, 1956; Braun, 1971), allegedly from the Upper Cretaceous to Oligocene, though without geochronological data supporting such an age range.

2.3. Methods

Erosion processes are known to be more effective when the topography is steeper, and high relief and steep slopes correlate with rapid erosion rates on a global scale (Ahnert, 1970; Montgomery and Brandon, 2002; Portenga and Bierman, 2011; Kirby and Whipple, 2012; Harel et al., 2016). Spatial variations in topography have thus been widely used to investigate geomorphic evolution in erosive settings (e.g., Wobus et al., 2006; Bishop and Goldrick, 2010; Kirby and Whipple, 2012; Gallen et al., 2013). Here, we used a seamless Copernicus (COP-30) digital elevation model (DEM) with a spatial resolution of 30 m and a vertical accuracy of <2 m for the APU region (AIRBUS, 2020) to extract local relief, hillslope angle, and normalised channel steepness in the study area, and to perform knickpoint and stream profile analysis, exploring potential links with lithological variability. Other reasonable choices of topographic data were not used because the vertical accuracy of the SRTM (Shuttle Radar Topography Mission) 30 m DEM is considerably worse (~9-12 m) as described in its specification (Rodriguez et al., 2005), while the ALOS (Advanced Land Observation Satellite) 30 m DEM is not complete in the region. The COP-30 DEM was downloaded from OpenTopography (https://opentopography.org/) and projected to WGS84 UTM Zone 23S.

2.3.1. Extraction of topographic metrics

A large body of geomorphic work has attempted to detect signatures of tectonic, climatic, and lithologic forcing in the morphology of river profiles (e.g., Wobus et al., 2006; Bishop and Goldrick, 2010; Kirby and Whipple, 2012; Gallen et al., 2013). Most of these studies build on the common empirical observation that channel slope (S) decreases along a stream profile with a downstream increase in drainage area (A) following a power-law relationship (e.g., Hack, 1957; Flint, 1974):

$$S = k_s A^{-\theta} \quad (1)$$

where θ is a dimensionless coefficient that describes how concave the channel profile is, with higher θ values determining that S decreases more rapidly with a downstream increase in A, and k_s is the local channel slope normalised by the upstream drainage assuming a reference value of θ.

The extraction of k_s values from a DEM depends on the choice of θ, and recent work demonstrated that θ might vary substantially in erosive landscapes (Mudd et al., 2018). The standard approach to analyse channel steepness data is to define a reference value of θ from which one computes normalised k_s values commonly referred to as k_{sn} (Kirby and Whipple, 2012). Empirical studies in various tectonic settings have demonstrated that k_{sn} is positively correlated with long-term channel erosion rates (e.g., DiBiase et al., 2010; Mandal et al., 2015; Harel et al., 2016), and spatial patterns in k_{sn} are generally expected to reflect variations in rock uplift, lithology or climate conditions (Kirby and Whipple, 2012).

We used the "integral method" of river profile analysis to extract k_{sn} (Perron and Royden, 2013). This method allows computation of k_{sn} without extracting values of local channel slope, resulting in k_{sn} estimates that are less affected by topographic noise (Perron and Royden, 2013). The integral method involves replacing S with dz/dx in Eq. 1, where z is channel bed elevation and x is distance along the profile, moving dx to the right-hand side of the equation, and integrating the equation in the upstream direction from an arbitrary base level at the position x_b in the profile, resulting in:

$$z(x) = z(x_b) + \left(\frac{k_s}{{A_0}^{\theta}}\right) \int_{x_b}^{x} \left(\frac{A_0}{A(x)}\right)^{\theta} dx, \quad (2)$$

where A_0 is a reference drainage area introduced to make the area term (i.e., $A_0/A(x)$) dimensionless. From Eq. 2, we can define an integral quantity χ with dimensions of length:

$$\chi = \int_{x_b}^{x} \left(\frac{A_0}{A(x)}\right)^{\theta} dx. \quad (3)$$

The angular coefficient of a river profile in χ-elevation space is k_{sn} if A_0 = 1 m^2 and the χ-transformation of the profile is based on a reference value of θ. Rivers in equilibrium flowing through areas with uniform rock uplift and bedrock erodibility are linear in χ-elevation space if the choice of the reference value of θ is adequate (Perron and Royden, 2013; Mudd et al., 2014, 2018). In contrast, spatial variations in rock uplift or bedrock erodibility should result in stark spatial contrasts in k_{sn}, and hence in channel erosion rates, which is generally expected

to be expressed as inflexions in χ-elevation space (Perron and Royden, 2013; Mudd et al., 2014, 2018).

The downstream end of the study area's river network features the Nova Ponte reservoir, a large reservoir with an area of 428 km^2 built-in 1987 (Silva, 2017). The COP-30 DEM includes flattening of water bodies (AIRBUS, 2020), and hence the entire reservoir exhibits 805 m of elevation. We set a minimum elevation of 830 m for performing river profile analysis, which determined that this arbitrary base level is located ~1 km upstream from the reservoir, thus avoiding artefacts related to its neighbouring areas (Fig. 4).

We estimated how θ varies in the landscape by calculating the best-fit value of θ for all complete, non-nested catchments in the region with an area ≥10 km^2, upstream from the 830 m base level (n = 171), extracted using functions implemented in TopoToolbox (Schwanghart and Scherler, 2014) and the TAK addon (Forte and Whipple, 2019). We used the "mnoptimvar" algorithm in TopoToolbox, which employs the disorder method (Hergarten et al., 2016), to estimate θ for each of these catchments. The mean θ value for the entire landscape is 0.468 (with a standard deviation of 0.138), close to the commonly used value of θ = 0.45 (e.g., Kirby and Whipple, 2012; Mandal et al., 2015), and thus we quantified k_{sn} and χ using 0.45 as our reference value of θ. We calculated k_{sn} for all channel segments upstream from the 830 m base level using the "KsnChiBatch" function in TAK. For that, we extracted the river network using a minimum contributing area of 1 km^2, smoothed k_{sn} measures using a window of 300 m, and used "trib" as our calculation method because it computes k_{sn} for each channel segment separately, which is recommended for segments adjacent to the 830 m base level (Forte and Whipple, 2019).

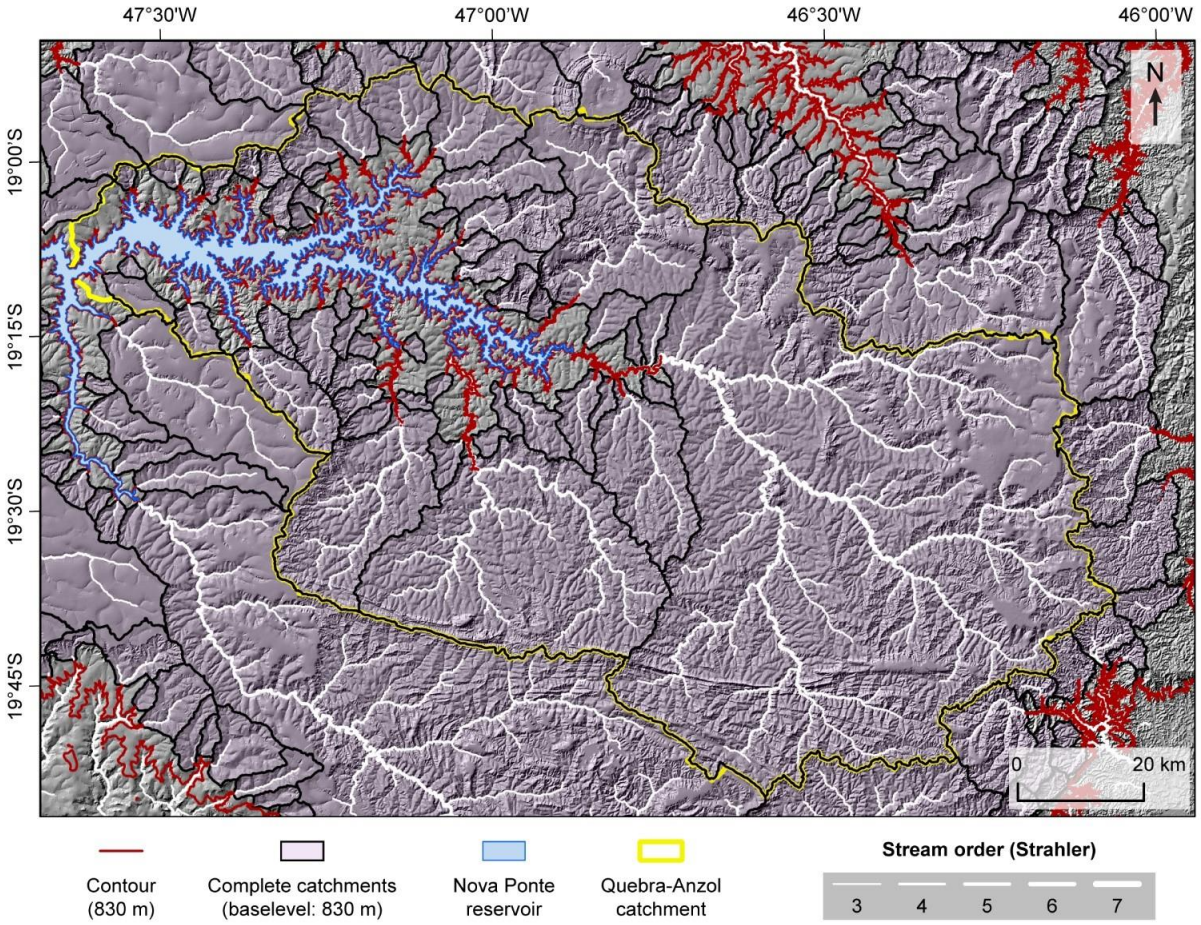

Figure 4. Complete catchments in the region, upstream of the 830 m base level, with an area greater than 10 km², draped over a hillshade image. Note that every river in the study area has headwaters at elevations ≥830 m transitioning downstream to such an elevation. Non-nested catchments were extracted using the "ProcessRiverBasins" function in TAK (Forte and Whipple, 2019).

Local relief and hillslope angle are two others commonly used topographic metrics to explore patterns in uplift, climate conditions and lithology from topographic data, mainly because they are positively correlated with erosion rates (e.g., Ahnert, 1970; Montgomery and Brandon, 2002; Portenga and Bierman, 2011). Local relief is the range in elevation within an area generally defined by a circular window. We computed local relief with window diameters varying from 0.5, 1-7 km using the "localtopography" algorithm in TopoToolbox to estimate the optimal window of local relief for the study area. Following previous studies (e.g., DiBiase et al., 2010; Peifer et al., 2021), we computed catchment-averaged values of local relief, calculated using different windows, and mean k_{sn} values for all catchments used to estimate the best-fit value of θ. Mean values of local relief computed with a circular window of 5 km of diameter were best correlated with mean k_{sn}, defining the 5 km diameter window as the optimal local relief in this study. Hillslope angle was extracted using the "gradient8" algorithm in TopoToolbox.

We investigated how topographic metrics vary as a function of lithology by computing descriptive statistics for how elevation, local relief, hillslope angle, and k_{sn} are distributed per lithological units adapted from CPRM (2014), classified based on age and composition (Fig. 3). Although we do not have quantitative data on rock strength, we used the approximate rock strength classification of Selby (1993) and Goudie (2006) to separate the exposed lithologies into relative rock strength classes (Tab. 1).

Tabela 1. Approximate strength classification of rock units exposed in the study area and respective geological information

Age (Ma)	Unit[1]	Lithology	Rock strength[2]
		Cenozoic	
70 - 48[3]	L16	Ferruginous duricrusts	Very strong
		Mesozoic	
	L15	Alkaline intrusions	Very strong
	L14	Sandstones and argillites	Moderately strong
	L13	Sandstones, conglomerates and lavas	Very strong
130 - 65	L12	Pelites and cemented clastics sediments	Very strong
145 - 130	L11	Basalts	Very strong
		Neoproterozoic	
	L10	Siltstones and fine sandstones	Weak
635 - 541	L09	Schists and secondary phyllites	Weak
	L08	Granites	Weak
850 - 635	L07	Mica schists	Weak
	L06	Phyllites	Weak
	L05	Banded iron formations	Very strong
1,000 - 850	L04	Micaceous quartzites	Very strong
	L03	Sericite phyllites and fine quartzites	Very strong
	L02	Sericite phyllites and schists	Weak
	L01	Carbonaceous phyllites	Weak

[1] Geological units adapted from CPRM (2014) (Fig. 3).
[2] Relative rock strength classification according to Selby (1993) and Goudie (2006).
[3] According to weathering geochronological data in surrounding areas (e.g., Monteiro et al., 2014; Monteiro et al., 2018; Vasconcelos and Carmo, 2018; Vasconcelos et al., 2019).

2.3.2. Knickpoint and river profile analysis

River networks generally respond to variations in prevalent tectonic, climatic or lithologic conditions by adjusting local channel slope in the proximity of the relative base level, which can be a confluence, an active structural boundary or the sea level (Kirby and Whipple, 2012). A knickpoint, or, in other words, a local steepening in channel slope expressed as a sharp

convexity in a river profile, prompts faster rates of local channel erosion, triggering their upstream migration through the river network with a velocity that is directly related to upstream drainage area and bedrock erodibility (Whipple and Tucker, 1999; Kirby and Whipple, 2012). Knickpoints propagate through the river network, defining a morphological boundary between 1) downstream "active" areas that are adjusted or adjusting to new boundary conditions, characterised by steep topographic relief, and 2) upstream, headwater "relict" areas whose gentle morphology is likely adjusted to past boundary conditions (Kirby and Whipple, 2012).

The transient river network response is generally expected to involve the clustering of knickpoints at relatively constant elevations and χ values in lithologically homogeneous landscapes (e.g., Schwanghart and Scherler, 2020). Nevertheless, when resistant and more erodible bedrocks are exposed, the celerity of the upstream migration of knickpoints is slower where resistant rocks are exposed. Hence, in lithologically heterogeneous landscapes affected by a spatially uniform base level fall, knickpoints are typically expected to be concentrated in resistant lithologies (e.g., Bishop and Goldrick, 2010). Differently, knickpoints may be anchored in active structural boundaries or lithological contacts. Therefore, one can use spatial patterns of knickpoint distribution to infer the geomorphic history of an erosive landscape (Kirby and Whipple, 2012).

We performed an uncertainty assessment of the stream profile data, following Schwanghart and Scherler (2017), to extract knickpoints from the COP-30 DEM. Channel elevation must necessarily decrease monotonically along a profile, yet raw river profiles are consistently "bumpy", which express errors in channel elevation. We estimated how "bumpy" the river network is for each of the complete catchments upstream of the 830 m base level by calculating the maximum difference in elevation between 10th and 90th percentiles of the channel elevation generated using the "quantile carving" algorithm in TopoToolbox (Schwanghart and Scherler, 2017). These uncertainty estimates, varying from 3-21 m, with a mean uncertainty of 9 m and a standard deviation of 4 m, defined the minimum elevation threshold for identifying knickpoints in the study area.

We computed knickpoints for all channels upstream of the 830 m base level using the "knickpointfinder" algorithm in TopoToolbox, which fits an ideal concave upward river profile (associated with a uniform k_{sn} along the entire profile) to the hydrologically corrected profile. We corrected river profiles using the "quantile carving" algorithm with tau = 0.5 in TopoToolbox (Schwanghart and Scherler, 2017). Discrepancies in elevation between the ideal concave-up profile and the corrected profile represent knickpoints. The "knickpointfinder" algorithm identifies where discrepancies are highest, splitting the profile into strictly concave-

up sections separated by knickpoints and progressively diminishing the concavity constraint until a threshold tolerance value is reached. Our uncertainty assessment informed spatially varying tolerances in the study area.

2.3.3. Mapping of *in situ* ferruginous duricrusts

We mapped the distribution of *in situ* ferruginous duricrusts in QA catchment and nearby areas combining fieldwork survey and visualization methods in hillshade raster models produced from the COP-30 DEM. A typical smooth texture and the flat surface at high elevations (low-relief uplands) are diagnostic imagery patterns of these materials in the study area, which is further corroborated by a close association with Upper Cretaceous sedimentary sequences, locally affected by ferruginous duricrusts in the region. The areas investigated in the field are exhibited in Fig. 3. Even though ferruginous duricrusts are not commonly classified as a rock (e.g., Tardy, 1993), they behave as a chemically and physically resistant material which we hereafter refer to as rock unit (L16 in Fig. 3).

2.4. Results

2.4.1. Spatial patterns in topographic metrics

Local relief is spatially variable in the study area, ranging from 32 to 462 m, with a mean of 178 m. In the QA catchment, we observe a patch of high relief located downstream of the interfluve yet following roughly its shape, extending nearly continuously through the entire catchment (Fig. 5). Headwater rivers cross this high relief patch perpendicularly and similarly so do the drainage divide segments separating adjacent tributaries (black lines in Fig. 5), indicating that high relief is not confined to a single tributary but instead collectively affects the catchment's uplands. The exception is a small area in the north-western limit of the QA catchment (located between the sub-catchments P18 and P19 in Fig. 2) where high relief is not present. In contrast, we find a continuous area of low-relief downstream of the catchment-wide patch of high relief, in elevations lower than the mean (986 m) associated with the valley bottom of the trunk river and its tributaries. Discontinuous areas of low-relief are also present upstream of the high relief patch, near the QA's interfluves. These low-relief areas located near the QA's interfluves are more expressive in some areas and less in others. For example, low-relief uplands are not present (or are less evident) along the southern limit of the QA catchment, and

this is more pronounced in the Pratinha sector. Surrounding areas show similar patterns in local relief. For instance, in the Paranaíba catchment, the trunk stream valley bottom is characterised by low-relief, with a continuous patch of high relief affecting all upstream tributaries, and discontinuous areas of low-relief are present upstream of this high relief zone. In the Araguari catchment, a patch of high relief follows the trunk river in a buffer-like pattern, with low-relief areas positioned immediately upstream of these areas.

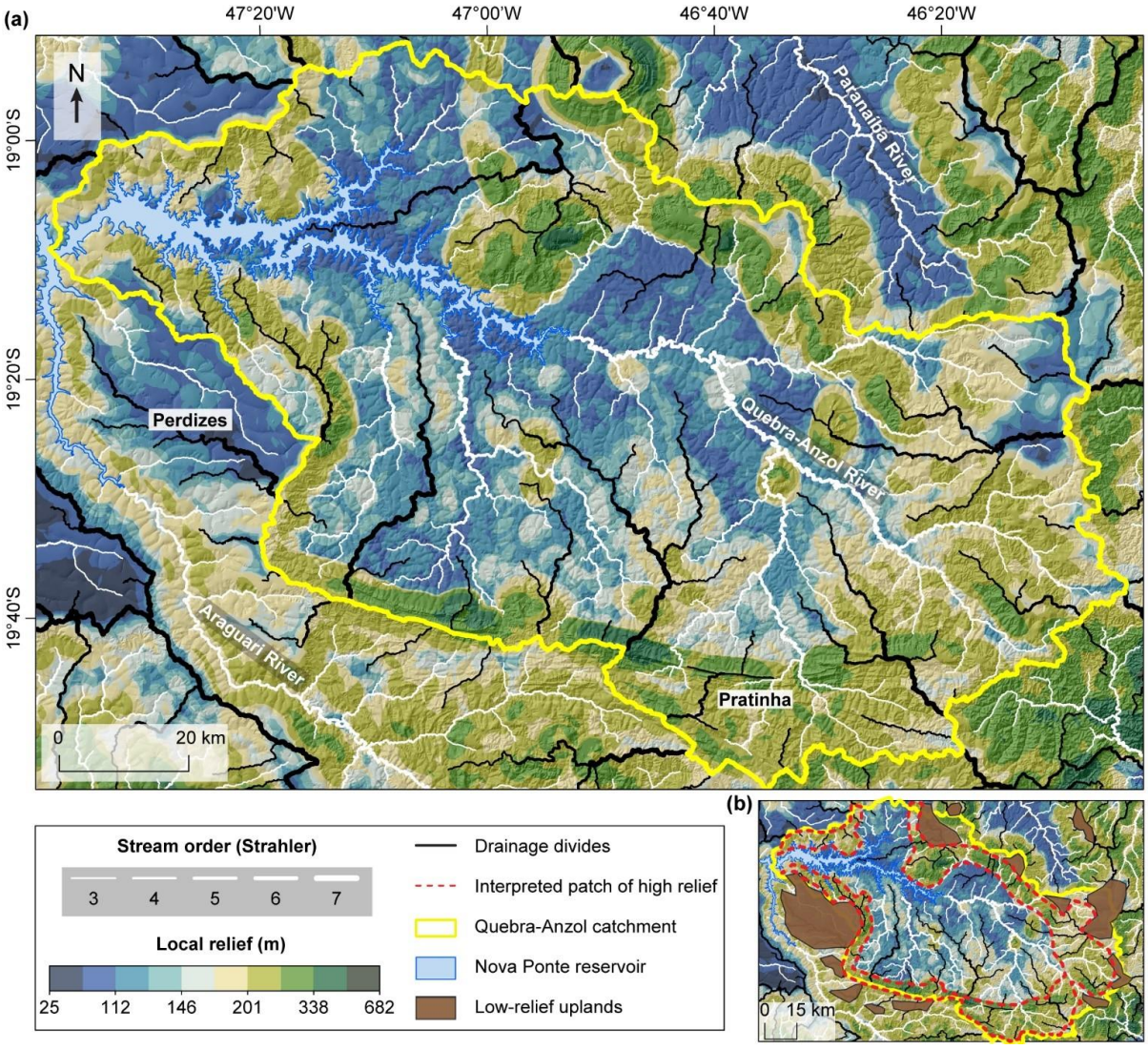

Figure 5. Local relief in the study area. (a) Map of local relief (extracted using a 5-km diameter window). (b) Map of local relief highlighting the spatial distribution of the interpreted catchment-wide patch of high relief, located downstream of the Quebra-Anzol catchment interfluves, and upstream areas of low-relief.

Hillslope angles in the QA region vary from 0 to 61º, with a mean of 7º, showing a right-skewed distribution with a bulk of low values and a long upper tail resulting from very high, low-frequency values. The spatial pattern of hillslope angles is similar to that of local relief, with a laterally continuous patch of high hillslope angles extending throughout the entire

QA catchment, separating downstream from upstream areas, both with low hillslope angles (Fig. 6). The map distribution of this patch of high hillslope angles is substantially thinner than the patch of high relief we observe (Fig. 5), suggesting that it represents an escarpment with an elevation difference of roughly 100 m immediately upstream and downstream of the feature, though with some variance throughout the catchment. In detail, the escarpment-like feature follows the river network closely, distributed adjacent to it (Fig. 7). All upstream low relief areas are strikingly flat, whereas the downstream low-relief areas appear to be less flat, with smaller and less prominent high hillslope angles adjacent to downstream channels (Fig. 7). We find upstream areas of low hillslope angles even in the southern limit of the QA catchment where we do not observe low relief areas (Fig. 5). The exception is the Pratinha sector, which shows a more complex spatial pattern of hillslope angles. The catchment-wide escarpment is not present in the north-western limit of the QA catchment, yet we observe, adjacent to its channels, small patches of high hillslope angles. Similar patterns in hillslope angles characterise nearby areas (Fig. 6).

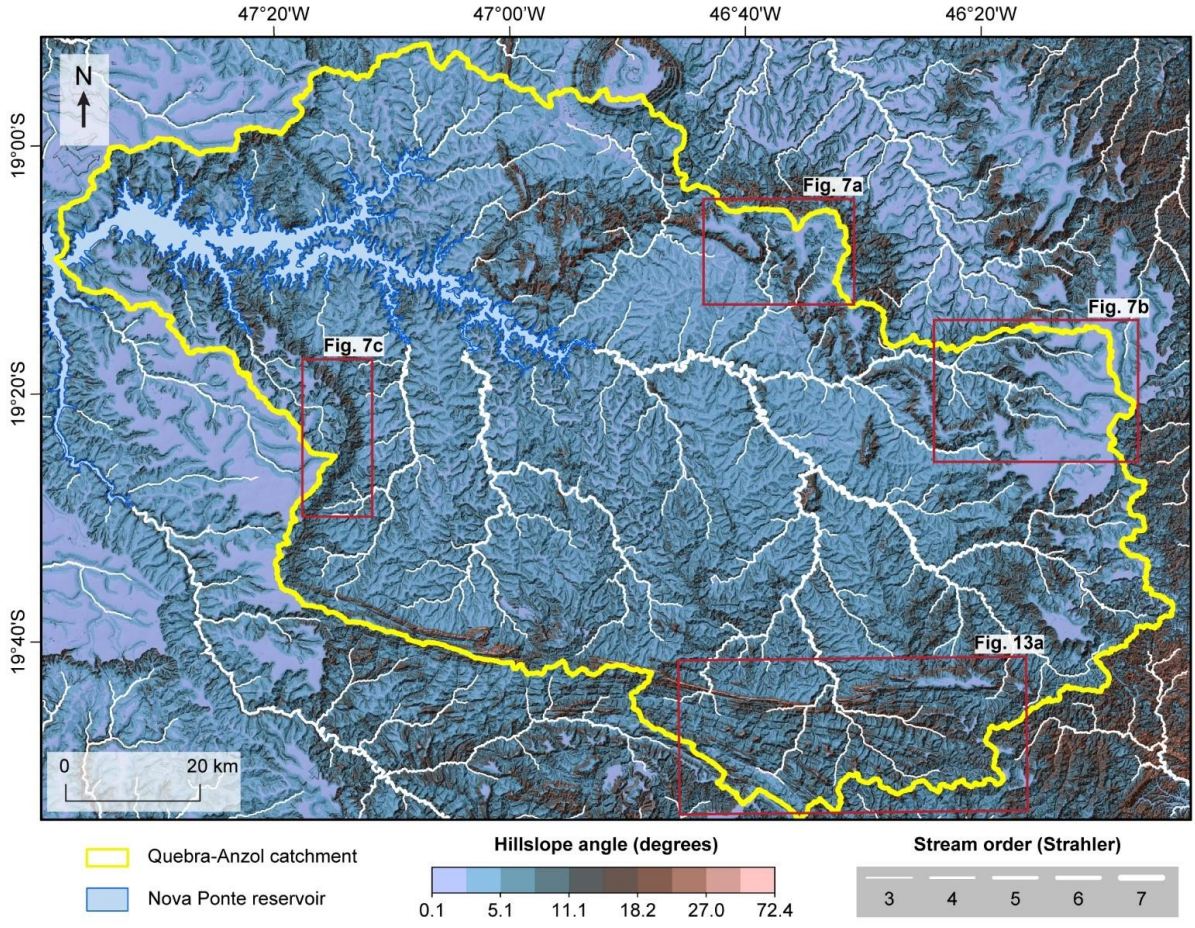

Figure 6. Map of the distribution of hillslope angles. Red rectangles indicate the location of other figures where we visualise the distribution of hillslope angles with more detail (see Fig. 7).

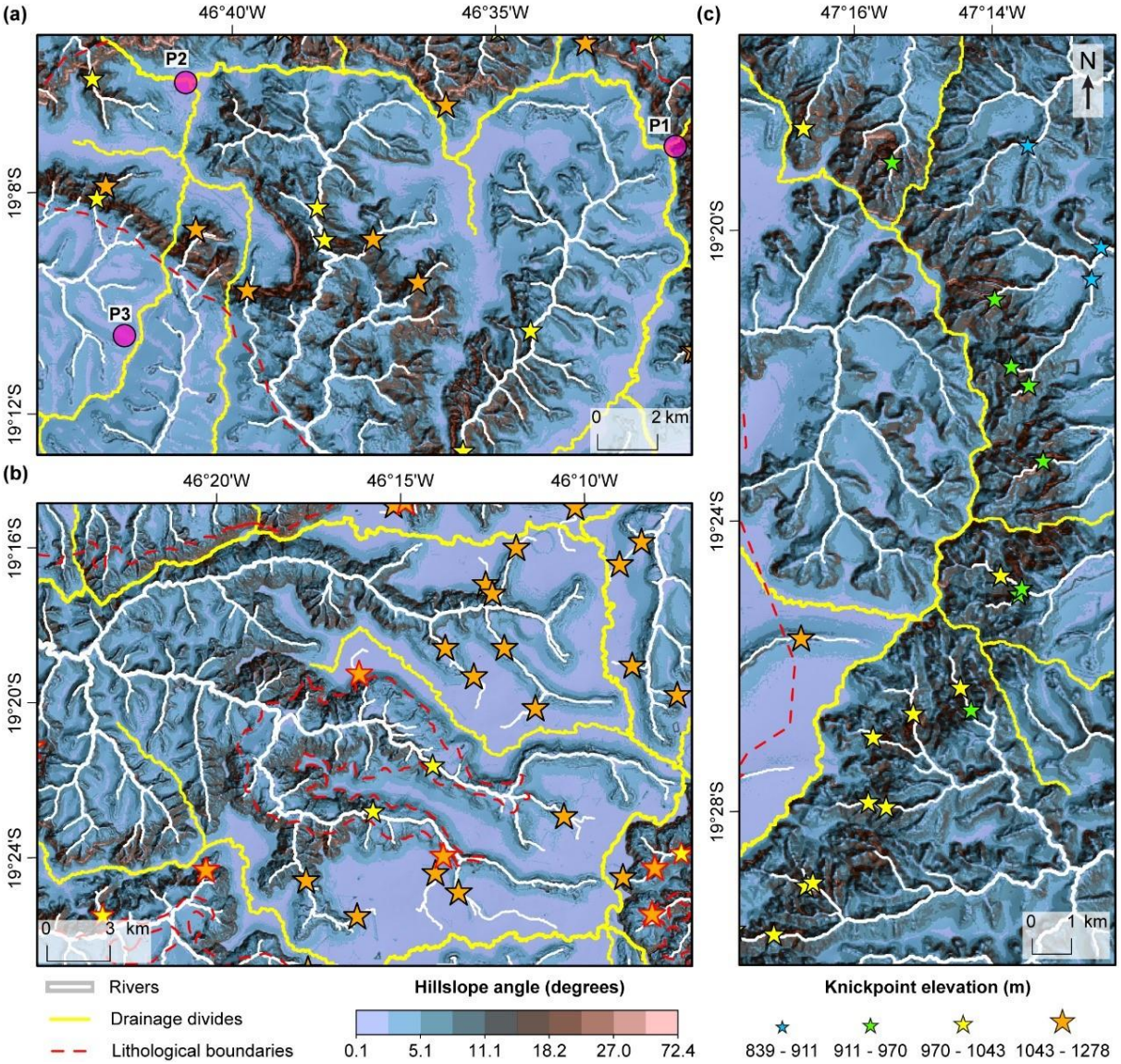

Figure 7. Detailed distribution of hillslope angles showing flat uplands and a steep downstream escarpment following adjacent the river network. Dashed red lines represent lithological boundaries separating resistant and more erodible rock units. Stars with black outlines represent knickpoints, and when these are located less than 300 m away from lithological boundaries, they exhibit red outlines instead. We explore the distribution of knickpoints in section 4.3. Panel (a) indicates the location of the images shown in Fig. 12.

The distribution of k_{sn} values is highly right-skewed (skewness = 5.3), varying from 0 to 630 $m^{0.9}$, with a mean of 18 $m^{0.9}$. The vast majority of channel segments in the study area are primarily flat, with k_{sn} values < 20 $m^{0.9}$ (Fig. 8). Where headwater rivers in the QA catchment cross the catchment-wide patch of high relief perpendicularly, k_{sn} is substantially higher, in many cases > 100 $m^{0.9}$, and these high k_{sn} segments are somewhat laterally aligned across the QA catchment (Fig. 8). Most upland rivers in the QA catchment have headwater segments with lower k_{sn} transitioning downstream to segments with higher k_{sn}, implying a systematic pattern of along-profile increase in channel steepness. The river network in nearby areas shows similar

patterns in k_{sn}, with river segments with high k_{sn} separating upstream and downstream segments with lower k_{sn} values. For instance, all tributaries of the Araguari River show very high k_{sn} values near the confluence with the trunk stream, and these rivers exhibit upstream segments with substantially lower k_{sn} (Fig. 8). The Pratinha sector shows a denser distribution of river segments with high k_{sn} values, and a single river profile exhibits sequential segments with high k_{sn}, differently from other areas in the QA catchment.

2.4.2. Links between topographic metrics and lithology

Resistant and more erodible lithologies are juxtaposed at the surface in the study area (Fig. 3). Elevation varies with bedrock erodibility to some degree, with resistant rocks such as the micaceous quartzites (L4), the Upper Cretaceous units (L12-L15), and the ferruginous duricrusts (L16) comprising, in general, areas with high elevation in the region, and more erodible rock units, such as schists and phyllites (e.g., L6, L7, and L9), granites (L8), and siltstones (L10), comprising lower elevation areas (Fig. 9a). However, we find that areas in some resistant lithologies, for example, banded iron formation (L5) and sericitic phyllites and quartzites (L3), are positioned in lower elevations than other resistant units, and areas in more erodible rock units, such as carbonaceous phyllites (L1) and sericitic phyllites and schists (L2), are located in higher elevations than other less resistant lithologies (Fig. 9a).

Local relief is similarly high for all Tonian rock units (L1-L6), with resistant rock units (L3-L5) showing a similar distribution of local relief to that of more erodible rock units (L1, L2, and L6) (Fig. 9b). Resistant and moderately resistant lithologies, including basalts (L11), pelites and cemented clastic sediments (L12), sandstones, conglomerates and lavas (L13) and the alkaline complexes (L15), show a distribution of local relief that is substantially higher than that of more erodible rock units (L7-L10) and is comparable to the distribution we find in Tonian rock units (L1-L6). The exception is the distribution of local relief in ferruginous duricrusts (L16), which is lower than we observe in other resistant units and is comparable to local relief in erodible rock units (Fig. 9b).

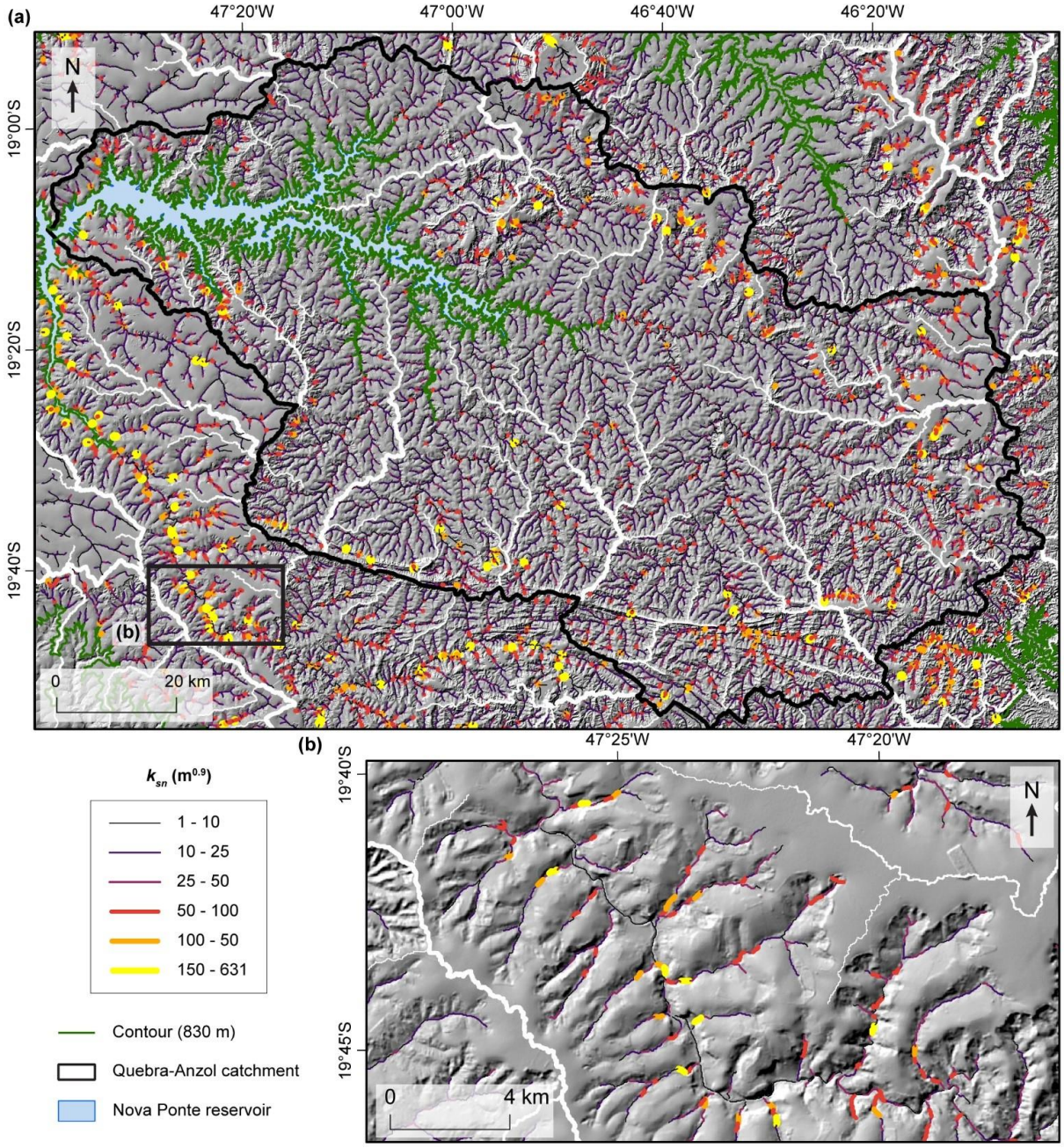

Figure 8. Map of normalised channel steepness (k_{sn}) draped over a hillshade image. (a) the QA catchment and nearby areas and (b) detailed sector in the Araguari catchment. See Methods for details about the k_{sn} calculation.

The distribution of hillslope angles is higher in some resistant rock units (L4, L5, L12, L13, and L15) than in more erodible units (L7-L10), particularly the high-end of the distribution, although the variability among different lithologies is less pronounced than with other topographic metrics (Fig. 9c). However, some erodible phyllite-dominated lithologies (L1, L2, and L6) show high hillslope angles that are comparable to some of the resistant rocks (e.g., L12, L13, and L15), and the distribution of hillslope angles are lowest under the ferruginous duricrusts (L16) (Fig. 9c). The distribution of k_{sn} per lithology shows a similar

pattern, with higher k_{sn} in resistant rock units (L4, L11, L12, L13, and L15) compared to the k_{sn} distribution in more erodible units (L7-L10), most notably the high-end of the distribution (Fig. 9d). Nevertheless, some resistant lithologies, such as the banded iron formations (L5) and ferruginous duricrusts (L16), show a k_{sn} distribution that is similar to the k_{sn} distribution we find in areas of more erodible units, for example, Tonian phyllite-dominated lithologies (L1, L2, and L6) (Fig. 9d). We observe a stark contrast in local relief, hillslope angle and k_{sn} between areas in micaceous quartzites (L4) and ferruginous duricrusts (L16), both resistant lithologies that are distributed in similarly high elevations in the region (Fig. 9).

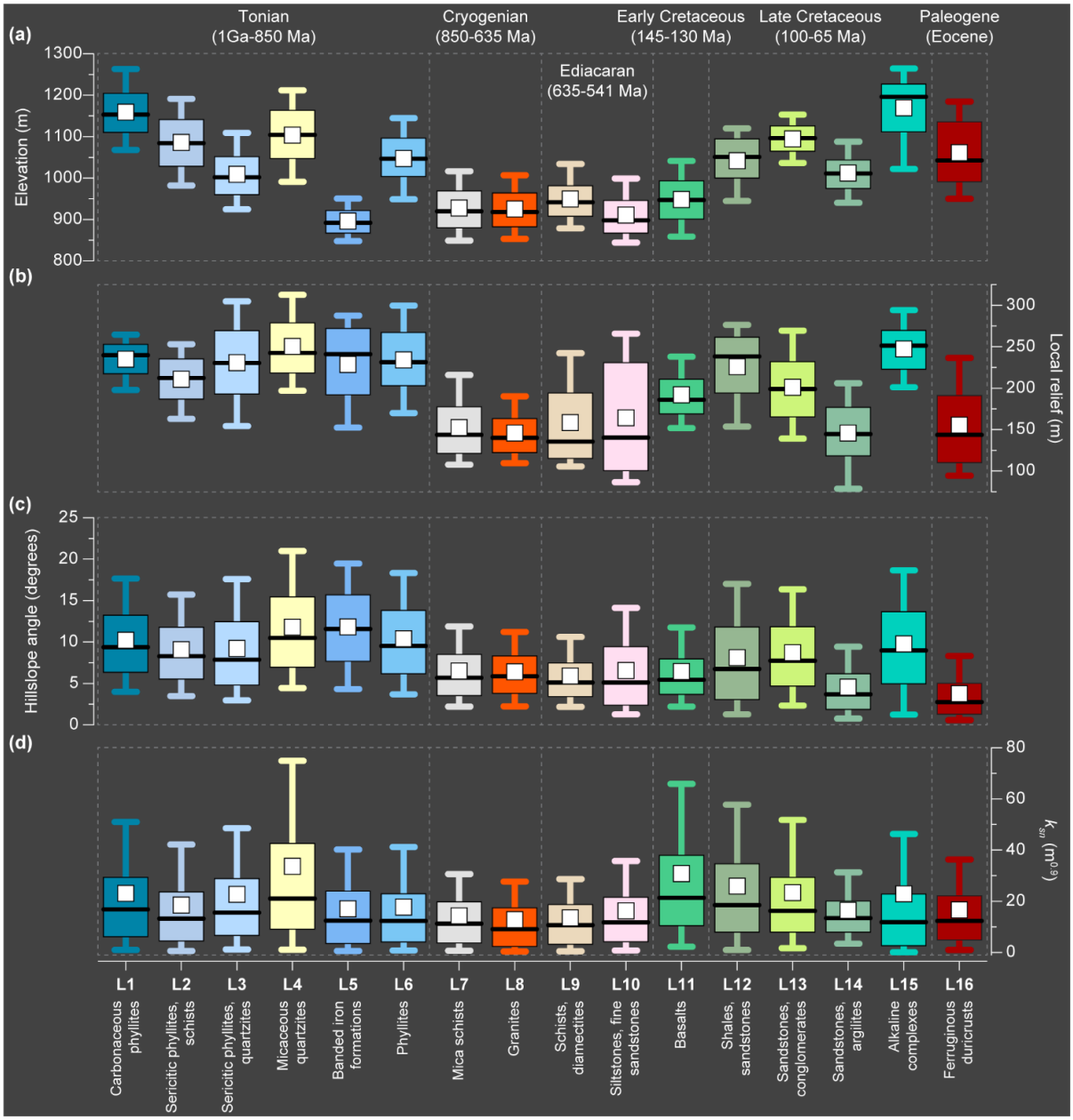

Figure 9. Boxplots of (a) elevation, (b) local relief, (c) hillslope angle, and (d) k_{sn} per lithological units. Box ranges show the interquartile range, whiskers exhibit the interval between the 10th and 90th percentiles of the data, white squares represent mean values, and the thick black line show median values. Lithological units are classified based on age and composition.

2.4.3. Knickpoints and river profiles analysis

We identify 1,636 knickpoints in the river network (Fig. 10). Knickpoints are present in most headwater rivers in the QA catchment, located primarily in tributaries' uppermost reaches, following a pattern in which they appear laterally aligned throughout the catchment (Fig. 10). We observe other knickpoints in downstream parts of the river network at lower elevations, although there are not easily recognisable patterns in their distribution. In the Araguari River catchment, all tributaries show knickpoints near their confluences to the trunk stream, whilst the upper reaches of large tributaries on the right margin of the Araguari River show upland knickpoints that appear to be laterally aligned. In nearby areas, knickpoints are present at the uppermost reaches of most headwater rivers, and, in many cases, they occur laterally aligned. Nearly 20% of the knickpoints we identify (n = 319) lie less than 300 m away from lithological contacts (Fig. 10). Knickpoints located close to lithological boundaries in the QA catchment are primarily concentrated in the Serra Negra massif (Fig. 2 and 10), where alkaline intrusions transition downstream to micaceous quartzites and phyllites (L4 and L6), secondarily in the southern limit of the QA catchment where micaceous quartzites transition downstream to the schist-dominated Rio Verde and Paracatú formations (L9 and L12), and in a few locations outside the QA catchment (Fig. 10).

Filtering away knickpoints that may be anchored to lithological boundaries, we find that knickpoints are spread over a relatively large range of channel elevations, varying from 839 to 1,256 m (Fig. 10b). Nonetheless, the distribution of knickpoint elevations indicates three prominent peaks, the first (and most evident) at roughly 910 m, including most knickpoints in the vicinity of the confluence between tributaries and the Araguari River and various downstream channel segments in the QA catchment and nearby areas. The second peak is at roughly 1,025 m, including headwater segments located relatively close to the Nova Ponte reservoir downstream of QA's southern and northern limits, the downstream part of the Pratinha sector, and segments located upstream of the lower elevation knickpoints outside the QA catchment. Finally, the third peak is at 1,150 m, including upland knickpoints in the QA catchment, the Araguari River catchment, and nearby areas. Knickpoints lying in lower elevations are distributed over a range of erodible lithologies, such as phyllites (L1, L6), schists (L2, L7, L9), granites (L8), and siltstones (L10), while the only resistant lithology associated with lower elevation knickpoints are basalts (L11) exposed close to the Araguari River. In contrast, knickpoints in high elevations are underlain by resistant lithologies, such as quartzites

(L3, L4), sandstones (L13, L14), and, in particular, ferruginous duricrusts (L16) that concentrates by far most of the knickpoints (Fig. 10c).

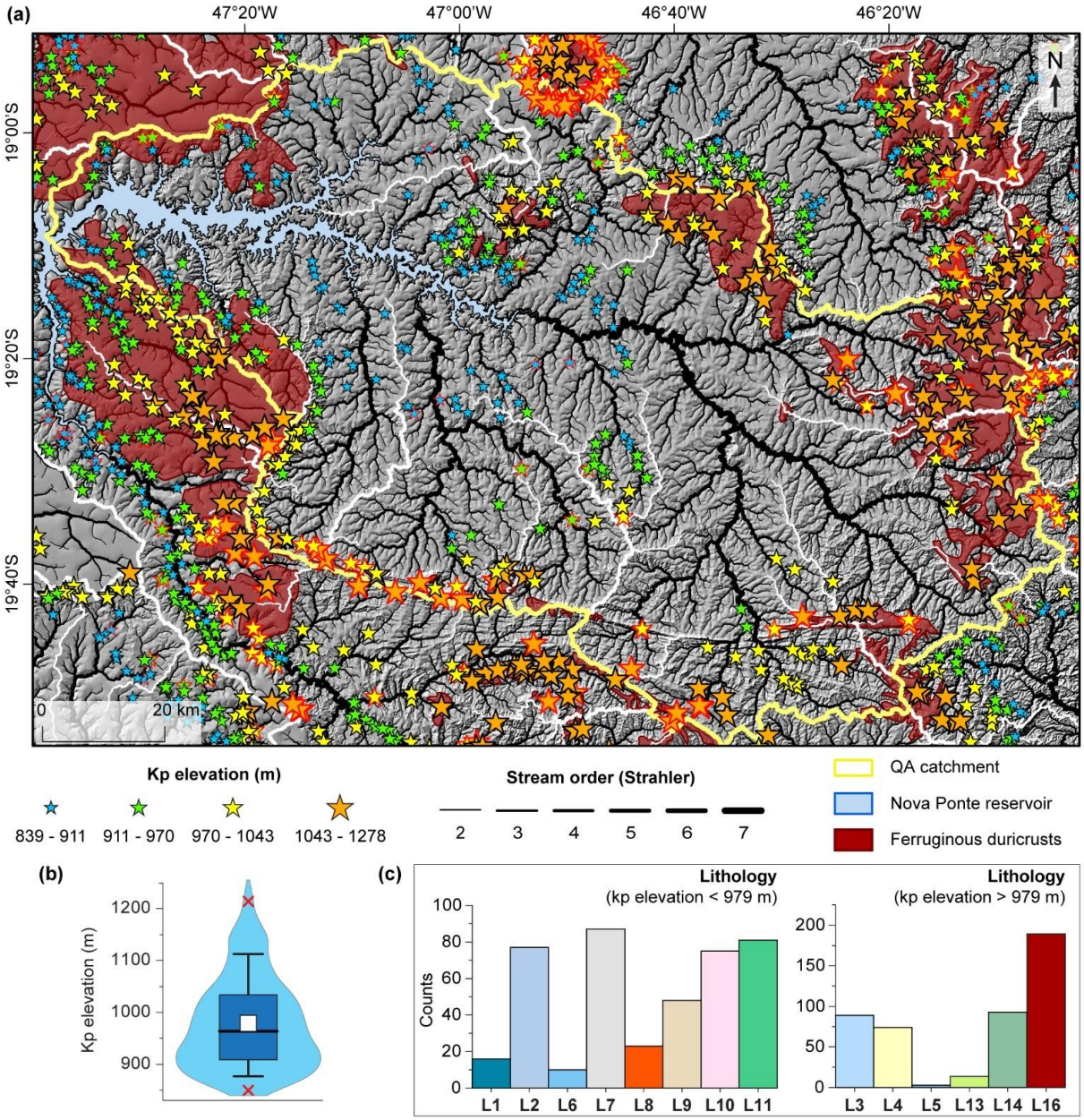

Figure 10. Spatial distribution of knickpoints in the study area. (a) Map distribution of knickpoints, whereby knickpoint elevations are classified by quartiles. Stars with red outlines represent knickpoints located less than 300 m away from lithological boundaries. (b) Violin plot showing the probability density (smoothed by a kernel density estimator) of knickpoint elevations. Boxplot elements are the same as in Fig. 9. (c) Histograms showing the frequency of knickpoints per lithology above and below the mean knickpoint elevation.

River profiles of headwater rivers and tributaries (including all rivers with more than 1 km of extension) throughout the QA catchment in χ-elevation space show that most tributaries of upland rivers exhibit prominent convexities in their profiles, with only a few located close to lithological boundaries (Fig. 11). In contrast, several trunk streams show linear profiles in χ-

elevation space (e.g., P4 and P20 in Fig. 11). We observe that river profiles show different overall morphologies in the study area, but river profiles of adjacent areas in related geomorphic contexts are similar, such as, for example, a1-a5, c1-c2, d1-d2, e1-e2, and g1-g2 in Fig. 11. Clusters of knickpoints per elevation are not evident in Fig. 11, although they might be present. For example, adjacent rivers P7 and P8 (Fig. 11c) show knickpoints in their tributaries in similar elevations. Other rivers, such as P1 and P2 (Fig. 11a), might show different clusters of knickpoint elevation, yet these are not easily discernible from the plot.

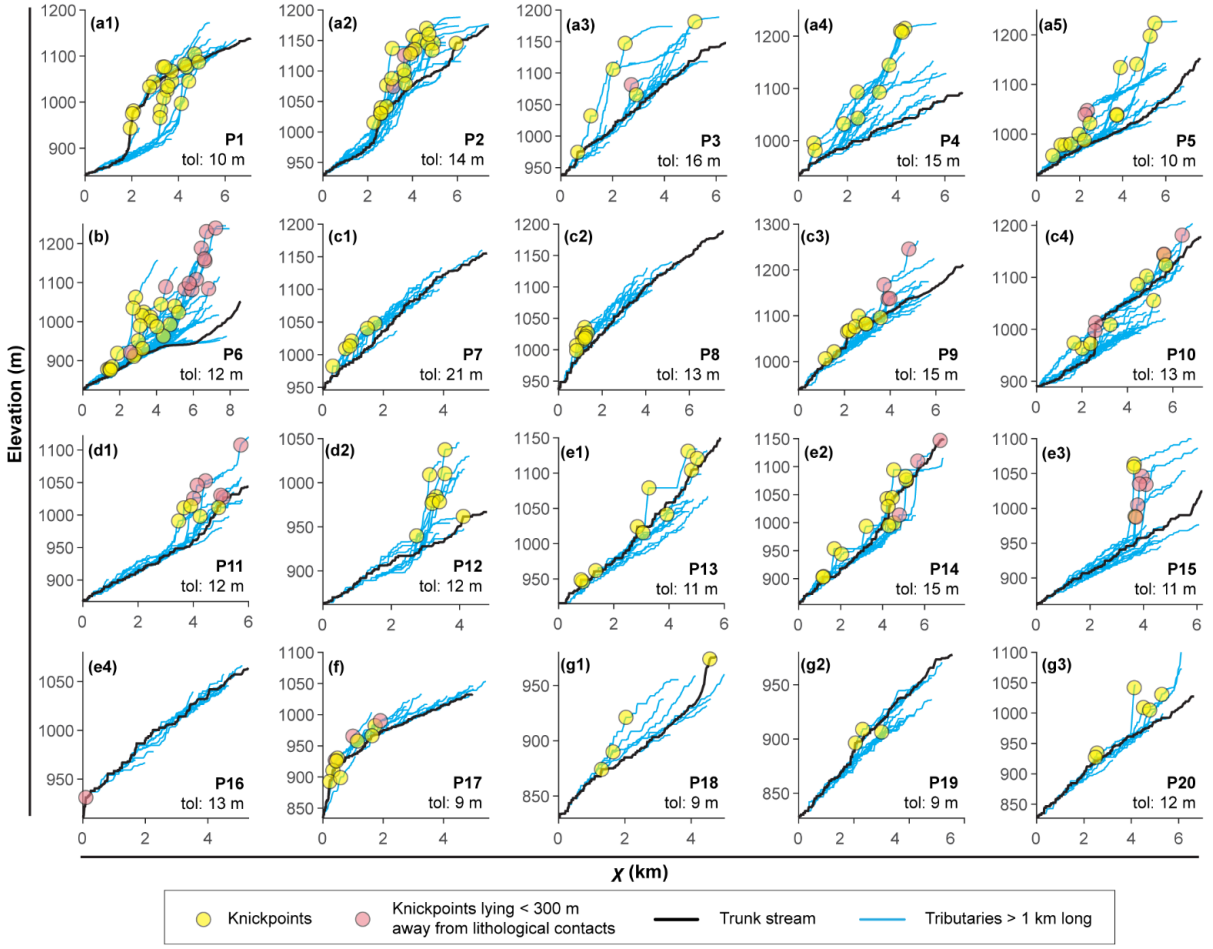

Figure 11. River profiles in χ-elevation space of upland drainages in the study area. Panels are separated according to geomorphic context; for example, (c1-c4) refers to rivers in the Pratinha sector, while (f) show river profiles in the Perdizes sector. "Tol" indicates the threshold tolerance value used to extract knickpoints (see Methods for details). See Fig. 2 for the location of upland sub-catchments.

2.4.4. Ferruginous duricrusts and shallower weathered soils in the QA catchment

In situ ferruginous duricrusts occur at a mean elevation of 1,060 m, and they mantle low-relief uplands located near the QA's interfluves (Figs. 3 and 9). The ferruginous duricrusts are formed over various bedrock (e.g., phyllites, basalts, pyroclastic, and epiclastic rocks), with thickness varying from 1 to 4 m, or even more, transitioning upwards into non-indurated horizons (locally very thick ~40 m) (Fig. 12). We observe that the ferruginous duricrust profiles exposed on the surface present several morphological pieces of evidence of dismantling, such as physical degradation and mineralogical transformation (e.g., Tardy, 1993). Discontinuous thin layers are spatially distributed immediately downstream of the low-relief uplands in the QA catchment. Such deposits are comprised of debris of ferruginous duricrusts and bedrock, suggesting that these gravity/erosion-driven sediments were supplied from source areas originally containing *in situ* ferruginous duricrusts. Weathering profiles in downstream areas, in contrast, are generally mantled by clay-rich shallow soils (<3 m in depth) developed at the expense of the underlying bedrock (e.g., schists, phyllites, mica schists and granites) and with no ferruginous duricrust (Fig. 12). Hence, a stark contrast in regolith thickness characterises low-relief uplands and downstream areas.

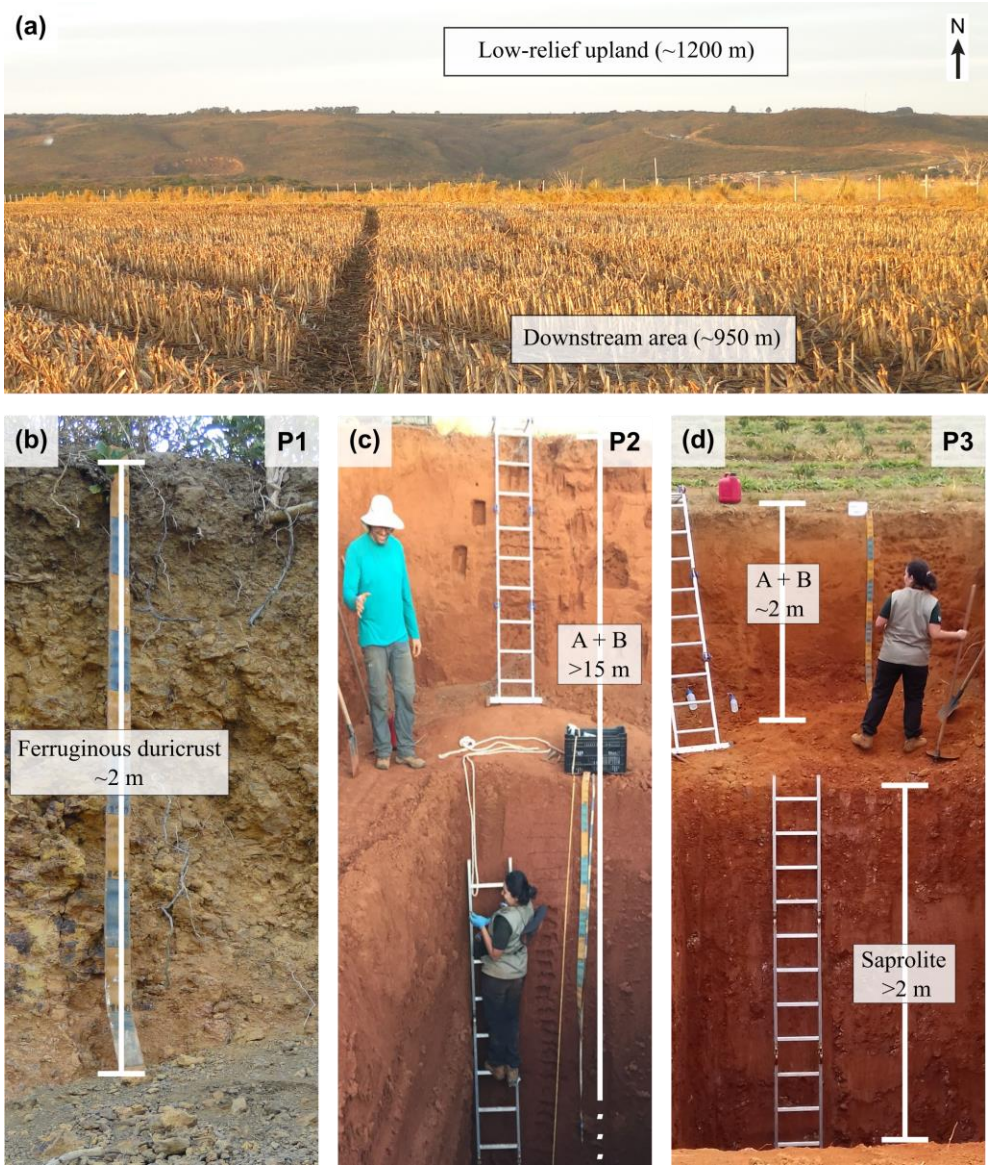

Figure 12. Example of the low-relief uplands and downstream areas near P1 (see Figs. 2 and 7a) and the corresponding regolith developed on both landscape positions. (a) Photo took from a downstream area (in P3) looking into a low-relief upland (where P2 is located). (b) Extremely dismantled ferruginous duricrust underlying a thick weathered profile developed in the low-relief uplands (in panel c) and a shallow weathered profile developed at the expense of the underlying bedrock in the valley bottom (in panel d).

2.5. Discussion

2.5.1. Transience in a lithologically diverse post-orogenic setting

Topography in the QA catchment and surrounding areas show spatial patterns that are characteristic of landscapes experiencing a transient topographic disequilibrium in response to a relative base level fall, commonly reported in tectonically active areas (e.g., Wobus et al., 2006; Reinhardt et al., 2007) and, in some cases, in post-orogenic landscapes (e.g., Bishop and Goldrick, 2010; Gallen et al., 2013; Miller et al., 2013; Prince and Spotila, 2013; Gallen, 2018).

The numerous knickpoints we find in headwater channel segments in the QA catchment and nearby areas demarcate a stark topographic transition between essentially flat uplands above the knickpoints, with low k_{sn} and hillslope angles, a zone of high k_{sn}, hillslope angles and local relief immediately downstream of the knickpoints, and a downstream area of gentle morphology at lower elevations (Figs. 5, 6 and 8). In the QA catchment, the laterally continuous patch of high-relief expresses a basin-wide escarpment with an elevation drop of ~100 m which, in detail, follows adjacent to the map distribution of the river network, implying that channel steepening and the resulting accelerated river incision induced the steepening of adjacent hillslopes (Figs. 7 and 11). Our findings suggest that the entire region is in a transient state of adjustment instead of topographic equilibrium or quasi-steady state, whereby the propagation through the river network of a transient wave of river incision rejuvenated the topography. The upper limit of this area of high-relief, located upstream of lithological boundaries between resistant and more erodible units (Figs. 3 and 7), define the leading edge of propagation of the rejuvenation signal that separates areas that are adjusting or adjusted to the new base level and relict low-relief uplands that are evolving under pre-rejuvenation boundary conditions (e.g., Gallen et al., 2013).

Corroborating such an interpretation, the lithological variability characterising the study area, where metamorphic, crystalline, volcanic, and sedimentary units are exposed side by side at the surface, is not the primary controlling factor in the distribution of k_{sn}, hillslope angles and local relief (Fig. 9), which is otherwise expected in a landscape in topographic equilibrium or quasi-steady state (Hack, 1960). For example, two of the most resistant lithologies exposed, the micaceous quartzites (lithological unit L4) and the ferruginous duricrusts (L16), show distinctly different topographic expression, with substantially higher k_{sn}, hillslope angles and local relief in micaceous quartzites, while ferruginous duricrusts show the lowest hillslope angles among all rock units. Similarly, erodible phyllite-dominated lithologies (L1, L2, and L6) show distributions of k_{sn}, hillslope angles and local relief similar to that of some resistant units. However, our data show some degree of lithological control in how some resistant units (L4, L11, L12, L13, and L15) are generally characterised by higher k_{sn}, hillslope angles, and local relief than more erodible rocks (L7-L10) (Fig. 9). Nonetheless, we do not have Schmidt hammer measurements or river erosion data to allow quantitative discrimination of erodibility between units. Furthermore, the transient topographic signal we infer is not anchored in active structural boundaries or lithological contacts. Only a minor proportion of mapped knickpoints are located close to lithological contacts (Fig. 10), and there are no patterns in the distribution of lithological or structural boundaries that could explain the transience we infer.

Relief is therefore increasing over time in a landscape evolving over timescales of millions of years instead of slowly decaying as most conceptual and numerical models of post-orogenic landscape development assume (e.g., Ahnert, 1970; Baldwin et al., 2003; Egholm et al., 2013) or remaining steady over time as the topographic equilibrium hypothesis predict (e.g., Hack, 1960; Matmon et al., 2003). On the one hand, our results support a growing body of literature showing that landscape dynamics in dead orogens is more complex and dynamic than previously thought, with relief resurgence long after cessation of ongoing tectonics (e.g., Pazzaglia and Brandon, 1996; Hancock and Kirwan, 2007; Quigley et al., 2007; Bishop and Goldrick, 2010; Gallen et al., 2013; Miller et al., 2013; Tucker and van Der Beek, 2013; Gallen, 2018). On the other hand, the low-relief uplands we identify represent a relict landscape, presumably adjusted to pre-existing boundary conditions and maintaining its morphology, which in many cases in the region are capped by ferruginous duricrusts. The presence of relict and transient areas indicates that older and more recent topographic elements coexist in the landscape. Hence, the topographic rejuvenation we infer cannot explain the entire topographic configuration of the study area, particularly the high elevations in drainage divides and nearby areas.

Knickpoints migrate upstream at rates that are commonly predicted to follow a non-linear kinematic wave proportional to upstream area raised to the exponent *m*, estimated as 0.45 in the study area (see methods section), and a fluvial erosion efficiency coefficient which reflects bedrock strength, climate conditions and other controls (Whipple and Tucker, 1999). In cases where channel slope scales linearly with fluvial erosion and the fluvial erosion efficiency coefficient is spatially uniform (e.g., areas in a single lithology), the wave speed depends only on drainage area, implying a transient response that produces a contour-like pattern of knickpoints in map view, with an overall consistency in knickpoint elevation (e.g., Wobus et al., 2006). However, if the fluvial erosion efficiency coefficient varies spatially, knickpoint retreat rates also change, with faster retreat rates where rocks are less resistant (e.g., Gallen, 2018) or where precipitation is high (e.g., Ferrier et al., 2013). The QA region shows a complex spatial distribution of lithologies, with substantial along-profile variations in the efficiency coefficient in every river profile, implying that a contour-like map distribution of knickpoints lying in common elevations is unlikely. We observe, however, some degree of consistency in knickpoint elevation, with three peaks at 910, 1,025, and 1,150 m, albeit with some variance. Knickpoints in lower elevations are distributed in various lithological units yet concentrated in non-resistant units, while knickpoints in upland channel segments are related to resistant units, with ferruginous duricrusts concentrating by far most knickpoints (Fig. 10).

These characteristics are consistent with the predicted transient response of at least two and perhaps more migrating waves. The oldest drop in base level is documented in resistant rocks at high elevations because these rocks act slowing the propagation stalling the transient signal similarly as in Bishop and Goldrick (2010), and the youngest drop in base level is distinctly expressed in the Araguari river network where knickpoints mark all tributaries near their confluences to the trunk stream (Fig. 10). We emphasise that we do not have quantitative constraints on erosion efficiency to model the transient response adequately, yet we expect the transient signals to be naturally complex given the lithological diversity in the study area.

2.5.2. Preservation of a pre-existing low-relief landscape capped by ferruginous duricrusts

Ferruginous duricrusts underlie most of the relict uplands we infer, and these materials archive information about the pre-existing boundary conditions before the oldest transient wave of topographic rejuvenation. The formation of duricrusts is dependent on favourable climate conditions, generally meaning tropical seasonally wet and dry climates that promote weathering and supergene mineral formation in a close association with the water table, and geomorphic and tectonic conditions that act inhibiting the effectiveness of runoff and erosion processes, commonly referring to gentle morphologies and relative tectonic stability (e.g., McFarlane, 1976; Nahon, 1986; Tardy, 1993; Widdowson, 1997). These weathering profiles record a protracted history of exposure and weathering, meaning that they keep evolving after their formation, likely until the optimal climate and tectonic conditions terminate, implying the onset of a significant fall of the water table and presumably the acceleration of erosion processes (Vasconcelos and Carmo, 2018; Vasconcelos et al., 2019). Geochronological data on the formation of ferruginous duricrusts is not available in the APU region, yet in surrounding regions, (U-Th)/He and $^{40}Ar/^{39}Ar$ dating of iron or K-Mn oxides in duricrusts located in high elevations areas of SE Brazil suggest that duricrusts formed 70-48 Ma (e.g., Monteiro et al., 2014; Monteiro et al., 2018; Vasconcelos and Carmo, 2018; Vasconcelos et al., 2019). Weathering profiles developed on low-relief uplands in other tropical, post-orogenic landscapes suggest roughly coeval ages, including Peninsular India (e.g., ~53–50 Ma, Bonnet et al., 2016; ~53 Ma, Beauvais et al., 2016; ~53–44 Ma, Jean et al., 2020) and West Africa (e.g., ~59-45 Ma, Beauvais et al., 2008). Such consistency in the ages of the materials capping low-relief uplands in various tropical, post-orogenic settings indicates a period of optimal climate and

tectonic conditions in the Paleogene, probably global in extent, which is consistent with global paleoclimatic studies (e.g., Zachos et al., 2001).

The morphology of hillslopes in ferruginous duricrusts is strikingly flat, and steep adjacent hillslopes to upland channels demarcate these flat uplands (Figs. 6 and 7), implying that river incision and feedbacks with adjacent hillslopes, which we interpret to be the result of transient disequilibrium, are progressively dismantling duricrusts that were formerly more spatially extensive. The topographic characteristics of these uplands capped by duricrusts are consistent with the scenario of incision into a pre-existing low-relief landscape proposed by Whipple et al. (2017), in which remnants patches are always located high in the landscape, near drainage divides but extending beyond these (Figs. 2 and 3), show a low variability in relief and are distributed at similarly high elevations (>1,000 m). We expect that consistently low erosion rates characterise these remnants due to their general flatness and the arguably high resistance to weathering and erosion of the ferruginous duricrusts, even though we do not have data to support it. Extremely low erosion rates were reported in areas capped by similar materials in SE Brazil (e.g., Monteiro et al., 2018; Vasconcelos et al., 2019). Such low erosion rates promote the prolonged preservation of this relict landscape, which presumably will only be consumed by erosion when affected by the oldest transient wave of topographic rejuvenation that we infer.

2.5.3. Driving mechanism for topographic rejuvenation

While the topographic evidence of transience in the study area is compelling, the factor or factors responsible for the two (and perhaps more) topographic disequilibrium events are uncertain. Factors such as drainage reorganization (e.g., Prince et al., 2011), far-field-driven tectonic uplift (e.g., Hack, 1982), mantle-flow-driven uplift (e.g., Gallen et al., 2013; Miller et al., 2013), denudational isostatic rebound (e.g., Bishop and Goldrick, 2010), and climate changes (e.g., Hancock and Kirwan, 2007) have been proposed as potential drivers of relief resurgence in post-orogenic settings. Much because of our lack of quantitative information on timing and rates of fluvial erosion and the variability of erosion efficiency, we have no decisive way to resolve the mechanism responsible for the transience or estimate timings for base level fall events postdating the duricrusts' ages.

Nonetheless, the regional expression of the transient signals we infer, affecting the QA catchment and its surroundings and not limited to catchments sharing a drainage divide, is unlikely to express discrete river capture or captures (Whipple et al., 2017), and the study area lacks evidence of regional drainage reorganization such as elbows of capture (Bishop, 1995).

The available data on the Cenozoic climatic history of Brazil indicates many cyclic oscillations of drier and wetter conditions within different timescales, with various of these oscillations showing similar magnitudes (e.g., Zachos et al., 2001; Behling, 2002; Strikis et al., 2018), which is not easily linked to our data consistent with two and perhaps three disequilibrium events. Furthermore, a climate change to more humid conditions is predicted to reduce the steepness of river segments (e.g., Whipple and Tucker, 1999; Wobus et al., 2010), whereas we observe steepening of river profiles immediately below the relict uplands. The topographic resurgences we infer are less than a few hundred meters, similar to post-orogenic relief increases observed in the Appalachians (e.g., Gallen et al., 2013; Miller et al., 2013). Such magnitudes of relief growth are broadly consistent with the rejuvenation expected in the context of rock uplift driven by mild denudational isostatic rebound (e.g., Bishop and Goldrick, 2010), long-wavelength, low-amplitude uplift driven by some form of mantle dynamics (e.g., Gallen et al., 2013; Miller et al., 2013), or mild uplift driven by compressional far-field stresses (e.g., Marques et al., 2013).

2.5.4. Areas with different topographic signatures in the QA catchment

Two areas in the QA catchment show patterns in topography that are different from those discussed so far. The first is a small area in the north-western limit of the QA catchment, located between the sub-catchments P18 and P19 in Fig. 2, where the zone of high local relief, hillslope angles and k_{sn} values is not present. The resistant lithologies underlying upstream areas in the QA catchment, notably quartzites and ferruginous duricrusts, are not present in this small area, and we hypothesise that the transient signals were able to sweep through rivers and hillslopes, leaving the system. In contrast, these signals are stalled primarily in resistant lithologies in other parts of the QA catchment. The second is the Pratinha sector, which shows complex spatial patterns in topography, with high hillslope angles, local relief, and k_{sn} values upstream (Figs. 5, 6 and 8) of what we interpret as the basin-wide escarpment, and where the relict uplands are not present. Although this is not the main objective of our study, we use field structural analysis to tentatively explain the spatial patterns in topography in the Pratinha sector. We emphasise, nonetheless, that more work is necessary to fully resolve its tectonic evolution.

In the field in the Pratinha sector, we identify trapezoidal and triangular facets, landslides comprised of debris of ferruginous duricrusts and bedrock along the escarpment of two approximately E-W left-lateral strike-slip faults and deep fault-driven gullies controlled by roughly E-W and N-S trends (Fig. S1). We also identify transverse normal faults (Riedel T

fractures) oriented approximately N-S, which outline a domino-like block arrangement tilted towards W (Fig. S1b). Remains of a sedimentary layer with debris of ferruginous duricrusts and bedrock occur along the master faults and on top of the domino blocks, showing a difference of elevation ~100 m (Figs. 13, S1f and S1g). These roughly N-S normal faults limit the longitudinal extension of the ~E-W master faults and are apparently lowering the base level of the trunk stream in the Pratinha sector (Fig. 13). The geometry and kinematics of master and transverse faults are consistent with what is generally expected in a pull-apart basin (Liu and Konietzky, 2018), and thus we named it here as the Pratinha Pull-Apart Basin (PPB).

The PPB is embedded in a horsetail splay structure of the Pratinha Fault Zone (PFZ) along a Neoproterozoic thrust structure (Fig. 13a) that reactivated during the South Atlantic rifting stage, which is suggested by the unexposed E-W-trending Pratinha I and II alkaline intrusions (Marangoni and Mantovani, 2013), and was likely reactivated later as a post-rift strike-slip fault. This transtensional basin characterised by a negative flower structure geometry was probably formed due to a releasing bend in the ~E-W left-lateral strike-slip fault system (Fig. 13b). The spatial patterns in topography (Figs. 6, 10 and 11f) coupled with field evidence such as trapezoidal facets, landslides and fault-driven gullies (Figs. 13b and S1) corroborate that this sector has undergone tectonic reactivation. Therefore, it is reasonable to hypothesise that the geometry and kinematics of the master and transverse faults of the PPB are compatible with stress regimes identified by various authors in the Brazilian passive margin. Examples include a Plio-Pleistocene stress regime with a ~N-S horizontal maximum paleostress (SHmax) (e.g., Peyerl et al., 2018), or a Neogene stress regime attributed to an NW-SE distension event (e.g., West and Mello, 2020) or a strike-slip stress regime with N-S-trending compression and E-W-trending extension (e.g., Bezerra et al., 2020).

The link between the regional rock uplift events responsible for the topographic resurgence in the study area and the strike-slip reactivation of old fault zones and the Pratinha Pull-Apart Basin formation is not straightforward or resolved. Nevertheless, the activity of the two most likely candidates as drivers of regional rock uplift, denudational isostatic rebound and compressional far-field stresses, can trigger reactivation of pre-existing structures (e.g., Zoback, 1992; Cobbold et al., 2001; van Arsdale et al., 2007; Marques et al., 2013; Talwani, 2017; Gallen and Thigpen, 2018), potentially causing geomorphic and structural consequences consistent with the described for the Pratinha sector. Hence, more work is necessary to reconcile regional rock uplift events and the local effects superimposed adequately in the study area. Furthermore, the APU setting consists of a complex mosaic of elements evolving contrasting crustal thickness (e.g., Mantovani et al., 2005), deep weakness zones such as the Azimuth 125º

Lineament and the associated Pratinha Fault Zone (e.g., Marangoni and Mantovani, 2013; Moraes Rocha et al., 2019), and recurrent transtensional reactivation during its post-rift evolution (e.g., Moraes Rocha et al., 2014), suggesting an intricate post-orogenic history.

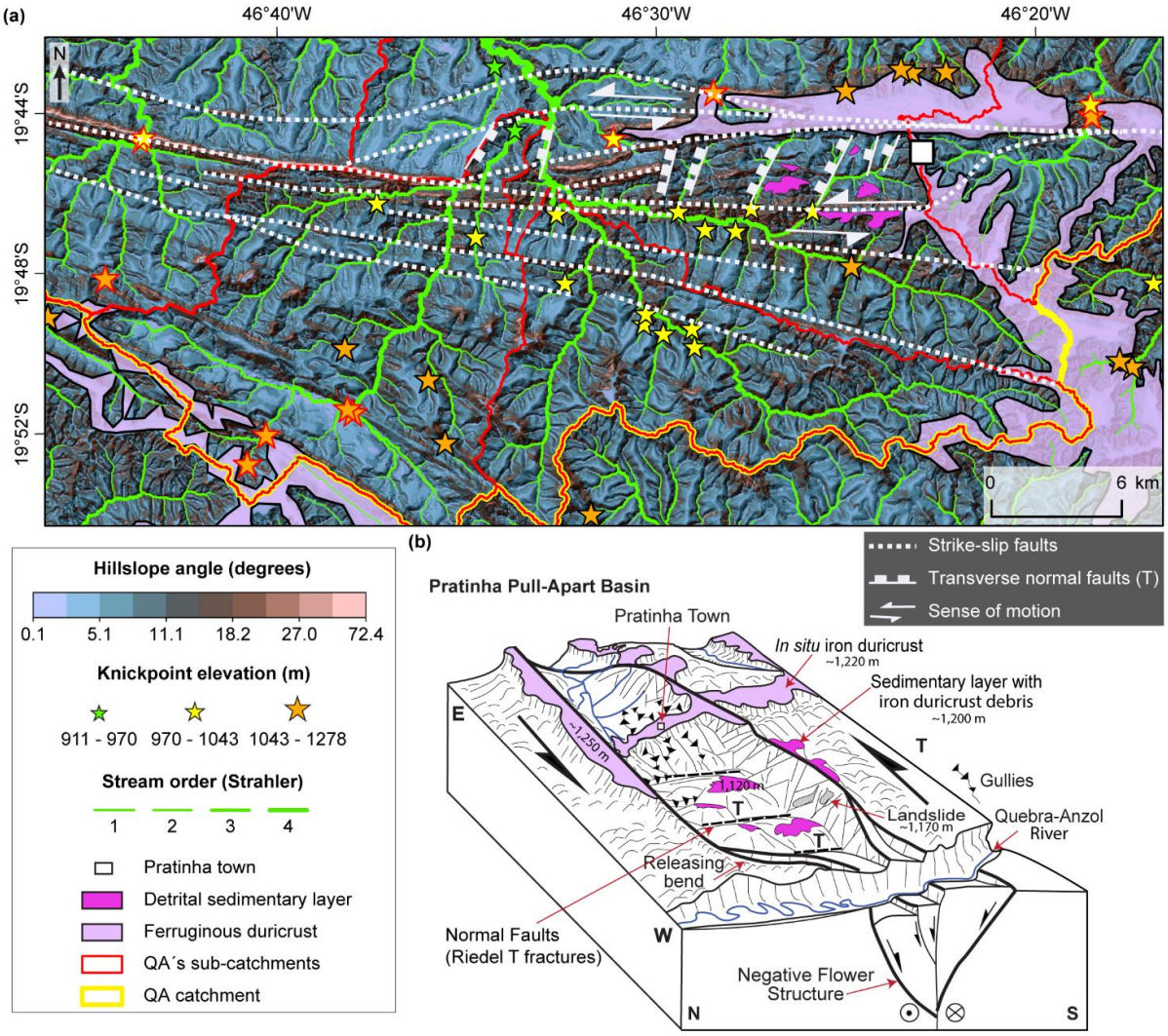

Figure 13. Structural and geomorphic elements of the Pratinha sector and the Pratinha Pull-Apart Basin (PPB). (a) Geometry and kinematics of the PPB and map distribution of hillslope angles, knickpoints, and ferruginous duricrusts. (b) Sketch of the PPB showing its negative flower structure and associated geomorphic features. We show some of the geomorphic features we observed in the field in Fig. S1 (e.g., ~E-W fault escarpments, ~N-S transverse normal faults, gullies, and landslides).

2.6. Conclusion

We present topographic data exploring spatial patterns in channel steepness, local relief, hillslope angles, and the distribution of knickpoints, and we test their relationships with variations in bedrock lithology in a tropical wet and dry, high relief post-orogenic landscape located in the Brazilian continental interior. We show that the topography in the study area is in a topographic disequilibrium condition whereby the propagation through the river network of at least two transient waves of river incision rejuvenated the topography, implying relief growth long after cessation of ongoing tectonics ~80 Ma. The front of propagation of these regional transient signals is delimited by high elevation knickpoints underlain by resistant lithologies, which presumably supress the upstream migration of these signals, isolating upper relict areas from base level drops. Relict uplands with a markedly flat morphology are primarily capped by ferruginous duricrusts, likely formed in the Eocene. Transient waves of accelerated river incision and feedbacks with adjacent hillslopes are actively dissecting these relict uplands. Our study demonstrates that a post-orogenic landscape in the tropical Brazilian continental interior is an ancient setting with younger topographic elements, whereby stark contrasts in lithology strongly control the style and pattern of transient landscape response to drops in base level. This transience is consistent with regional uplift events, likely driven by denudational isostatic rebound or compressional far-field stresses, with local effects superimposed linked with the strike-slip reactivation of old faults and the formation of the Pratinha Pull-Apart Basin. The post-orogenic history of other lithologically diverse ancient landscapes is likely similar in that they are not adequately explained by a progressive decay in relief and denudation rates but instead show a more dynamic evolution, with variations in erosion rates in space and time, and where variations in lithology play an essential role on landscape dynamics.

References

Ahnert, F., 1970. Functional relationships between denudation, relief, and uplift in large, mid-latitude drainage basins. Am. J. Sci. 268, 243-263. https://doi.org/10.2475/ajs.268.3.243, 1970.

AIRBUS, European Space Agency, Sinergise, 2020. Copernicus Global Digital Elevation Model. Distributed by OpenTopography. https://doi.org/10.5069/G9028PQB. Accessed: 2021-05-03.

Baldwin, J.A., Whipple, K.X., Tucker, G.E., 2003. Implications of the shear stress river incision model for the timescale of post-orogenic decay of topography. J. Geophys. Res. 108, 2158, https://doi.org/10.1029/2001JB055.

Batezelli, A., 2003. Análise da sedimentação cretácea no Triângulo Mineiro e sua correlação com áreas adjacentes. Tese de Doutorado, Inst. Geociências e Ciências Exatas, UNESP, Rio Claro, 183 p.

Batezelli, A., 2017. Continental systems tracts of the Brazilian Cretaceous Bauru Basin and their relationship with the tectonic and climatic evolution of South America. Basin Res. 29, 1–25. https://doi.org/10.1111/bre.12128.

Batezelli, A., Ladeira, F.S.B., Nascimento, D.L., Silva, M.L., 2019. Facies and palaeosol analysis in a progradational distributive fluvial system from the Campanian-Maastrichtian Bauru Group, Brazil. Sedimentology 66, 699-735. https://doi.org/10.1111/sed.12507.

Beauvais, A., Bonnet, N.J., Chardon, D., Arnaud, N., Jayananda, M., 2016. Very long-term stability of passive margin escarpment constrained by $^{40}Ar/^{39}Ar$ dating of K-Mn oxides. Geology 44, 299–302. https://doi.org/10.1130/G37303.1.

Beauvais, A., Chardon, D., 2013. Modes, tempo, and spatial variability of Cenozoic cratonic denudation: The West African example. Geochemistry, Geophysics, Geosystems 14, 1590-1608. https://doi.org/10.1002/ggge.20093.

Beauvais, A., Ruffet, G., Hénocque, O., Colin, F., 2008. Chemical and physical erosion rhythms of the West African Cenozoic morphogenesis: The ^{39}Ar-^{40}Ar dating of supergene K-Mn oxides. Journal of Geophysical Research 113, F04007. doi:10.1029/2008JF000996.

Behling, H., 2002. South and southeast Brazilian grasslands during Late Quaternary times: a synthesis. Palaeogeogr. Palaeoclimatol. Palaeoecol. 177, 19-27. https://doi.org/10.1016/S0031-0182(01)00349-2.

Bezerra, F.H.R., Castro, D.L., Maia, R.P., Sousa, M.O.L., Moura-Lima, E.N., Rossetti, D.F., Bertotti, G., Souza, Z.S., Nogueira, F.C.C., 2020. Postrift stress field inversion – implications for the petroleum system in the Potiguar Basin and evolution of the equatorial margin of South America. J. Mar. Petrol. Geol. 111, 88–104. https://doi.org/10.1016/j.marpetgeo.2019.08.001.

Bierman, P.R., Caffee, M., 2001. Slow rates of rock surface erosion and sediment production across the Namib Desert and escarpment, southern Africa. Am. J. Sci. 301, 326-358. https://doi.org/10.2475/ajs.301.4-5.326.

Bishop, P., 1995. Drainage rearrangement by river capture, beheading and diversion. Progress in Physical Geography 19, 449-473. https://doi.org/10.1177/030913339501900402.

Bishop, P., 2007. Long-term landscape evolution: linking tectonics and surface processes. Earth Surf. Proc. Land. 32, 329-365. https://doi.org/10.1002/esp.1493.

Bishop, P., Goldrick, G., 2010. Lithology and the evolution of bedrock rivers in post-orogenic settings: constraints from the high-elevation passive continental margin of SE Australia, Geol. Soc. Spec. Publ. 346, 267–287. https://doi.org/10.1144/SP346.14.

Bonnet, N.J., Beauvais, A., Arnaud, N., Chardon, D., Jayananda, M., 2014. First $^{40}Ar/^{39}Ar$ dating of intense Late Palaeogene lateritic weathering in Peninsular India. Earth Planet. Sc. Lett. 386, 126–137. http://dx.doi.org/10.1016/j.epsl.2013.11.002.

Bonnet, N.J., Beauvais, A., Arnaud, N., Chardon, D., Jayananda, M., 2016. Cenozoic lateritic weathering and erosion history of Peninsular India from $^{40}Ar/^{39}Ar$ dating of supergene K–Mn oxides. Chem. Geol. 446, 33–53. http://dx.doi.org/10.1016/j.chemgeo.2016.04.018.

Braun, O.P.G., 1971. Contribuição à geomorfologia do Brasil Central. Revista Brasileira de Geografia 32, 3–39.

Chadwick, R., Boutle, I., Martin, G., 2013. Spatial patterns of precipitation change in CMIP5: Why the rich do not get richer in the tropics. Journal of Climate 26, 803–3822. https://doi.org/10.1175/JCLI-D-12-00543.1.

Cobbold, P.R., Meisling, K.E., Mount, V.S., 2001. Reactivation of an obliquely rifted margin, Campos and Santos Basins, Southeastern Brazil. AAPG Bulletin 85, 1925–1944. https://doi.org/10.1306/8626D0B3-173B-11D7-8645000102C1865D.

Cogné, N., Gallagher, K., Cobbold, P.R., Riccomini, C., Gautheron, C., 2012. Post-breakup tectonics in southeast Brazil from thermochronological data and combined inverse-forward thermal history modeling. J. Geophys. Res. 117, B11413. https://doi.org/10.1029/2012JB009340.

Cordani, U.G., Ramos, V.A., Fraga, L.M., Cegarra, M., Delgado, I., Souza, K.G., Gomes, F.E.M., Schobbenhaus, C., 2016. Tectonic map of South America=Mapa tectónico de América del Sur=Mapa tectônico da América do Sul. http://rigeo.cprm.gov.br/xmlui/handle/doc/16750 (accessed 20 June 2021).

CPRM - Serviço Geológico do Brasil, 2014. Mapa geológico do estado de Minas Gerais. Belo Horizonte: CPRM. Escala 1:1.000.000.

DiBiase, R.A., Whipple, K.X., Heimsath, A.M., Ouimet, W.B., 2010. Landscape form and millennial erosion rates in the San Gabriel Mountains, CA. Earth Planet. Sc. Lett. 289, 134-144. https://doi.org/10.1016/j.epsl.2009.10.036, 2010.

Egholm, D.L., Knudsen, M.F., Sandiford, M., 2013. Lifespan of mountain ranges scaled by feedbacks between landsliding and erosion by rivers. Nature 498, 475–478. https://doi.org/10.1038/nature12218.

Ferrier, K.L., Perron, J.T., Mukhopadhyay, S., Rosener, M., Stock, J.D., Huppert, K.L., Slosberg, M., 2013. Covariation of climate and long-term erosion rates across a steep rainfall gradient on the Hawaiian island of Kaua'i. GSA Bull. 125, 1146–1163. https://doi.org/10.1130/B30726.1

Flint, J.J., 1974, Stream gradient as a function of order, magnitude, and discharge, Water Resour. Res. 10, 969-973. https://doi.org/10.1029/WR010i005p00969.

Fonseca, A.C.L., Novo, T.A., Nachtergaele, S., Fonte-Boa, T.M.R., van Ranst, G., de Grave, J., 2021. Differential Phanerozoic evolution of cratonic and non-cratonic lithosphere from a thermochronological perspective: São Francisco Craton and marginal orogens (Brazil). Gondwana Research 93, 106-126. https://doi.org/10.1016/j.gr.2021.01.006.

Forte, A.M., Whipple, K.X., 2019. Short communication: The Topographic Analysis Kit (TAK) for TopoToolbox. Earth Surf. Dynam. 7, 87–95. https://doi.org/10.5194/esurf-7-87-2019.

Gallen, S.F., 2018. Lithologic controls on landscape dynamics and aquatic species evolution in post-orogenic mountains. Earth Planet. Sc. Lett. 493, 150-160. https://doi.org/10.1016/j.epsl.2018.04.029.

Gallen, S.F., Thigpen, J.R., 2018. Lithologic controls on focused erosion and intraplate earthquakes in the eastern Tennessee seismic zone. Geophysical Research Letters 45, 9569–9578. https://doi.org/10.1029/2018GL079157.

Gallen, S.F., Wegmann, K.W., Bohnenstiehl, D.R., 2013. Miocene rejuvenation of topographic relief in the southern Appalachians. GSA Today 23, 4-10, https://doi.org/10.1130/GSATG163A.1.

Goudie, A.S., 2006. The Schmidt Hammer in geomorphological research. Progress in Physical Geography 30, 703–718. https://doi.org/10.1177/0309133306071954.

Hack, J.T., 1957. Studies of longitudinal stream profiles in Virginia and Maryland: U.S. Geological Survey Professional Paper 294-B, 45–97.

Hack, J.T., 1960. Interpretation of erosional topography in humid temperate regions. Am. J. Sci. 258, 80-97.

Hack, J.T., 1975. Dynamic equilibrium and landscape evolution, in: Melhorn, W.N., Flemal, R.C. (Eds.), Theories of landform development. State University of New York Press, Binghamton, NY, USA, pp. 87-102.

Hack, J.T., 1982. Physiographic divisions and differential uplift in the Piedmont and Blue Ridge, United States Geological Survey Professional Paper 1265, US Geological Survey, Washington, D.C.

Hancock, G., Kirwan, M., 2007. Summit erosion rates deduced from 10 Be: Implications for relief production in the Central Appalachians. Geology 35, 89-92. https://doi.org/10.1130/G23147A.

Harel, M.A., Mudd, S.M., Attal, M., 2016. Global analysis of the stream power law parameters based on worldwide ^{10}Be denudation rates. Geomorphology, 268, 184-196. https://doi.org/10.1016/j.geomorph.2016.05.035.

Hasui, Y., Haralyi, N.L.E., 1991. Aspectos Litoestruturais e Geofísicos do Soerguimento do Alto Paranaíba. Revista Geociências 10, 67-77.

Heimsath, A.M., Chadwick, O.A., Roering, J.J., Levick, S.R., 2020. Quantifying erosional equilibrium across a slowly eroding, soil mantled landscape. Earth Surf. Process. Landforms 45, 499–510. https://doi.org/10.1002/esp.4725.

Hergarten, S., Robl, J., Stüwe, K., 2016.Tectonic geomorphology at small catchment sizes – extensions of the stream-power approach and the χ-method. Earth Surface Dynamics 4, 1–9. https://doi.org/10.5194/esurf-4-1-2016.

Howard, A.D., 1965. Geomorphological systems — equilibrium and dynamics. Am. J. Sci. 263, 302-312. https://doi.org/10.2475/ajs.263.4.302.

Jean, A., Beauvais, A., Chardon, D., Arnaud, N., Jayananda, M., Mathe, P.E., 2020. Weathering history and landscape evolution of Western Ghats (India) from 40Ar/39Ar dating of supergene K–Mn oxides. Journal of the Geological Society 177, 523–536. https://doi.org/10.1144/jgs2019-048.

Johnston, A. C., Coppersmith, K. J., Kanter, L.R., Cornell, C.A., 1994. The earthquakes of stable continental regions. Assessment of large earthquake potential, TR-102261, Schneider, J.F., (Ed.), Electric Power Research Institute (EPRI), Palo Alto, CA.

King, L.C., 1956. A geomorfologia do Brasil oriental. Rev. Bras. Geogr. 18, 147–266.

Kirby, E., Whipple, K.X., 2012. Expression of active tectonics in erosional landscapes. J. Struct. Geol., 44, 54-75. https://doi.org/10.1016/j.jsg.2012.07.009.

Liu, Y., Konietzky, H., 2018. Particle-based modeling of pull-apart basin development. Tectonics 37, 343–358. https://doi.org/10.1002/2017TC004685.

Macedo, J., Bryant, R.B., 1987. Morphology, Mineralogy, and Genesis of a Hydrosequence of Oxisols in Brazil. Soil Sci. Soc. Am. J. 51, 690-698.

Mandal, S.K., Lupker, M., Burg, J.P., Valla, P.G., Haghipour, N. and Christl, M., 2015. Spatial variability of ^{10}Be-derived erosion rates across the southern Peninsular Indian escarpment: A key to landscape evolution across passive margins. Earth Planet. Sc. Lett. 425, 154-167. https://doi.org/10.1016/j.epsl.2015.05.050.

Mantovani, M., Quintas, M.C.L., Shukowsky, W., Neves, B.B.B., 2005. Delimitation of the Paranapanema Proterozoic Block: a geophysical contribution. Episodes 28, 18-22. https://doi.org /10.18814/epiiugs/2005/v28i1/002.

Marangoni, Y.R., Mantovani, M.S.M., 2013. Geophysical signatures of the alkaline intrusions bordering the Paraná Basin. Journal of South American Earth Sciences 41, 83-98. https://doi.org/10.1016/j.jsames.2012.08.004.

Marques, F.O., Nikolaeva, K., Assumpção, M., Gerya, T.V., Bezerra, F.H.R., Nascimento, A.F., Ferreira, J.M., 2013. Testing the influence of far-field topographic forcing on subduction initiation at a passive margin. Tectonophysics 608, 517–524. https://doi.org/10.1016/j.tecto.2013.08.035.

Matmon, A., Crouvi, O., Enzel, Y., Bierman, P., Larsen, J., Porat, N., Amit, R., Caffee, M., 2003. Complex exposure histories of chert clasts in the late Pleistocene shorelines of Lake Lisan, Southern Israel. Earth Surf. Proc. Land. 28, 493–506. https://doi.org/10.1002/esp.454.

McFarlane, M.J., 1976. Laterite and Landscape. Academic Press, London.

Miller, S.R., Sak, P.B., Kirby, E. and Bierman, P.R., 2013. Neogene rejuvenation of central Appalachian topography: Evidence for differential rock uplift from stream profiles and erosion rates. Earth Planet. Sc. Lett. 369, 1-12, https://doi.org/10.1016/j.epsl.2013.04.007.

Monteiro, H.S., Vasconcelos, P.M., Farley, K.A., Spier, C., Mello, C., 2014. (U–Th)/He geochronology of goethite and the origin and evolution of Cangas. Geochim. Cosmochim. Acta 131, 267–289. http://dx.doi.org/10.1016/j.gca.2014.01.036.

Monteiro, H.S., Vasconcelos, P.M.P., Farley, K.A., 2018. A combined (U-Th)/He and cosmogenic ^{3}He record of landscape armoring by biogeochemical iron cycling. J. Geophys. Res.: Earth Surface, 123, 298-323. https://doi.org/10.1002/2017JF004282.

Montgomery, D.R., 2001. Slope distributions, threshold hillslopes, and steady-state topography. Am. J. Sci. 301, 432-454. https://doi.org/10.2475/ajs.301.4-5.432.

Montgomery, D.R., Brandon, M.T., 2002. Topographic controls on erosion rates in tectonically active mountain ranges. Earth Planet. Sc. Lett. 201, 481-489. https://doi.org/10.1016/S0012-821X(02)00725-2.

Moraes Rocha, L.G., Pires, A.C.B., Carmelo, A.C., Araújo Filho, J.O., 2014. Geophysical characterization of the Azimuth 125º lineament with aeromagnetic data: Contributions to the geology of central Brazil. Precambrian Research 249, 273–287.http://dx.doi.org/10.1016/j.precamres.2014.05.005.

Moraes Rocha, L.G.M., Correa, R.T., Silva, A.B., Matos, D.R., 2019. Geophysical reassessment of the Azimuth 125° Lineament: emplacement model and propagation of its dikes. Journal of the Geological Survey of Brazil 2, 87-98. https://doi.org/10.29396/jgsb.2019.v2.n1.6.

Motta, P.E.F., Carvalho Filho, A., Ker, J.C., Pereira, N.R., Carvalho Junior, W., Blancaneaux, P., 2002. Relações solo-superfície geomórfica e evolução da paisagem em uma área do Planalto Central Brasileiro. Pesquisa Agropecuária Brasileira 37, 869–878.

Mudd, S.M., Attal, M., Milodowski, D.T., Grieve, S.W., Valters, D.A., 2014. A statistical framework to quantify spatial variation in channel gradients using the integral method of channel profile analysis, J. Geophys. Res.: Earth Surface, 119, 138-152. https://doi.org/10.1002/2013JF002981.

Mudd, S.M., Clubb, F.J., Gailleton, B., Hurst, M.D., 2018. How concave are river channels?. Earth Surf. Dynam. 6, 505-523. https://doi.org/10.5194/esurf-6-505-2018.

Nahon, D., 1986. Evolution of iron crusts in tropical landscapes. In: Colman, S.M., Dethier, D.P. (Eds) Rates of Chemical Weathering of Rocks and Minerals. Academic Press, New York, pp. 169-191.

Oliveira, P.E., Raczka, M., McMichael, C.N.H., Pinaya, J.L.D., Bush, M.B., 2020. Climate change and biogeographic connectivity across the Brazilian cerrado. Journal of Biogeography 47, 396-407. https://doi.org/10.1111/jbi.13732.

Pazzaglia, F.J., Brandon, M.T., 1996. Macrogeomorphic evolution of the post-Triassic Appalachian Mountains determined by deconvolution of the offshore basin sedimentary record. Basin Research, 8, 255-278. https://doi.org/10.1046/j.1365-2117.1996.00274.x

Pazzaglia, F.J., Brandon, M.T., 2001. A fluvial record of long-term steady-state uplift and erosion across the Cascadia forearc high, western Washington State. American Journal of Science 301, 385-43.

Peifer, D., Persano, C., Hurst, M.D., Bishop, P., Fabel, D., 2021. Growing topography due to contrasting rock types in a tectonically dead landscape. Earth Surf. Dynam. 9, 167–181. https://doi.org/10.5194/esurf-2020-68.

Perron, J.T., Royden, L., 2013. An integral approach to bedrock river profile analysis. Earth Surf. Proc. Land. 38, 570-576. https://doi.org/10.1002/esp.3302.

Peyerl, W.R.L., Salamuni, E., Sanches, E., Nascimento, E.R., Santos, J.M., Gimenez, V.B., Silva. C.L., Farias, T.F.S., 2018. Reativation of Taxaquara Fault and its morphotectonic influence on the evolution of Jordão River catchment, Paraná, Brasil. Braz. J. Geol. 48, 553-573. https://doi.org/10.1590/2317-4889201820170110.

Portenga, E.W., Bierman, P.R., 2011. Understanding Earth's eroding surface with 10Be. GSA Today 21, 4-10. https://doi.org/10.1130/G111A.1.

Prince, P.S., Spotila, J.A., 2013. Evidence of transient topographic disequilibrium in a landward passive margin river system: knickpoints and paleo-landscapes of the New River basin, southern Appalachians. Earth Surf. Process. Landforms 38, 1685–1699. https://doi.org/10.1002/esp.3406.

Prince, P.S., Spotila, J.A., Henika, W.S., 2011. Stream capture as driver of transient landscape evolution in a tectonically quiescent setting. Geology 39, 823–826. https://doi.org/10.1130/G32008.1.

Quigley, M., Sandiford, M., Fifield, K., Alimanovic, A., 2007. Bedrock erosion and relief production in the northern Flinders Ranges, Australia, Earth Surf. Proc. Land. 32, 929-944. https://doi.org/10.1002/esp.1459.

Reinhardt, L.J., Bishop, P., Hoey, T.B., Dempster, T.J., Sanderson, D.C.W., 2007. Quantification of the transient response to base-level fall in a small mountain catchment: Sierra Nevada, southern Spain. J. Geophys. Res. 112, F03S05. https://doi.org/10.1029/2006JF000524.

Riccomini, C., 1997. Arcabouço estrutural e aspectos do tectonismo gerador e deformador da Bacia Bauru no estado de São Paulo. Revista Brasileira de Geociências 27, 153-162.

Riccomini, C., Velázquez, V.F., Gomes, C.B., 2005. Tectonic controls of the Mesozoic and Cenozoic alkaline magmatism in central-southeastern Brazilian Platform, in: Comin-Chiaramonti, P., Barros, C. (Eds.), Mesozoic to Cenozoic alkaline magmatism in the Brazilian platform. EDUSP/FAPESP, São Paulo, pp. 31-56.

Rodriguez, E., Morris, C.S., Belz, J.E., Chapin, E.C., Martin, J.M., Daffer, W., Hensley, S., 2005. An assessment of the SRTM topographic products. Technical Report JPL D-31639, Jet Propulsion Laboratory, Pasadena, California.

Scharf, T.E., Codilean, A.T., De Wit, M., Jansen, J.D., Kubik, P.W., 2013. Strong rocks sustain ancient postorogenic topography in southern Africa. Geology 41, 331-334. https://doi.org/10.1130/G33806.1.

Scherler, D., Schwanghart, W., 2020. Drainage Divide Networks Part 2: Response to Perturbations. Earth Surf. Dynam. 8, 261-274. https://doi.org/10.5194/esurf-8-261-2020.

Schulte, S.M., Mooney, W.D., 2005. An updated global earthquake catalogue for stable continental regions: reassessing the correlation with ancient rifts. Geophys. J. Int. 161, 707–721. doi: 10.1111/j.1365-246X.2005.02554.x.

Schwanghart, W., Scherler, D., 2014. TopoToolbox 2 – MATLAB-based software for topographic analysis and modeling in Earth surface sciences. Earth Surf. Dynam. 2, 1-7. https://doi.org/10.5194/esurf-2-1-2014.

Schwanghart, W., Scherler, D., 2017. Bumps in river profiles: uncertainty assessment and smoothing using quantile regression techniques. Earth Surf. Dynam. 5, 821-839. https://doi.org/10.5194/esurf-5-821-2017.

Schwanghart, W., Scherler, D., 2020. Divide mobility controls knickpoint migration on the Roan Plateau (Colorado, USA). Geology 48, 698–702. https://doi.org/10.1130/G47054.1.

Selby, M.J., 1993. Hillslope materials and processes. Second ed. Oxford University Press, New York.

Sgarbi, G.N.C., Dardenne, M.A., 1996. Evolução climática do Gondwana nas regiões centro-sul do brasil e seus registros geológicos continentais durante o Mesozóico, enfatizando o Arco do Alto Paranaíba, a borda NNE da bacia do Paraná e a porção meridional da bacia Sanfranciscana, no oeste do estado de Minas Gerais. Geonomos 4, 21-49. https://doi.org/10.18285/geonomos.v4i1.193.

Silva, V.P.A., 2017. A hidroelétrica de Nova Ponte-MG, Brasil, e a problemática dos deslocamentos compulsórios. Revista Território 24, 115-125. https://doi.org/10.14195/1647-7723_24_8.

Strikis, N.M., Cruz, F.W., Barreto, E.A.S., Naughton, F., Vuille, M., Cheng, H., Voelker, A.H.L., Zhang, H., Karmann, I., Edwards, R.L., Auler, A.S., Santos, R.V., Sales, H.R., 2018. South American monsoon response to iceberg discharge in the North Atlantic. PNAS 115, 3788-3793. https://doi.org/10.1073/pnas.1717784115.

Suppe, J., 1981. Mechanics of mountain building in Taiwan. Mem. Geol. Soc. China 4, 67-89.

Talwani, P., 2017. On the nature of intraplate earthquakes. J. Seismol. 21, 47–68. https://doi.org/10.1007/s10950-016-9582-8.

Talwani, P., 2014. Intraplate earthquakes. Cambridge University Press, New York.

Tardy, Y., 1993. Pétrologie des latérites et des sols tropicaux. Masson, Paris.

Tucker, G.E., van Der Beek, P., 2013. A model for post-orogenic development of a mountain range and its foreland. Basin Res. 25, 241-259. https://doi.org/10.1111/j.1365-2117.2012.00559.x.

Twidale, C.R., 1976. On the survival of paleoforms. Am. J. Sci. 276, 77-95. https://doi.org/10.2475/ajs.276.1.77.

van Arsdale, R., Bresnahan, R., McCallister, N., Waldron, B., 2007. Upland complex of the central Mississippi River valley: its origin, denudation, and possible role in reactivation of the New Madrid seismic zone, in: Stein, S., Mazzotti, S. (Eds.), Continental intraplate earthquakes: science, hazard, and policy issues. The Geol. Soc. Am. Special paper 425, pp. 177-192.

van Ranst, G., Pedrosa-Sorares, A.C., Novo, T., Vermeesch, P., de Grave, J., 2020. New insights from low-temperature thermochronology into the tectonic and geomorphologic evolution of the south-eastern Brazilian highlands and passive margin. Geoscience Frontiers 11, 303-324. https://doi.org/10.1016/j.gsf.2019.05.011.

Vasconcelos, P.M., Carmo, I.D.O., 2018. Calibrating denudation chronology through $^{40}Ar/^{39}Ar$ weathering geochronology. Earth-Sci. Rev. 179, 411-435. https://doi.org/10.1016/j.earscirev.2018.01.003.

Vasconcelos, P.M., Farley, K.A., Stone, J., Piacentini, T., Fifield, L.K., 2019. Stranded landscapes in the humid tropics: Earth's oldest land surfaces. Earth Planet. Sc. Lett. 519, 152-164. https://doi.org/10.1016/j.epsl.2019.04.014.

West, D.C., Mello, C.L., 2020. Distribuição da Formação Barreiras na região sul do Espírito Santo e sua relação com a deformação neotectônica. Rev. Bras. Geomorfol. 21, 155-170. http://dx.doi.org/10.20502/www.ugb.org.br rbg.v21i1.1667.

Whipple, K. X., 2001. Fluvial landscape response time: How plausible is steady-state denudation?. Am. J. Sci. 301, 313–325. https://doi.org/10.2475/ajs.301.4-5.313.

Whipple, K.X., Forte, A.M., DiBiase, R.A., Gasparini, N.M., Ouimet, W.B., 2017. Timescales of landscape response to divide migration and drainage capture: implications for the role of divide mobility in landscape evolution. J. Geophys. Res. Earth Surf. 122, 248-273. https://doi.org/10 10.1002/2016JF003973.

Whipple, K.X., Tucker, G.E., 1999. Dynamics of the stream-power river incision model: Implications for height limits of mountain ranges, landscape response timescales, and research needs. J. Geophys. Res.-Solid 104, 17661-17674. https://doi.org/10.1029/1999JB900120.

Widdowson, M.,1997. The geomorphological and geological importance of palaeosurfaces, *in* Palaeosurfaces: Recognition, Reconstruction and Palaeoenvironmental Interpretation, Spec. Publ. Geol. Soc., 120, 1–12.

Willett, S.D., Brandon, M.T., 2002. On steady states in mountain belts. Geology 30, 175-178. https://doi.org/10.1130/0091-7613(2002)030<0175:OSSIMB>2.0.CO;2.

Willett, S.D., Slingerland, R., Hovius, N., 2001. Uplift, shortening, and steady state topography in active mountain belts. Am. J. Sci. 301, 455–485. https://doi.org/10.2475/ajs.301.4-5.455.

Wobus, C., Tucker, G., Anderson, R.S., 2010. Does climate change create distinctive patterns of piedmont dissection?. J. Geophys. Res. 115, F04008. https://doi.org/10.1029/2009JF001562.

Wobus, C., Whipple, K.X., Kirby, E., Snyder, N., Johnson, J., Spyropolou, K., Crosby, B., Sheehan, D., 2006. Tectonics from topography: Procedures, promise, and pitfalls, in: Willett, S.D., Hovius, N., Brandon, M.T., Fisher, D.M. (Eds.), Tectonics, Climate, and Landscape Evolution. Geological Society of America Special Paper 398, Penrose Conference Series, pp. 55–74. https://doi.org/10.1130/SPE398.

Zachos, J., Pagani, M., Sloan, L., Thomas, E., Billups, K., 2001. Trends, Rhythms, and Aberrations in Global Climate 65 Ma to Present. Science 292, 686-693. https://doi.org/10.1126/science.1059412.

Zoback, M.L., 1992. First- and second-order patterns of stress in the lithosphere: The World Stress Map Project. J. Geophys. Res. 97, 11703. https://doi.org/10.1029/92JB00132.

3. SUPERGENE PHASES FROM FERRUGINOUS DURICRUSTS: NON-DESTRUCTIVE MICROSAMPLING AND MINERALOGY PRIOR TO DATING BY (U-TH)/HE

ABSTRACT

The interpretations of ages of supergene phases, such as iron oxides and oxyhydroxides, clearly depend on the appraisal of the complexity arising from their finely divided and polycrystalline nature at the microscopic scale. This study addresses a meaningful and critical issue for dating of hematite and goethite by the (U-Th)/He method: the mineralogical analysis prior to dating of the same grain. Mineralogy on single grains used for dating is not achievable by classical tools, such as conventional powder XRD (requiring at least some mg) or SEM (that can contaminate the grain by coating or fixing). Therefore, two samples from the pisolitic facies of a Brazilian ferruginous duricrust (Southwestern of the São Francisco craton, Minas Gerais State) were chosen because they presented a usual heterogeneity. In the pisolitic core and cortex, single grains (size circa 500 µm) were collected and powder samples were prepared in parallel by hand grinding and sieving at 100 µm. Samples were analyzed by high X-ray flux experiments such as laboratory rotating anode X-ray diffraction (RA-XRD) and synchrotron X-ray diffraction (SXRD). Rietveld refinement performed on grain patterns obtained from both RA-XRD and SXRD yielded similar values of the Hematite/(Hematite+Goethite) ratio. In addition, this ratio was consistently estimated by a previously proposed calibration curve based upon isolated XRD peaks for goethite and hematite. No effect of exposure time of RA-XRD was revealed on XRD patterns nor (U-Th)/He ages. Hence, inframillimetric, undisturbed grains can be used to analyze the mineralogy of ferruginous duricrusts by RA-XRD with a short exposure, and the same grains can subsequently be dated by (U-Th)/He method. The (U-Th)/He dating of pisolitic core and cortex grains also provided meaningful ages: they revealed two evolution phases of the ferruginous duricrust, which occurred at or before the Late Oligocene for pisolitic core and Middle to Late Miocene for pisolitic cortex, agreeing with the previous model for the development of pisoliths. The mineralogy of single grains selected for dating is helpful for discussing the crystallization ages, and the high-flux XRD approach may be applied to other supergene mineral parageneses used for absolute dating of weathering profiles.

Keywords: Iron oxides, X-ray diffraction, Synchrotron diffraction, Weathering geochronology.

3.1. Introduction

Ferruginous duricrusts, containing hematite and/or goethite as major components, consist in hard iron-rich horizons formed at or near the ground surface of laterites that are

widespread in intertropical areas (see e.g., Tardy, 1993). Their modes of formation have been extensively discussed in order to unravel the complexity arising from their polyphasic nature (McFarlane, 1976; Nahon, 1986; Nahon 1991; Tardy, 1993; Ollier and Sheth, 2008; Monteiro et al., 2014). In the landscape, they may represent paleosurfaces that partially resisted to erosion and weathering for long periods, down to Mesozoic (King 1956; Tardy and Roquin, 1998). In order to understand and reconstruct related continental surface evolution through time as a result of geodynamic or paleoclimate forcing, it is necessary to perform absolute dating of appropriate mineral components of ferruginous duricrusts, such as goethite and hematite (Tardy and Roquin, 1998; Theveniaut and Freyssinet, 1999; Theveniaut and Freyssinet, 2000; Allard et al., 2018; Monteiro et al., 2018; Vasconcelos et al., 2019). Through (U-Th)/He dating, the knowledge on their timing of formation is continuously increasing, but the chronology of ancient landscapes worldwide in relation to paleoclimate events is still fragmented and remains a topical issue (Shuster et al., 2005, Heim et al., 2006; Shuster et al., 2012; Vasconcelos et al., 2013; Monteiro et al., 2014; Allard et al. 2018; Monteiro et al., 2018; Vasconcelos et al., 2019; Albuquerque et al., 2020).

In the (U-Th)/He dating methodology, sample mineralogy is analyzed using conventional XRD and SEM on milli/microfacies first recognized to the naked eye or with a binocular magnifyer (e.g., Allard et al., 2018; Albuquerque et al., 2020). However, the finely divided nature of iron oxides and oxyhydroxides causes that even inframillimetric grains used for dating (typically less than 500 µm large, i.e., circa 0.25 mg for a goethite with spherical shape) can be polycrystalline and thus potentially exhibit different mineralogy from the sample analyzed beside with conventional XRD or SEM. This may induce some bias when discussing the dating results, especially when goethite and hematite correspond to contrasting ages according to the sampled microfacies (Anand and Gilkes, 1987; Alburquerque et al., 2020).

Classical mineralogical investigations cannot perform analyses on the same sample as the one independently used for (U-Th)/He dating: SEM can contaminate the grain by metal coating or fixing, and conventional powder XRD requires amounts of matter (at least several mg) much higher than that of a single grain extracted for (U-Th)/He dating. Consequently, in order to support interpretation and discussion of ages of iron oxides populations from ferruginous duricrusts using mineralogy, it appears critical to analyze the same single grain that will be subsequently used for (U-Th)/He dating. This can be potentially achieved using a powerful source of X-rays that is far beyond classical setups, such as those available with rotating anode (RA-XRD) or synchrotron X-ray diffraction (SXRD) facility.

Consequently, the present study objectives are twofold. First, it proposes to refine the mineralogical characterization of iron oxides and oxyhydroxides from ferruginous duricrusts on inframillimetric (≤500 µm), undisturbed grains prior to dating the same grains by (U-Th)/He method. On two natural samples from a Brazilian pisolithic duricrust, the RA-XRD patterns are compared to the better-resolved SXRD patterns. Related data allowed us to determine parameters that are useful for recognition of different generations between samples (e.g., sizes of mean coherent domain and Al-substitution) and the hematite/(hematite+goethite) ratio using either Rietveld fitting (Bish and Post, 1993) or an amplitude-based calibration curve upon isolated XRD peaks for goethite and hematite (Sanchez et al., 2021). Second, using this methodology, the (U-Th)/He ages of the cortex and core of the pisolitic sample from a Brazilian Fe-duricrust (Minas Gerais State) were determined and discussed as an example. Pisoliths are frequently observed in ferruginous duricrusts, may exhibit contrasting mineralogy between the core and cortex, and are thus relevant for the second aim of this study. This methodology is shown to be appropriate to evidence and quantify different Fe oxides and oxyhydroxides in a dated grain and also potentially to reveal mineral contaminants, provided that their concentration is high enough.

3.2. Material and methods

3.2.1. Location and description of the sampling

Low-relief uplands are preserved in ancient landscapes across the intertropical belt (Bardossy and Aleva, 1990; Scharf et al., 2013; Mandal et al., 2015; Heimsath et al., 2020; Peifer et al., 2021; Marques et al., 2021). Its preservation in the present-day landscape is often attributed to the slow erosion rate related to the stark contrast in lithology and relative tectonic quiescence (e.g., Beauvais and Chardon, 2013; Beauvais et al., 2016; Monteiro et al., 2018; Vasconcelos et al., 2019). The South America passive margin has been considered the least seismically active stable continental region in the world (Johnston et al., 1994; Schulte and Mooney, 2005; Talwani, 2014), and thick weathering profiles including duricrusts are partially preserved on remnants of paleosurfaces in slowly eroding humid tropical areas (e.g., Monteiro et al., 2018; Vasconcelos and Carmo, 2018; Vasconcelos et al., 2019).

A ferruginous duricrusts profile (~1,100 m elevation) at the Southwestern of the São Francisco craton (Minas Gerais State, Brazil) was chosen for sampling. It is developed at the expense of pyroclastic and epiclastic rocks from the Mata da Corda Group (Upper Cretaceous)

(CPRM, 2014). Despite being an important area of occurrence of thick weathering profiles at high elevations (Marques et al., 2021), no weathering geochronological data are available yet. The climate of the study area is Aw (Köppen–Geiger's classification), characterized by warm and seasonally dry winters, and moist and warm summers. The average annual rainfall is 1,600 mm and the mean annual temperature is 22 °C (Oliveira et al., 2020).

The morphological description of the profile was carried out based on McFarlane (1976), Tardy (1993) and Aleva (1994), and then non-disturbed samples were taken from all the described layers. Based on the morphological description at the fieldwork and lab, the pisolitic facies, which is often encountered in ferruginous duricrusts (Nahon, 1991; Tardy, 1993), was chosen due to being structurally suitable for dating, and also because it presented a usual complexity or heterogeneity allowing us to carry out our methodological approach.

3.2.2. Selection and preparation of samples

The morphological characteristics of a hand specimen from the pisolitic facies were observed and described using a binocular microscope. The populations of iron oxides were identified based on texture, color and morphology (e.g., Tardy, 1993), and then the pisoliths were individualized. The semi-quantitative composition of a complete pisolith was analyzed by a Zeiss Ultra55 Scanning Electron Microscope (SEM) with a FEG-Schottky electronic source coupled with an energy-dispersive spectrometer (EDS) facility. The working distance was at 7.5 mm and the acceleration voltage was at 15 kV.

Another pisolith with similar morphological characteristics and belonging to the same identified population was sampled using a diamond micro drill to divide the cortex and core. Grains (circa 500 µm large) were carefully selected from the cortex and core using an optical microscope. Some of grains were prepared by hand grinding using a mortar and pestle and then homogenized, and sieved at 100 µm in order to obtain powder samples (~0.50 mg). In the other selected grains (~0.10 mg), no preparation was carried out.

3.2.3. X-ray data collection and processing

The mineralogical analysis was performed in both powder and grain samples from the pisolitic cortex and core in transmission geometry on the samples loaded in a borosilicate capillary either as a filling for the powder or as a stuck-up for grain. A Rigaku MM007HF

diffractometer equipped with a RAXIS4++ image plate detector placed at a distance of 200 mm from the sample and a Mo rotating anode (0.70926 Å - 0.713609 Å) at 50 KeV and 24 mA were used for 60 min, with a range scan of 3-45 º2θ and a step size of 0.02 º2θ s^{-1}. The Fit2D program was used for the integration of 2D images into 1D patterns after a calibration with LaB6 standard. Rotating anode generators are the most powerful X-ray sources available in the laboratory. In these experimental setting operating under a high vacuum, a cooled rotating surface is continuously irradiated by the electron beam (Fig. 1), resulting in an improved signal-to-noise ratio and in the possibility to analyze small samples.

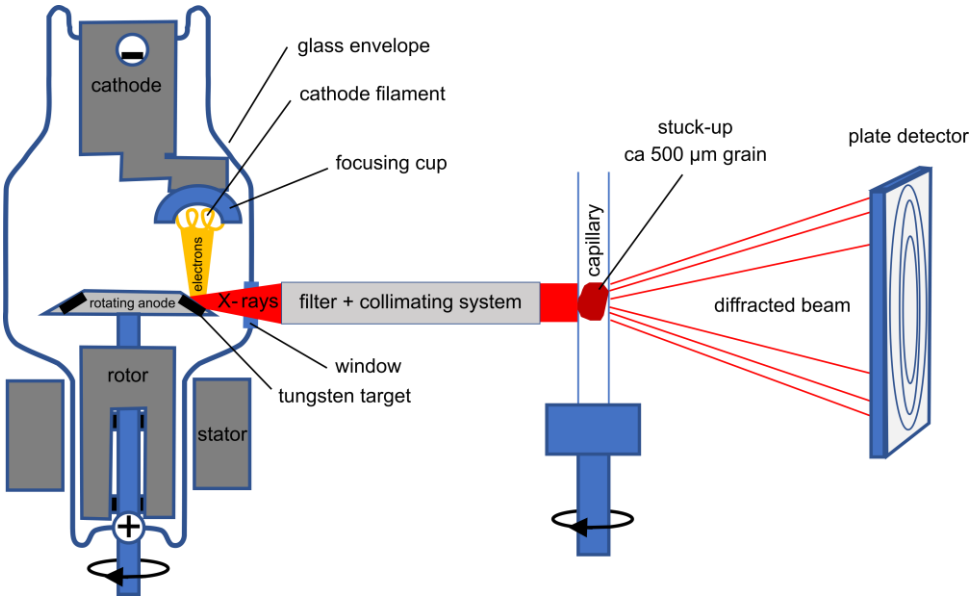

Figure 1. Diagram (out of scale) of the rotating anode X-ray diffraction device.

Higher X-ray fluxes require the use of a synchrotron facility. Therefore, SXRD patterns were collected on the same grains at the SOLEIL Synchrotron Facility, Orsay, France. It was used 2-circle diffractometer of the CRISTAL beamline, which is equipped with a MYTHEN2 X 9K detector (DECTRIS). The measurements were performed at 17 keV (0.72896 or 0.727913 Å) using 5 min exposure time, with a range scan of 3-65 º2θ and a step size of 0.04 º2θ s^{-1}.

The mineral phases of the grains and powder samples from the pisolitic cortex and core were identified from RA-XRD and SXRD patterns using the d-spacing according to Bragg's Law (Dixon and Weeds, 1989). The hematite/(goethite+hematite) ratio was estimated for powder and grain samples using an amplitude-based calibration curve upon isolated XRD

peaks, i.e., (020) goethite and (204) hematite (Sanchez et al., 2021). The sizes of Mean Coherent Domains (MCD) were calculated for grain samples using the Scherrer's equation (Klug and Alexander, 1954) taking into account the experimental width for correction of the instrumental error, considering the reflection peaks (020) and (111) of goethite, and (204) and (102) of hematite. The wt% ratio of the main phases of grain samples was determined by Rietveld refinement using the FullProf program (Rodriguez-Carvajal, 1993). When possible, the Fe/Al ratio for goethite and hematite was determined by Rietveld refinement and compared to its estimation using the empirical formula by Schulze (1984) for goethite and Schwertmann et al. (1979) for hematite. It allowed us to compare RA-XRD and SXRD data and evaluate the possibility of mineralogically characterizing grains prior to dating.

The undisturbed grains from the pisolitic core and cortex, and a reference sample of goethite were exposed to different exposure times (30, 60, 90 min) during RA-XRD recording, to find the best conditions for X-ray analysis and verify that (U-Th)/He dating was not biased by He diffusion.

3.2.4. (U-Th)/He dating

The grains previously analyzed for different acquisition times by RA-XRD were weighed, their size was measured, and then they were encapsulated into a niobium foil. One grain from each population without exposure to irradiation, including the reference sample, was also analyzed. Grains with circa 500 µm size were selected to avoid significant natural He losses out of the crystals (i.e., alpha ejection, He diffusion) (Farley et al., 1996; Shuster et al., 2005). The dating was performed by the (U-Th)/He method according to Gautheron et al. (2013), Allard et al. (2018) and Monteiro et al. (2018). The helium content of the encapsulated grains was analyzed using a Pfeiffer Prisma Quadrupole mass spectrometer in the Low-temperature Thermochronology Laboratory at GEOPS, Paris-Sud University, France. After this step, grains inside niobium foils were dissolved and their U, Th and Sm content was measured. Based on these data, the age of each population was calculated. Detailed information of procedures mentioned above is described by Shuster et al. (2005; 2012), Vasconcelos et al. (2013), Monteiro et al. (2014; 2018) and Allard et al. (2018).

3.3. Results and discussion

3.3.1. Morphological description

The ferruginous duricrust profile of the studied site (Fig. 2a) comprises basal pyroclastic and epiclastic rocks from the Upper Cretaceous transitioning upwards into a *sensu stricto* ferruginous duricrust (~400 cm), a pisolith-rich (~100 cm) and nodular indurated zone (~30 cm) (Fig. 2b). The pisoliths are well-formed, irregular in size and shape and range from 5 to 10 mm in diameter (Fig. 2c). They are separated one from the other by a matrix composed of goethite, kaolinite and quartz. The pisoliths present a concentric yellow-brown cortex that develops at the periphery of the purple-red nodule. The well-developed concentric cortex presents an alternation of light and dark banded zones (Fig. 2d), which the light rings have a higher Al and Si than Fe content (Fig. 2e), as often observed for pisoliths from duricrusts (Nahon, 1976; McFarlane, 1983; Amouric et al., 1986; Anand and Gilkes, 1987).

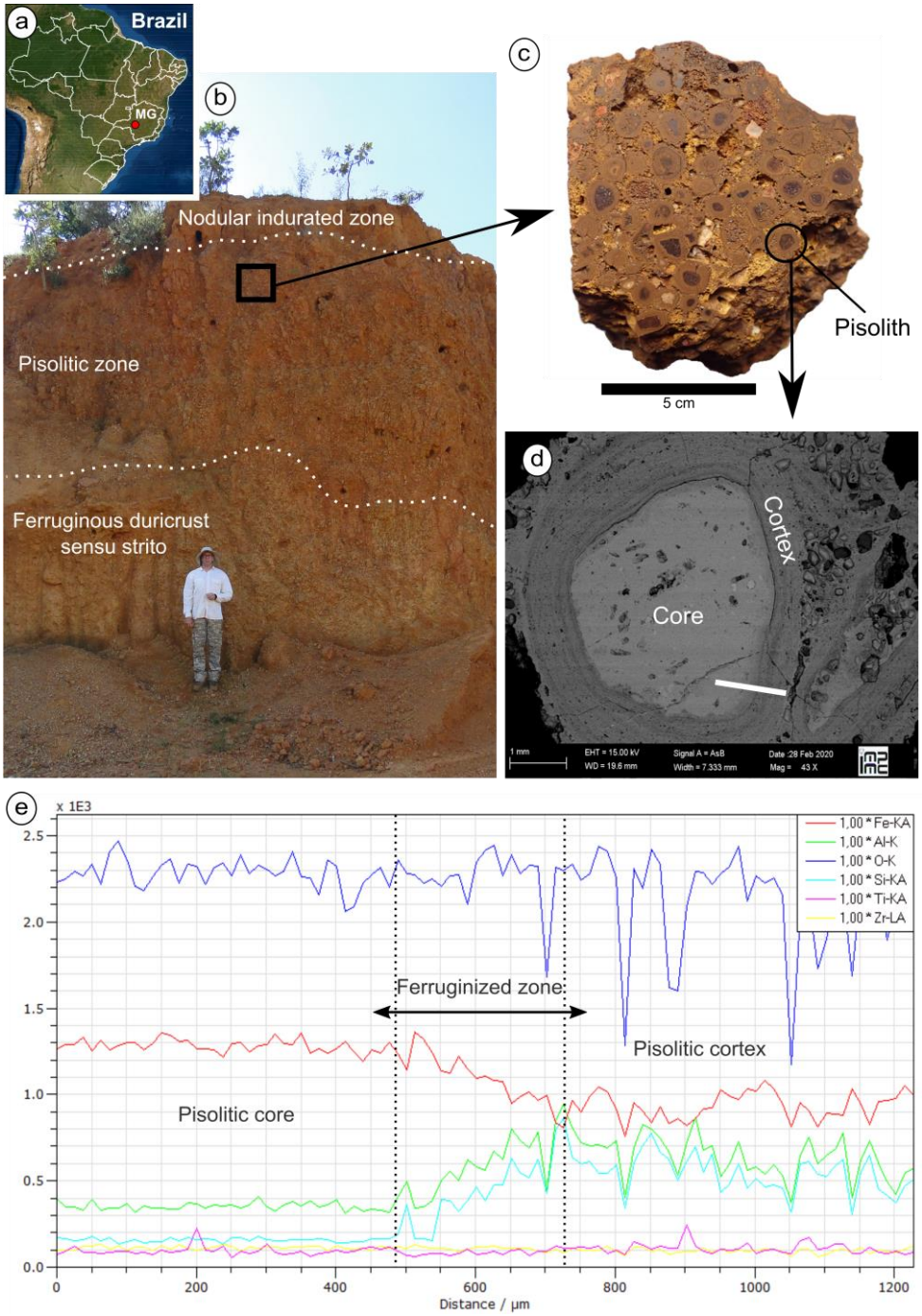

Figure 2. Ferruginous duricrusts profile and pisolitic facies, indicating the morphological characteristics and compositional variation. (a) Location of the Fe-duricrust profile in a Brazilian landscape, (b) distinct horizons of the profile, (c) pisolitic facies, (d) internal structure of a pisolith and (e) contrasting compositional variation from the core to cortex. Line white on the SEM image in painel d indicate of the transect analyzed and showed in painel e.

3.3.2. XRD data of the core and cortex from the pisolitic facies

3.3.2.1. Rotate anode-XRD patterns

Various assays of the RA-XRD acquisition of grain samples from both pisolitic core and cortex and a reference sample of goethite were carried out using 30, 60, and 90 min exposure times in order to evaluate the quality of signal/noise in XRD patterns and question the influence on He diffusion and age. The RA-XRD patterns of all three samples were similar with a very good signal-to-noise ratio. Consequently, a 60 min exposure time was chosen for RA-XRD in the following study, because it should provide good quality patterns for Rietveld refinement, even for phases with low concentration. The effect of exposure time on the He diffusion is approached in the final section.

The RA-XRD patterns for grain and powder samples from the pisolitic core and cortex are shown in Fig. 3, with assigned mineral contributions together with the indexation of the isolated peaks used for the determination of the Hm/(Hm+Gt) ratio, sizes of MCD, and Al-substitution. The grain- and powder-XRD patterns were dominantly similar, indicating that both types of sample preparation could be used to analyze the mineralogical composition in small amounts (Fig. 3). However, the intensity of some peaks appears different for powder and grain samples, suggesting that they do not have exactly the same mineralogical content. This is the case for the core sample for which the relative intensity of Hm peaks is greater in the grain pattern than in the powder preparation. This is interpreted as an effect of heterogeneity of Hm content in the selected core microfacies and fully justifies the benefit of analyzing the mineralogy of the same grain as the one used for subsequent (U-Th)/He dating, in order to help discussion of ages in case of mixed mineral compositions. Thus, this clearly indicates that the mineralogy of a single grain with ≤500 μm size can be analyzed with RA-XRD with a good signal/noise ratio and that subsequently the same grain can be retained without disturbance for further analysis.

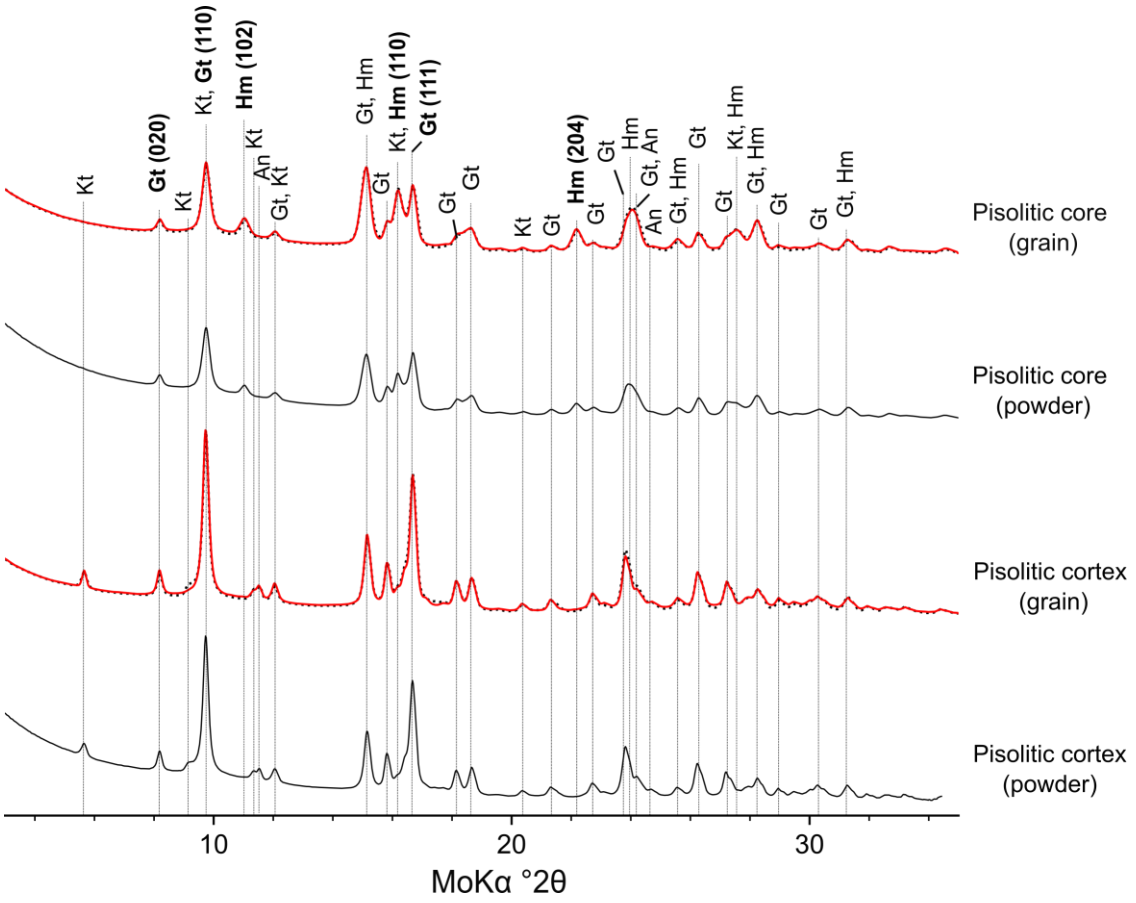

Figure 3. Rotating anode XRD patterns for grain and powder samples from the pisolitic core and cortex of the ferruginous duricrust. Gt: goethite, Hm: hematite, Kt: kaolinite and An: anatase. Note that the quality of the grain pattern is similar to that of the powder pattern. Red line represents the Rietveld fit.

The RA-XRD patterns indicate that hematite and goethite are present in the pisolitic core whereas goethite and kaolinite are present in the cortex, as revealed by the reflection peaks at 7.15 and 3.58 Å of kaolinite (Dixon and Weeds, 1989), which were not observed in the samples from the pisolitic core (Fig. 3). The absence of kaolinite in the pisolitic core is often related to its epigenetic replacement by hematite, which becomes more aluminous with the progressive dissolution of kaolinite (Nahon, 1976; Didier et al., 1983; Tardy and Nahon, 1985; Ambrosi et al., 1986). The reflection peak at 1.84 Å related to (204) of hematite was not observed in the RA-DRX patterns of the pisolitic cortex, regardless of the sample preparation method, indicating a low amount or absence of hematite, as confirmed by the Rietveld refinement (Tab. 1). The mineralogical composition of the pisolitic core and cortex is consistent with previous studies (Didier et al., 1985; Amouric et al., 1986; Tardy, 1993).

The Hm/(Hm+Gt) ratio estimated from RA-XRD patterns is shown in Tab. 1. In the grains, the values of the Hm/(Hm+Gt) ratio determined by Rietveld refinement and amplitude-based calibration are fully consistent, i.e., 0.41 and 0.39 in the core and 0.30 and 0.00 in the

cortex, respectively. This indicates that the pisolitic core contains ~40% of hematite and the pisolitic cortex is predominated by goethite (Tab. 1). In the core powder, the hematite content is lower, i.e., 25%, owing to the lesser amplitude of the peak at 1.84 Å (Fig. 3). The Hm/(Hm+Gt) ratio can be useful for investigating the ferruginous duricrust dismantling process and therefore it can be used as a proxy for the investigations of paleoclimate and weathering episodes (Didier et al., 1985; Tardy and Nahon, 1985).

The estimated values of the MCD sizes of hematite and goethite from RA-XRD for grain and powder samples arise from peak widths such as those reported in Fig. 3. There were differences for grain and powder samples of both pisolitic core and cortex, with higher values for powder samples (Tab. 1). This is thought to reveal the heterogeneity of crystallites present in the powder, which is revealed even using a small amount of matter. The alternative would be the result of grinding that may induce crystalline disorder (Buhrke et al., 1998). Concerning grains, the MCD size for core hematite is circa 144 Å, while goethite of the pisolitic core and cortex is circa 163 Å and 204 Å, respectively (Tab. 1). Goethite and hematite particles are generally smaller in laterites, with particle size ranges from 40 to 100 Å for hematite and 100 to 400 Å for goethite being commonly reported (e.g., Tardy and Nahon, 1985; Amouric et al., 1986; Anand and Gilkes, 1987). However, Didier (1983) and Amouric et al. (1986) reported hematite crystals ca. 400 Å by Mössbauer spectra and TEM, while MCD sizes for goethite crystals were observed according to the reported for other studies.

The Fe/Al determination from Rietveld refinement for the core grain was 10% for goethite and 30% for hematite, respectively (Tab. 1). The value for Al-hematite is far over the maximum value of Al-substitution for this mineral (i.e., 15%) (Cornell and Schwertmann, 2003). This was probably due to the weak number of isolated and relatively intense Hm peaks, which hinders an accurate Rietveld refinement. By comparison, the estimation of Al/Fe according to Schulze's formula was 8.5% for goethite and 1.1% for hematite of the pisolitic core, indicating the replacement of Al-hematite by Al-goethite, as often reported for pisoliths (Tardy and Nahon, 1985). On the other hand, the Al/Fe calculation using Rietveld refinement and Schulze's formula for cortex grain was 18% and 4.1% for goethite, respectively, which are possible values (i.e., <33%; Cornell and Schwertmann, 2006). In the studied samples, the Al-substitution on goethites assessed on RA-XRD patterns decreases from the core to the cortex as already observed in pisoliths from duricrusts (Didier et al., 1985; Tardy and Nahon, 1985; Nahon and Tardy, 1992), indicating the advanced evolution of pisoliths and thus the ferruginous duricrust dismantling (Didier et al., 1983).

Table 1. Mineralogical parameters determined for the core and cortex samples by Rietveld refinement and empirical calibrations using RA-XRD patterns: sizes of Mean Coherent Domains of the hematite and goethite, estimated Hm/(Hm+Gt) ratio, concentrations of main phases and Fe/Al ratio

Sample	RA-XRD-based									Rietveld refinement							
	Gt (020)		Gt (111)		Hm (204)		Hm (102)			IS[4]						Fe/Al ratio	
	d[1]	MCD[2]	d	MCD	d	MCD	d	MCD	Hm/(Hm+Gt)[3]	Gt	Hm	Hm	Gt	Kt	An	Gt	Hm
	Å									%mol		wt %					
									Pisolitic core								
Grain	4.97	192	2.44	133	1.84	134	3.68	154	0.39	8.5	1.1	41.24	58.76	0.00	0.00	90:10	70:30
Powder	4.96	231	2.44	148	1.84	143	3.68	166	0.25	7.4	0.0	nd	nd	nd	nd	nd	nd
									Pisolitic cortex								
Grain	4.96	231	2.45	176	*	*	*	*	0.00	4.1	*	0.3	94.45	2.7	2.54	82:18	*
Powder	4.96	302	2.45	193	*	*	*	*	0.00	5.9	*	nd	nd	nd	nd	nd	nd

[1] The interplanar space according to Bragg's Law; [2] Sizes of the Mean Coherent Domain according to Scherrer's formula; [3] Empirical calibration on Hm/(Hm+Gt) ratio (Sanchez et al., 2021); [4] Isomorphic substitution of Fe^{3+} by Al^{3+} according to Schulze (1984) for goethite and Schwertmann et al. (1979) for hematite. Hm: hematite; Gt: goethite; Kt: kaolinite; An: anatase; nd: not determined; * absent.

3.3.2.2. Synchrotron-XRD patterns

The synchrotron XRD patterns for the grain samples from the pisolitic core and cortex are shown in Fig. 4. The results were similar to those obtained by RA-XRD data concerning the signal/noise ratio and identified mineral phases. As expected, the synchrotron XRD patterns show a better resolution of diffraction peaks than RA-XRD (Figs. 3 and 4). It is related to the better-defined wavelength of the incident synchrotron radiation, which is useful for identifying minor constituents in a sample and even particles of small size (Lombi and Susini, 2009; Tsao et al., 2013). There was also a good fit that modeled all the peaks, except for kaolinite because stacking disorder was not accounted for the refinement (Fig. 4).

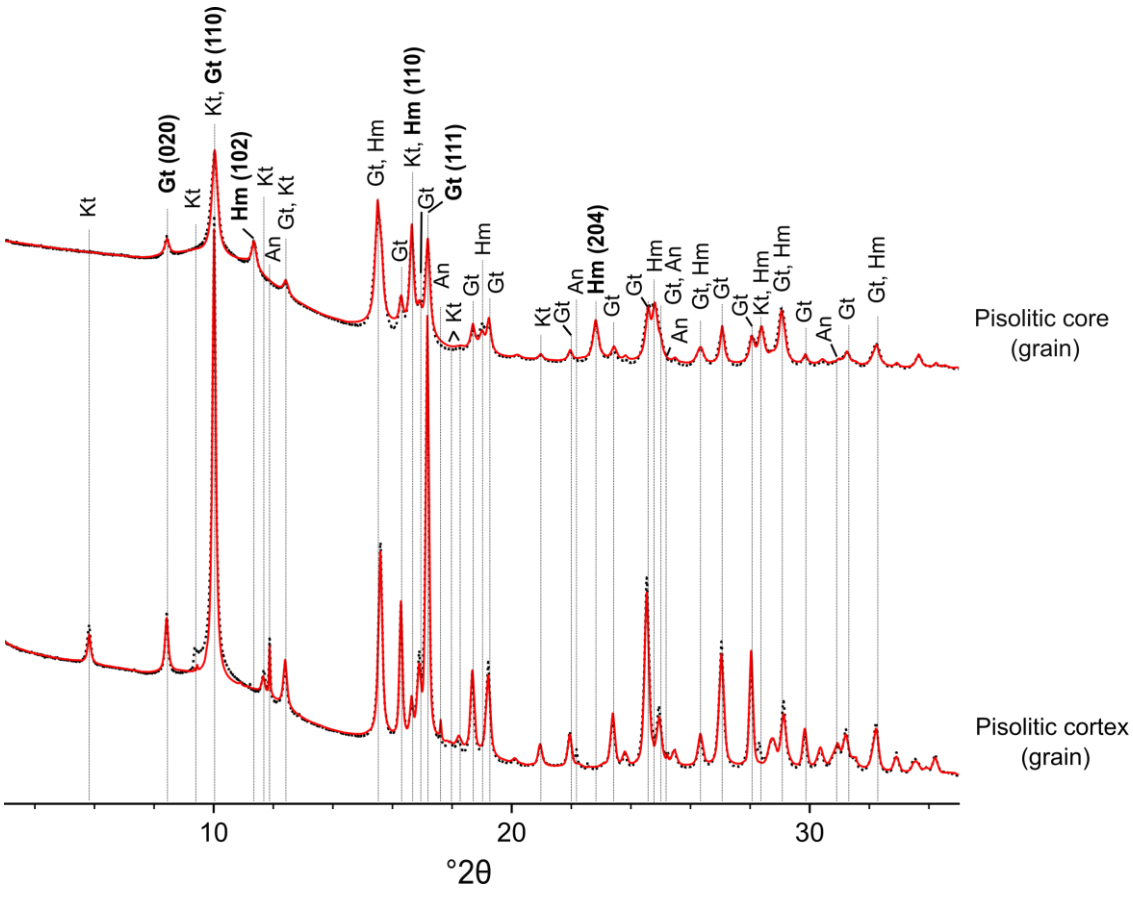

Figure 4. Synchrotron XRD patterns for grain samples from the pisolitic core and cortex. Gt: goethite, Hm: hematite, Kt: kaolinite, and An: anatase. Red line represents the Rietveld fit.

Comparing the crystallographic properties of mineral phases, the MCD sizes of hematite and goethite from the pisolitic core were slightly different by both XRD data,

considering the reflection of (020) of Gt and (204) of Hm. From the pisolitic cortex, MCD size of hematite and goethite was quite similar (Tab. 2). The difference may be related to the higher resolution and intensity of diffraction peaks from the SXRD, which influences the smaller peak width and therefore the MCD result (Fig. 4). The Hm/(Hm+Gt) ratio estimated from SXRD patterns for pisolitic core using grain sample was 0.39, the same value was obtained by RA-XRD data (Tabs. 1 and 2). This supports why the single grain analysis is appropriate also for Hm/(Hm+Gt) ratio, in addition to the investigation of the mineral phases and the MCD size. Furthermore, it also highlights that the calibration curve proposed by Sanchez et al. (2021) can be used for estimation of Hm/(Hm+Gt) ratio instead of Rietveld refinement, which is time-consuming and requires very well resolved patterns.

The estimation of the Fe/Al ratio in goethite was higher for SXRD data than RA-XRD using Rietveld refinement. The resulting value of Al-substitution in goethites was 35% for the core, which is a maximum value (Cornell and Schwertmann, 2006), and 15% for the cortex (Tab. 2). This is not consistent with the RA-XRD data (Tab. 1), but is more in agreement with the natural lowering of Al-substitution in goethites from the pisolitic cortex as a result of duricrust dismantling (Didier et al., 1983; Tardy and Nahon, 1985). The Schulze's calibration in contrast gave different values, with 12.3% and 10.5% for goethite in the pisolitic core and cortex, respectively.

Despite the different settings between RA-XRD and SXRD, both methods are suitable for investigating the mineralogical composition of supergene phases in small amounts (down to micrometric, circa 500 µm size). The RA-XRD, available in laboratories, is powerful enough to analyze undisturbed grains that can be subsequently used for dating, and thus appears much more appropriate than conventional XRD analysis, which does not provide quality data allowing quantitative mineralogy analysis even after a long exposure time (i.e., 15 hours).

Table 2. Mineralogical parameters determined for the core and cortex samples by Rietveld refinement and empirical calibrations synchrotron XRD patterns: sizes of Mean Coherent Domains of the hematite and goethite, estimated Hm/(Hm+Gt) ratio, concentrations of main phases and Fe/Al ratio

Sample	XRD-based											Rietveld refinement				
	Gt (020)		Gt (111)		Hm (020)		Hm (102)		Hm/(Hm+Gt)[3]	IS[4]		Hm	Gt	Kt	Fe/Al ratio	
	d[1]	MCD[2]	d	MCD	d	MCD	d	MCD		Gt	Hm				Gt	Hm
	Å									% mol		wt %			mol %	
	Pisolitic core															
Grain	8.43	259	2.44	178	1.84	162	3.67	181	0.39	12.3	6.7	32.17	67.83	0	65:35	nd
	Pisolitic cortex															
Grain	8.42	361	2.44	302	*	*	*		0	10.5	*	0.73	93.94	5.33	85:15	nd

[1] The interplanar space according to Bragg's Law; [2] Sizes of the Mean Coherent Domain according to Scherrer's formula; [3] Empirical calibration on Hm/(Hm+Gt) ratio (Sanchez et al., 2021); [4] Isomorphic substitution of Fe^{3+} by Al^{3+} according to Schulze (1984) for goethite and Schwertmann et al. (1979) for hematite. Hm: hematite; Gt: goethite; Kt: kaolinite; An: anatase; nd: not determined; * absent.

3.3.3. (U-Th)/He dating

The effect of exposure time of RA-XRD recording on apparent age for pisolitic core and cortex, and reference samples is shown in Fig. 5 and 6. For each sample, there is no representative shift in age related to the acquisition time of mineralogical data and the results showed reliable replicates within the analytical uncertainty, i.e., 10% (Shuster et al., 2005; Vasconcelos et al., 2013; Monteiro et al., 2014). Only one reference subsample (60 min exposure) showed an age lower than the others aliquots, but this is likely due to some heterogeneity of the reference goethite. This difference also exists on eU, hence this point is considered as an outlier, as also found by Monteiro et al. (2014) and Albuquerque et al. (2020) for grains belong the same population. Fig. 6 clearly shows that all the samples exhibit apparent age clusters including the 0 exposure point, supporting the possibility to perform mineralogical analysis by RA-XRD prior to dating the same grain by (U-Th)/He.

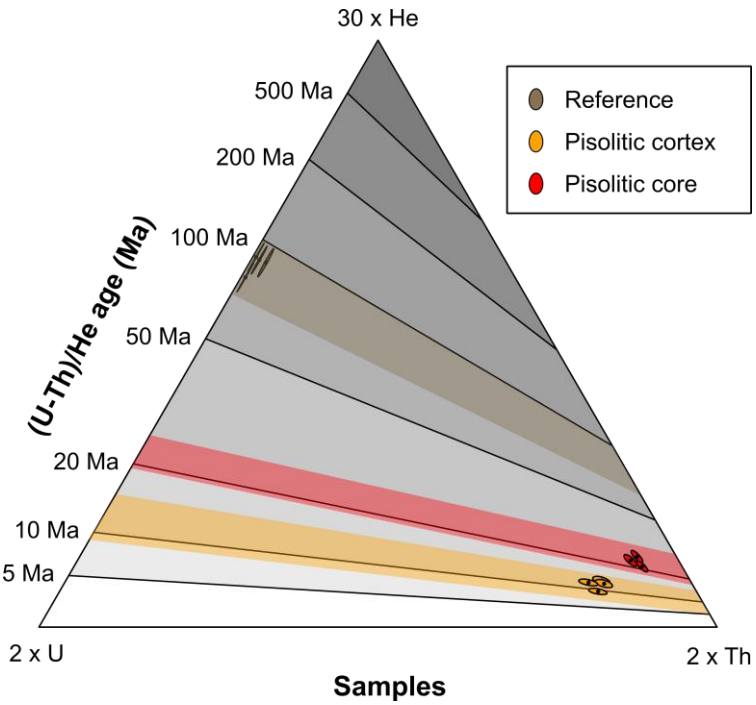

Figure 5. Ternary diagram indicating the He-Th-U concentrations and the (U-Th)/He age (Ma) for pisolitic core and cortex, and reference samples.

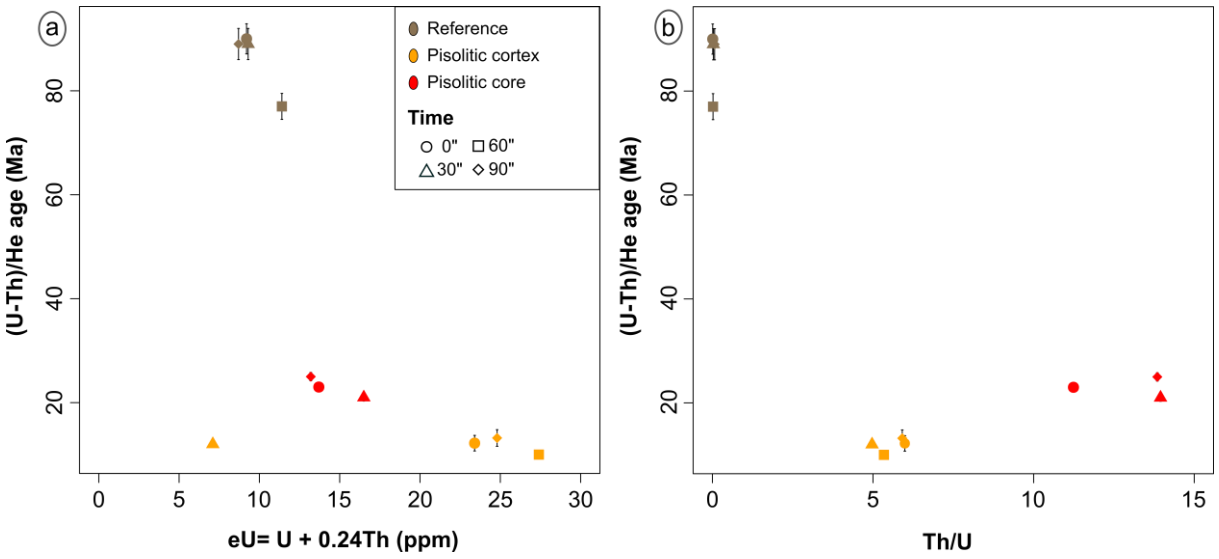

Figure 6. Effective uranium content (eU) (a) and Th/U ratio (b) as a function of (U-Th)/He age (Ma).

U and Th concentrations clearly differ between the pisolitic core and cortex (Fig. 6a), with higher values of both elements for the pisolitic cortex. In addition, Th/U decreases from the core to cortex (Fig. 6b), suggesting a relative enrichment of U during the weathering of the iron oxides and oxyhydroxides of the core, as also observed by Albuquerque et al. (2020) for lateritic pisoliths. A grain from the pisolitic cortex contains lower U and Th concentrations than other grains (Fig. 6a), which is possible to occur due to small differences between grains, as reported for grains of supergene minerals belonging to the same population (e.g., Monteiro et al., 2014; Albuquerque et al., 2020). Nevertheless, such difference has not influence age, which is similar to the other grains (Fig. 6).

(U-Th)/He ages for the pisolitic core range from 25.3±0.8 to 21.3±0.7 Ma and pisolitic cortex from 13.2±1.6 to 9.5±0.3 Ma (Fig. 6). The apparent age reveals that the pisolitic core is older than the pisolitic cortex which is fully in agreement with the model for the development of pisoliths from different localities, as proposed by several authors (see e.g., Didier et al., 1983; Didier et al., 1985; Tardy and Nahon, 1985; Nahon and Tardy, 1992). It must be pointed out that the core age may be an average age of the hematite and goethite, with hematite being possibly much older than goethite. Assuming that the goethite has the same age in the core as in the cortex and knowing the Hm/(Hm+Gt) ratio, the pure hematite average age would be ~41 Ma. The crystallographic parameters such as the MCD size and Fe/Al ratio of goethite in the core and cortex rather indicate that they formed in different conditions, but with no constraint

on the age. Thus, the formation episode of ferruginous duricrusts at the Southwestern of the São Francisco craton (Minas Gerais State, Brazil) occurred at or before the Oligocene.

Accordingly, Albuquerque et al. (2020) also found younger goethites in the pisolitic cortex than for hematite in the pisolitic core of pisolitic bauxites and fragmental ferruginous duricrust from the Southwestern Amazonia, Brazil. They pointed out that the ferruginous duricrust dismantling process, which is evidenced by the formation phase of the pisolitic cortex, took place in the Early to Late Miocene (~23 to 13 Ma) and therefore can be correlated to an epoch of extensive bauxite duricrust formation in the region. Our results suggest that the dismantling process of ferruginous duricrusts at Southeastern Brazil took place from the Middle to Late Miocene (~13.2 to 9.5 Ma), which is close to the finding by Albuquerque et al. (2020). Monteiro et al. (2014) reported that ferruginous duricrusts below ca. 1,550 m elevation in Southeastern Brazil, relatively close (~250 km) to our study area, yielded (U–Th)/He ages predominantly younger than 15 Ma and they are more prone to rejuvenation through goethite dissolution–reprecipitation.

Monteiro et al. (2014) pointed out that discrepancies in (U-Th)/He ages would be expected for samples with apparent age close to the lower limit of the method, greater ^{4}He loss, incorporation or loss of U and Th after goethite precipitation, contamination with primary minerals and coexistence of several generations in a single grain. Some of these factors cannot be detected before dating, but the primary minerals inclusions can be assessed satisfactorily using a powerful X-ray source, which cannot be achieved using a conventional powder XRD. This reinforces the importance of performing detailed mineralogical analysis of grains potentially suitable for (U-Th)/He dating. Further studies would need to be conducted to assess the potential of RA-XRD and SXRD in identifying minor constituents in supergene minerals prior to dating and their influence on ages.

3.4. Conclusion

Mineralogy of supergene minerals from core and cortex of lateritic pisoliths can be analyzed non-destructively by RA-XRD, with good quality of signal/noise on submillimetric (≤ 500 μm) single grains, which can be used subsequently retained without disturbance for further analysis. RA-XRD allows the estimation of Hm/(Hm+Gt) either by Rietveld refinement or using an amplitude-based calibration curve upon isolated XRD peaks for goethite and hematite amplitudes. SXRD patterns yielded similar results to the RA-XRD, but it is more appropriate for identifying minor constituents in a grain due to its better resolution. This

approach could potentially be applied to other mineral parageneses (e.g., Mn-oxides, jarosites) prior to dating. The exposure to X-rays was shown not to compromise the accuracy of the apparent age and thus the same grains used for mineralogical investigations can subsequently be dated by (U-Th)/He method.

Although concerning only a few grains, the (U-Th)/He ages reveal that a formation phase of ferruginous duricrusts at the Southwestern of the São Francisco craton (Minas Gerais State, Brazil) occurred at or before the Late Oligocene, which is recorded by the pisolitic core ages ranging from 25.3±0.8 to 21.3±0.7 Ma. A subsequent phase associated with the dismantling process of ferruginous duricrusts took place from the Middle to Late Miocene (~13.2 to 9.5 Ma), which is evidenced by the formation of the goethitic pisolitic cortex. Therefore, the apparent age by (U-Th)/He results reveals that the pisolitic core is older than pisolitic cortex, agreeing with the previously proposed model for the development of pisoliths in duricrusts.

References

Albuquerque, dos Santos M.F., Horbe, A.C., Danisik, M., 2020. Episodic weathering in southwestern Amazonia based on (U-Th-Sm)/He dating of Fe and Mn lateritic duricrust. Chemical Geology 553, 119792.

Aleva, G.J.J., 1994. Laterites: Concepts, Geology, Morphology and Chemistry. Wageningen (Netherlands), International Soil Reference and Information Centre. 169p.

Allard, T., Gautheron, C., Riffel, S.B., Balan, E., Soares, B.F., Pinna-Jamme, R., Derycke, A., Morin G., Bueno, G.T., Nascimento, N., 2018. Combined dating of goethites and kaolinites from ferruginous duricrusts. Deciphering the Late Neogene erosion history of Central Amazonia. Chemical Geology 479, 136-150.

Ambrosi, J.P., Nahon, D., Herbilon, A.J., 1986. The epigenetic replacement of kaolinite by hematite in laterite. Petrographic evidence and the mechanisms involved. Geoderma 37, 283-294.

Amouric, M., Baronneta., A., Nahon, D., Didier, P., 1986. Electron microscopic investigations of iron oxyhydroxides and accompanying phases in lateritic iron-crust pisolites. Clays Clay Minerals 34, 45-52.

Anand, R.R., Gilkes, R.J., 1987. Variations in the properties of iron oxides within individual specimens of lateritic duricrust. Aust. J. Soil Res. 25, 287-302.

Bárdossy, G., Aleva, G.J.J., 1990. Lateritic bauxites. Dev. Econ. Geol. 27. 624 p.

Beauvais, A., Bonnet, N.J., Chardon, D., Arnaud, N., Jayananda, M., 2016. Very long-term stability of passive margin escarpment constrained by $^{40}Ar/^{39}Ar$ dating of K-Mn oxides. Geology 44, 299–302.

Beauvais, A., Chardon, D., 2013. Modes, tempo, and spatial variability of Cenozoic cratonic denudation: The West African example. Geochemistry, Geophysics, Geosystems 14, 1590-1608.

Bish, D.L., Post, J.E., 1993. Quantitative mineralogical analysis using the Rietveld full-pattern fitting method. Amer. Miner. 78, 932–940.

Buhrke, V. E., Jenkins, R., Smith, D. K., 1998. A practical guide for the preparation of specimens for x-ray fluorescence and x-ray diffraction analysis. New York: Wiley-VCH.

Cornell R.M., Schwertmann U., 2006. The Iron Oxides: Structure, Properties, Reactions, Occurrences and Uses. 2nd Edition, Wiley-WCH, Weinheim.

CPRM - SERVIÇO GEOLÓGICO DO BRASIL, 2014. Mapa geológico do estado de Minas Gerais. Belo Horizonte: CPRM. Escala 1:1.000.000.

Didier, P., 1983. Paragenèses à oxydes et hydroxydes de fer dans les bauxites et les cuirasses ferrugineuses.Thèse 3e cycle, Univ. Poitiers, 150 p.

Didier, P., Nahon, D., Fritz, B., Tardy, Y., 1983. Activity of water as a geochemical controlling factor in ferricretes. A thermodynamic model in the system: kaolinite Fe-Al-oxihydroxides. Sei. Géol. Mérn. 71, 35 – 44.

Didier, P., Perret, D., Tardy, Y., Nahon, D., 1985. Equilibres entre kaolinites ferrifères, goethites alumineuses et hématites alumineuses dans les systèmes cuirasses rôle de l'activité de l'eau et de la taille des pores. Sci. Géol. Bull.38, 383-397.

Dixon, J.B., Weeds, S.B., 1989. Minerals in Soil Environments. Soil Science Society of America, Madison, WI.

Farley, K.A., Wolf, R.A., Silver, L.T., 1996. The effects of long alpha-stopping distances on (U-Th)/He ages. Geochimica et Cosmochimica Acta 60, 4223-4229.

Gautheron, C., Barbarand, J., Ketcham, R.A., Got, L.T., Beek, P.V., Pagel, M., Pinna-Jamme, R., Couffignal, F., Fialin, M., 2013. Chemical influence on α-recoil damage annealing in apatite: Implications for (U–Th)/He dating. Chemical Geology 351, 257–267.

Heim, J.A., Vasconcelos, P.M., Shuster, D.L., Farley, K.A. and Broadbent, G., 2006. Dating paleochannel iron ore by (U-Th)/He analysis of supergene goethite, Hamersley Province, Australia: Geology, 34, 173-176.

Heimsath, A.M., Chadwick, O.A., Roering, J.J., Levick, S.R., 2020. Quantifying erosional equilibrium across a slowly eroding, soil mantled landscape. Earth Surf. Process. Landforms 45, 499–510.

Johnston, A. C., Coppersmith, K. J., Kanter, L.R., Cornell, C.A., 1994. The earthquakes of stable continental regions: assessment of large earthquake potential, TR-102261, Vol. 1–5, ed. Schneider, J.F., Electric Power Research Institute (EPRI), Palo Alto, CA.

King, L.C., 1956. A geomorfologia do Brasil oriental. Rev. Bras. Geogr. 18, 147–266.

Klug, H.P., Alexander, L.E., 1974. X-ray Diffraction Procedures for Polycrystalline and Amorphous Materials. 2nd Ed. John Wiley & Sons: New York.

Lombi, E., Susini, J., 2009. Synchrotron-based techniques for plant and soil science: opportunities, challenges and future perspectives. Plant Soil 320, 1–35.

Mandal, S.K., Lupker, M., Burg, J.P., Valla, P.G., Haghipour, N. and Christl, M., 2015. Spatial variability of ^{10}Be-derived erosion rates across the southern Peninsular Indian escarpment: A key to landscape evolution across passive margins. Earth Planet. Sc. Lett. 425, 154-167.

Marques, K.P.P., Santos, M., Peifer, D., Silva, C.L., Vidal-Torrado, P., 2021. Transient and relict landforms in a lithologically heterogeneous post-orogenic landscape in the intertropical belt (Alto Paranaíba region, Brazil). Geomorphology 391, 107892.

McFarlane, M.J., 1976. Laterite and Landscape. Academic Press, London.149p.

McFarlane, M.J., 1983. Laterites. In: Goudie, A.S., Pye, K. (Eds) Chemical sediments and geomorphology. Academic Press, New York, pp. 7-58.

Monteiro, H.S., Vasconcelos, P.M.P., Farley, K.A., 2018. A combined (U-Th)/He(U-Th-Sm)/He and cosmogenic ^{3}He record of landscape armoring by biogeochemical iron cycling. Journal of Geophysical Research: Earth Surface 123, 298–323.

Monteiro, H.S., Vasconcelos, P.M.P., Farley, K.A., Spier, C.A., Mello, C.L., 2014. (U-Th)/He geochronology of goethite and the origin and evolution of cangas. Geochimica et Cosmochimica Acta 131, 267–289.

Nahon, D., 1976. Cuirasses ferrugineuses et encroûtements calcaires au Sénégal occidental et en Mauritanie. Mém. Sci. Géol. Strassbourg, 44:232 pp.

Nahon, D., 1986. Evolution of iron crusts in tropical landscapes. In: Colman, S.M., Dethier, D.P. (Eds) Rates of Chemical Weathering of Rocks and Minerals. Academic Press, New York, pp. 169-191.

Nahon, D., Tardy, Y., 1992. The ferruginous laterites. In: Butt, C.R.M., Zeegerds, H. (Eds) Regolith exploration geochemistry in tropical and subtropical terrains. Handbook of exploration geochemistry. Elsevier, Amsterdam, pp. 41-55.

Nahon, D.B., 1991. Introduction to the Petrology of Soils and Chemical Weathering. John Wiley & Sons, New York.

Oliveira, P.E., Raczka, M., McMichael, C.N.H., Pinaya, J.L.D., Bush, M.B., 2020. Climate change and biogeographic connectivity across the Brazilian cerrado. Journal of Biogeography 47, 396-407.

Ollier, C.D., Sheth, H.C., 2008. The High Deccan duricrusts of India and their significance for the "laterite" issue. Journal of Earth System Science 117, 537–551.

Peifer, D., Persano, C., Hurst, M.D., Bishop, P., Fabel, D., 2021. Growing topography due to contrasting rock types in a tectonically dead landscape. Earth Surf. Dynam. 9, 167–181.

Rodriguez-Carvajal, J., 1993. "Fullprof Program," Physica B. 192, 55-69.

Scharf, T.E., Codilean, A.T., De Wit, M., Jansen, J.D., Kubik, P.W., 2013. Strong rocks sustain ancient postorogenic topography in southern Africa. Geology 41, 331-334.

Schulte, S.M., Mooney, W.D., 2005. An updated global earthquake catalogue for stable continental regions: reassessing the correlation with ancient rifts. Geophys. J. Int. 161, 707–721.

Schulze, D.G., 1984. The influence of aluminium on iron oxides. VIII – unit-cell dimensions of Al-substituted goethites and estimation of Al from them. Clays Clay Miner. 32, 36-44.

Schwertmann, U., Fitzpatrick, R.W., Taylor, R.M., Lewis, D.G., 1979. The influence of aluminum on iron oxides. Part II. Preparation and properties of Al-substituted hematites. Clays Clay Miner. 27, 105–112.

Shuster, D.L., Farley, K.A., Vasconcelos, P.M.P., Balco, G., Monteiro, H.S., Waltenberg, K., Stone, J.O., 2012. Cosmogenic ^{3}He in hematite and goethite from Brazilian "canga" duricrust demonstrates the extreme stability of these surfaces. Earth and Planetary Science Letters 329-330, 41–50.

Shuster, D.L., Vasconcelos, P.M.P., Heim, J.A., Farley, K.A., 2005. Weathering geochronology by (U-Th)/He dating of goethite. Geochimica et Cosmochimica Acta 69, 659–673.

Talwani, P., 2014. Intraplate earthquakes. Cambridge University Press, New York.

Tardy Y., Roquin C, 1998. Dérive des continents. Paléoclimats et altérations tropicales. Éditions BGM, Orléans. 473p.

Tardy, Y. and Nahon, D., 1985. Geochemistry of laterites, stability of Al-goethite, Al-hematite and Fe^{3+}-kaolinite in bauxites and ferricretes: an approach of the mechanism of concretion formation. Am. J. Sci. 285, 865-903.

Tardy, Y., 1993. Pétrologie des latérites et des sols tropicaux. Masson, Paris. 461p.

Tardy, Y., Roquin, C., 1992. Geochemistry and evolution of lateritic landscapes. In: Martini, I.P., Chesworth, W. (Eds) Weathering, Soils & Paleosols. Developments in Earth Surface Processes 2. Elsevier, Amsterdam, pp. 407-443.

Théveniaut, H., Freyssinet, P., 1999. Paleomagnetism applied to lateritic profiles to assesssaprolite and duricrust formation processes: the example of Mon t Baduel profile (French Guiana). Palaeogeogr. Palaeoclimatol. Palaeoecol. 148, 209–231.

Théveniaut, H., Freyssinet, P., 2002. Timing of lateritization on the Guiana shield: synthesis of paleomagnetic results from French Guiana and Suriname. Palaeogeogr.Palaeoclimatol. Palaeoecol. 178 (1–2), 91–117.

Tsao, T., Chen, Y., Sheu, H., Tzou, Y., Chou, Y., Wang, M., 2013. Separation and identification of soil nanoparticles by conventional and synchrotron X-ray diffraction. Applied Clay Science 85, 1–7.

Vasconcelos, P.M., Carmo, I.D.O., 2018. Calibrating denudation chronology through $^{40}Ar/^{39}Ar$ weathering geochronology. Earth-Sci. Rev. 179, 411-435.

Vasconcelos, P.M., Farley, K.A., Stone, J., Piacentini, T., Fifield, L.K., 2019. Stranded landscapes in the humid tropics: Earth's oldest land surfaces. Earth and Planetary Science Letters 519, 152–164.

Vasconcelos, P.M.P., Heim, J.A., Farley, K.A., Monteiro, H., Waltenberg, K., 2013. $^{40}Ar/^{39}Ar$ and (U–Th)/He – $^{4}He/^{3}He$ geochronology of landscape evolution and channel iron deposit genesis at Lynn Peak, Western Australia. Geochimica et Cosmochimica Acta 117, 283–312.

4. CRYSTALLOGRAPHIC AND THERMAL PROPERTIES OF KAOLINITE AND GIBBSITE OF FERRALSOLS DEVELOPED IN DISTINCT LANDFORMS AND PARENT MATERIALS (SOUTHERN CENTRAL PLATEAU, SE BRAZIL)

ABSTRACT

Ancient landscapes in humid and semi-humid tropical climate conditions are frequently covered by highly weathered soils, known as Ferralsols. Although they have been extensively studied worldwide in the last sixty years, there is a dominance of studies focused on the first two meters of soils that often reach several tens of meters thick until contact with saprolite or rock and thus several issues concerning the soil evolution could remain oversimplified. Therefore, our main objective was to investigate the variation of the mineralogical composition and crystallographic properties of the main mineral species of clay fraction, and the thermal properties of kaolinite and gibbsite of Ferralsols developed in a tropical wet and dry ancient landscape at the Southern Central Plateau, Alto Paranaíba region, Minas Gerais State, Brazil. Eight soil profiles over two landforms at different elevations and parent materials were systematic sampling reaching several meters deep and particle size distribution, chemical and mineralogical analyses, including crystallographic and thermal properties, were carried out. The soils developed in the upper and relict landform, known as S*ul-Americana surface* in the classic literature, are much thicker than those in the transient and younger landform. Ferralsols are highly weathered in both landforms and present geric properties, but their mineralogical composition is not dominated by gibbsite and iron oxides/oxyhydroxides as expected. Instead, an increase in the amounts of kaolinite in depth in soils developed in the relict landform and relatively similar amounts of kaolinite and gibbsite in depth in soils in the transient landform were observed, which amounts of gibbsite were roughly higher in soils developed in the transient than those in the relict landforms. In addition, kaolinites with a higher structural disorder and gibbsites more crystalline were observed in soils developed in the transient landform, contrasting to expected for soils developed in a young landform. Such variation of the proportions of minerals in clay fraction, and their crystallographic and thermal properties can be interpreted as influenced more due to distinct weathering conditions prevailing at the present time of their formation and the different parent materials than the exposure time of the surface.

Keywords: Tropical weathering; Mean coherent domain sizes; Dehydroxylation temperature; iron oxides.

4.1. Introduction

Highly and long-term weathered soils recognised as either ferralitic or lateritic soils may be classified as Oxisols (Soil Survey Staff, 2014), Ferralsols (IUSS Working Group WRB,

2015), or Latossolos in the Brazilian Soil Classification System (Santos et al., 2018). Many of them have been developed under distinct weathering periods for sometimes for millions of years over different elevations, landforms and lithologies in humid and semi-humid tropical climate conditions (e.g., Chauvel and Pedro, 1978a; Bittom and Novikoff, 1991; Macedo and Bryant, 1987; Tardy and Roquin, 2000; Mathian et al., 2020). The weathering conditions that prevailed during their formation are recorded in their mineralogy, which may be an archive to decipher the major paleoclimates when appropriately constrained their formation by dating methods of secondary minerals (e.g., Balan et al., 2005; Fritsch et al., 2011; Monteiro et al., 2018; Mathian et al., 2019; Allard et al., 2020).

The occurrence of Ferralsols (term used hereinafter) in ancient landscapes under humid or semi-humid tropical climates is predominant. Regarding the Brazilian territory, where its occurrence is widespread (~33%), Ferralsols are widely reported as occurring in the distinct landforms which are recognised by King (1956) as Sul-Americana Surface (SAS; upper landform) supposedly from the Upper Cretaceous and Oligocene and Velhas Surface (VS; lower landform) supposedly from the Neogene (King, 1956; Braun, 1971; Motta et al., 2002), although no geochronological data are widely available to support such age range. The upper landform and other analogous in the intertropical zone have been covered by thick highly and long-term weathered profiles including duricrusts, and distinct weathering periods have influenced its evolution (Beauvais, 2009; Monteiro et al., 2018; Jean et al., 2019; Mathian et al., 2019; Vasconcelos et al., 2019). However, there are still few studies that reveal the influence of these periods on the processes that operated or are currently underway in soils developed in ancient landscapes.

The general trend of progressive weathering under tropical climate conditions is towards the residual accumulation of iron and aluminum oxyhydroxides: the ferralitization (e.g., Muller, 1972; Chauvel and Pedro, 1978b; Herbillon, 1980). However, varying proportions of gibbsite, kaolinite, iron oxides/oxyhydroxides, and frequently minor accessory minerals have been observed in highly weathered soils in the intertropical zone (Tardy et al., 1991; Curi and Franzmeier, 1984; Furian et al., 2002; Muggler et al., 2007; Mathian et al., 2020). It is well known that the amounts and characteristics of kaolinite and gibbsite are governed by the extent to which desilication occurs and weathering conditions prevailing at the present time of their formation (Muller, 1982; Nahon, 1986; Macedo and Bryant, 1987; Tardy et al., 1991; Fritsch et al., 2005). Therefore, the increase of the amounts of gibbsite from the bottom to the top is commonly observed with the advance of weathering. However, high amounts of gibbsite can

also occur in depth, which is often related to its formation in saprolite (e.g., Watanabe et al., 2006; Herrmann et al., 2007; Muggler et al., 2007).

It is well reported the predominance of gibbsite in Ferralsols developed in the upper and older landform and kaolinite in those developed in the lower and younger ones (Ker, 2002; Motta et al., 2002; Gomes et al., 2004; Reatto et al., 2008), suggesting a relationship between apparent age of the landform and intensity of weathering. However, a very deep Ferralsol profile (~800 cm) developed in the upper landform and studied by Macedo and Bryant (1987) may exemplify that variation of the amounts of kaolinite and gibbsite occur in depth and the consensus of similar amounts of the clay minerals in great depth for highly weathered soils may be questioned. As many studies have been carried out in the first two meters of soils that often reach several tens of meters thick until contact with saprolite or rock (e.g., Reatto et al., 2008; Rolim Neto et al., 2009), several issues about them remain oversimplified. Indeed, certain soils which are products of recent weathering can coexist in the same landscape and even in the same profile (Nahon, 2003), and restrict investigations to the upper sola makes them difficult to distinguish.

The identification of the mineralogical composition, estimation of the amounts of individuals minerals in clay fraction, and degree of crystallinity are commonly assessed via conventional X-ray diffraction (XRD) for its perceived availability. Such approach is very useful when minerals are well-ordered, but it is less promising for short-range ordered minerals as well as those with small crystallite size (Klug and Alexander, 1954; Brown and Brindley, 1980; Dixon and Weeds, 1989). Therefore, several limitations in an XRD-based approach when used for highly weathered soils arise, such as: 1) many reflections are absent or very weak to be measured; 2) reflections of different clay minerals may be superimposed; and 3) many of the proposed methods for assessing the crystallographic properties were empirically obtained considering standard minerals, which are well-ordered and thus different from those commonly found in soils (e.g., Hinckley, 1963; Mitra, 1963; Hughes and Brown, 1979; Plançon et al., 1988).

Other techniques for evaluation of minerals in clay fraction have been used (e.g., Mössbauer spectroscopy, thermogravimetry and differential thermal analysis, isotopic composition, electron paramagnetic resonance, infrared spectroscopy, and transmission electron microscopy) and insights from the mineralogy of highly weathered soils have emerged (e.g., Girard et al., 2000; Mathian et al., 2020; Allard et al., 2020). Among them, the upwards replacement of an old population of well-ordered kaolinites with large particle size by a more recent population of disordered kaolinites with smaller particle size has been verified in

Ferralsols from Amazon Basin (Fritsch et al., 2002; Balan et al., 2005; Balan et al., 2007; Mathian et al., 2020) and over an ancient landscape in Minas Gerais State, Brazil (Muggler et al., 2007). Therefore, the direction of weathering and the conditions that prevailed during its formation cannot be adequately revealed by the composition of the clay fraction itself assessed via XRD patterns.

Our main objective was to investigate the variation of the mineralogical composition and crystallographic properties of the main mineral species of clay fraction, and the thermal properties of kaolinite and gibbsite in Ferralsols developed in a tropical wet and dry ancient landscape (Southern Central Plateau, Minas Gerais State, Brazil). Eight sites located on two landforms at different elevations and parent materials were selected and systematic sampling reaching several meters deep was carried out. The weathering conditions that prevailed during the soil formation were discussed considering the different factors and then compared with those of other intertropical regions where Ferralsols are predominant.

4.2. Methods

4.2.1. Study site and soil profiles

The study area is located at the Southern Central Plateau (Alto Paranaíba region, Minas Gerais State, Brazil), nested within the Neoproterozoic Brasília Orogenic Belt, which is situated between São Francisco and Paranapanema Cratons. Topographically the area is characterised by relict landforms up to 1,000 m surrounded by transient landforms at valley bottoms (Marques et al., 2021) (Fig. 1a). The Quebra-Anzol (QA) catchment was chosen as the study area, due to be the largest (~10,600 km²) complete catchment in the Alto Paranaíba region (Fig. 1b). The climate of the study area is tropical (Aw – Köppen–Geiger's classification), characterised by warm and seasonally dry winters and moist and warm summers, with an average annual rainfall of 1,600 mm and a mean annual temperature of 22 °C (Oliveira et al., 2020). The native vegetation is characterised by a predominance of different Brazilian savanna phytophysiognomies (Oliveira et al., 2020), but some enclaves of Semideciduous Tropical Forest are also present. Currently, most of the area is cultivated with cereals, cotton, pastures, coffee, and horticulture.

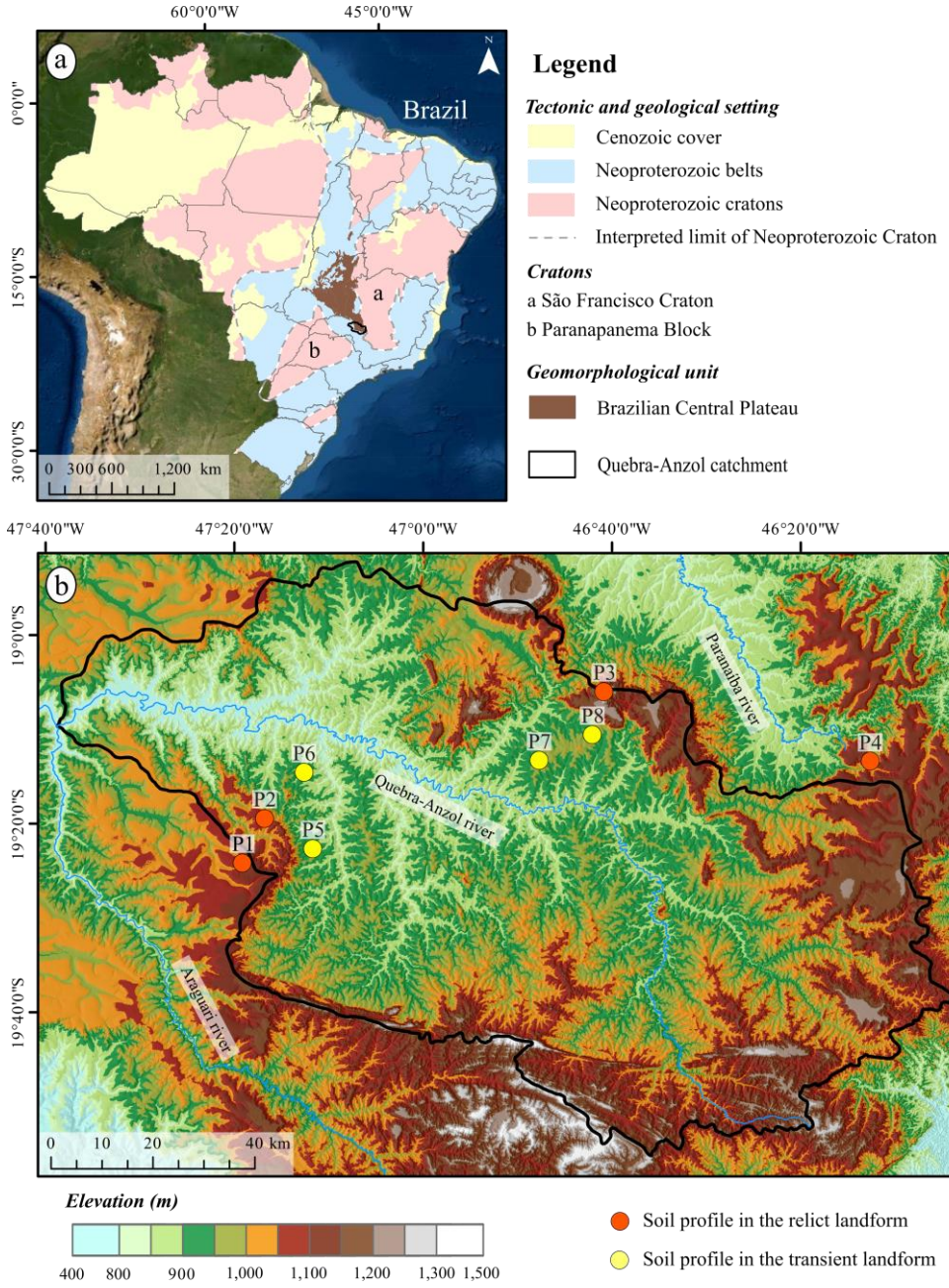

Figure 1. Study site. (a) Simplified tectonic and geological setting of the South American Platform (adapted from Cordani et al., 2016) and (b) hypsometric map of the Quebra-Anzol catchment, indicating the location of the studied soil profiles.

Eight sites for studies at scale of soil profiles were selected in the QA catchment, which were chosen to cover the lithological variability and landforms in which the Ferralsols are developed in the study area. Four sites were located in the relict landform (identified as P1, P2, P3, and P4), and the other four in the transient landform (identified as P5, P6, P7, and P8) (Fig. 1b). In some portions of the relict landform, Ferralsols are observed covering ferruginous duricrusts (i.e., P2 and P4). In general, Ferralsols in the relict landform are usually reported as

developed from Cenozoic deposits with low or no genetic relationship with the underlying bedrock (Ferreira et al., 1999; Motta et al., 2002; Marques et al., 2004; Reatto et al., 2008; Rolim Neto et al., 2009), but no evidence of lithologic discontinuity was observed. Ferralsols in the transient landform are developed from underlying metamorphic rocks, being P5 and P6 from mica schists of the Araxá Group and P7 and P8 from chlorite-quartz-muscovite schists of the Rio Verde Formation (CPRM, 2014) (Tab. 1).

Table 1. Topographic conditions and parent material of the selected sites

Pedon	Elevation (m)	Slope (%)	Parent material[1]
P1	~1,100	<2	Cenozoic deposits
P2	~1,100	~3	Cenozoic deposits
P3	~1,250	<2	Cenozoic deposits
P4	~1,130	<5	Cenozoic deposits
P5	~930	~3	Mica schists
P6	~930	~3	Mica schists
P7	~970	~3	Chlorite-quartz-muscovite schists
P8	~970	~3	Chlorite-quartz-muscovite schists

[1] According to the geological map from CPRM (2014) and previously mentioned studies.

Trenches were excavated with a hydraulic excavator until ~10 m in P1 and P3, and until the contact with the saprolite in P5, P6, P7, and P8 (<5 m). P2 and P8 are sites of exploration of ferruginous duricrusts and therefore there were recently excavated outcrops, having less than 5 m thick, so they were used in this study. Soil description and sampling were carried out in the field, according to soil description procedures by FAO guidelines (2006) and Santos et al. (2015), and soil profiles were classified according to IUSS Working Group WRB (2015).

4.2.2. Soil sampling and analyses

Disturbed soil samples were collected from each pedogenetic horizon, except in P2 and P8, which samples were collected only in few horizons due to the difficulty of sampling. The soil samples were oven-dried in the lab at 40°C, ground, and sieved (<2 mm) for particle size distribution, chemical and mineralogical analyses. Particle size distribution by soil separates was performed using 40 g of material, 50 ml of 1 mol L-1 NaOH as dispersing agent, and deionised water, and then samples were mechanically agitated by 16h. The total sand fraction (0.05-2 mm) was sieved, the clay fraction (<0.002 mm) was measured using a hydrometer according to the Stokes' law, and the silt fraction (0.002 - 0.05 mm) was obtained by the difference (Gee and Or, 2002). Chemical analyses were performed as follows: pH in H2O and KCl (1:2.5), exchangeable aluminum (Al^{3+}), calcium (Ca^{2+}), and magnesium (Mg^{2+}) extracted by KCl solution 1 mol L^{-1}, exchangeable sodium (Na^{+}) and potassium (K^{+}) extracted by Mehlich-1, and potential acidity (H + Al) extracted by calcium acetate solution of 0.5 mol L^{-1} at pH 7. The soil analyses were performed according to current Brazilian Soil Survey methods (Teixeira et al., 2017). Such results were used to calculate sum of exchangeable bases ($S = Ca^{2+} + Mg^{2+} + K^{+} + Na^{+}$), cation exchange capacity at pH 7 ($CEC = Ca^{2+} + Mg^{2+} + K^{+} + Na^{+} + H^{+} + Al^{3+}$), and base saturation status (V = [S/CEC]*100). Organic carbon content was determined according to Walkley and Black (1934).

4.2.3. X-ray diffraction measurement

Samples of the clay fraction from selected soil horizons of each soil profile were prepared following the method described by Mehra and Jackson (1960) and Jackson (1979). After the elimination of organic matter with the addition of 15% H_2O_2, extractions with citrate-bicarbonate-dithionite (CBD) of sodium at 65 ºC for 10 min in a water bath were performed six times to remove the free iron oxides. The Fe content from the CBD residue was determined by an Inductively Coupled Plasma Optical Emission Spectrometer (ICP-OES) and then Fe_2O_3 content was calculated. Furthermore, X-ray diffraction (XRD) patterns of the deferrated oriented slides samples were obtained using a Panalytical X'Pert3 Powder device with CuKα radiation, operating at 40 kV and 40 mA, with a range scan of 4-65 º2θ and a step size of 0.02 º2θ s^{-1}.

Iron oxides were concentrated after the elimination of silicate minerals and gibbsite using 5 mol L-1 NaOH under heating at ~250ºC for 120 minutes, according to the procedures

of Norrish and Taylor (1961) modified by Kämpf and Schwertmann (1982). Sodium metasilicate was added to reach 0.2 mol L^{-1} Si concentration in solution to avoid Fe oxide dissolution with high Al-substitution (Kämpf and Schwertmann, 1982). Sodalite [Na4Al3Si3O12(OH)] formed during extraction was removed by washing twice with 50 mL of 0.5 mol L−1 HCl solution and washing once with 50 mL of deionised water (Norrish and Taylor, 1961; Singh and Gilkes, 1991). XRD patterns of random powder samples were obtained using the previous settings described, but with a range scan of 10-60 º2θ and a step size of 0.01 º2θ s^{-1}.

4.2.4. Crystallographic properties

The mineral species of the clay fraction were identified from the XRD patterns using the d-spacing according to Bragg's Law (Brown and Brindley, 1980; Dixon and Weeds, 1989). The Asymmetry Index (AI) of the (001) diffraction peak of kaolinite was obtained by drawing a perpendicular line considering the sharpest point and measuring the Width at Half Height (WHH) to the right and the left of the peak, according to Melo and Wypych (2009). The Mean Coherent Domain (MCD) sizes of the main mineral species were calculated using the Scherrer's equation (Klug and Alexander, 1954), considering the (001) peak of kaolinite and (002) of gibbsite from XRD patterns of deferrated clay samples, and (110) of goethite and (104) of hematite from XRD patterns after elimination of silicates and gibbsite. The Average Number of Layers (ANL) of kaolinite was calculated by dividing the corresponding MCD sizes by the (001) value. The Al-substitution was calculated from *a* cell parameter of hematite as proposed by Schwertmann et al. (1979) and *c* cell parameter of goethite according to Schulze (1984). The goethite and hematite ratio [Gt/(Gt+Hm)] was estimated based on the peak area of (110) goethite and (104) hematite due to the low intensity of the (111) goethite or (110) hematite, according to the equation proposed by Torrent and Cabedo (1986) and also used by Melo et al. (2020).

4.2.5. Estimation of the amounts of kaolinite and gibbsite

Simultaneous thermogravimetric and differential thermal analysis (TG-DTA) was performed in clay samples after CBD treatment in order to eliminate interferences with iron oxides that present overlapping dehydroxylation reactions in similar temperature ranges

(Karathanasis, 2008). The thermogravimetric analysis was carried out using ~10 mg of soil sample which were placed in platinum crucibles and heated from room temperature to 950°C at 10°C min^{-1} under an N_2 atmosphere with the gas flow at 50 ml min^{-1}. The heating temperature and its respective weight loss were recorded using a thermogravimetric analyzer, model DTG-60 (Shimadzu Corporation, Japan). A standard poorly ordered kaolinite (KGa – 2 sample) was used to verify the precision of the measurement. The amounts of kaolinite and gibbsite were estimated according to Eqs. 1 and 2, respectively.

$$\%\ kaolinite = \left(\frac{\text{wl}}{13.95} * 100\right) * \text{c} \qquad \text{(Eq. 1)}$$

$$\%\ gibbsite = \left(\frac{\text{wl}}{34.62} * 100\right) * \text{c} \qquad \text{(Eq. 2)}$$

Where wl is the weight loss in % corresponding to the dehydroxylation temperature of kaolinite (~480°C) and gibbsite (~260°C) and c is the weight loss during the CBD treatment.

4.3. Results

4.3.1. Soil characterization and classification

Morphological description, horizon designation and classification of all soil profiles are shown in Tabs. 2 and 3. The soils developed in the relict landform are much deeper than those in the transient ones. P1 and P3 had a thickness greater than 10 m while P2 and P4 have less than 5 m thick. The soils developed in the transient landform in contrast showed contact with the saprolite within 3 m thick.

Table 2. Morphological description of the soils developed in the relict landform

Hz[1]	Depth (cm)	Color[2]	Structure[3]			Consistence[4]		Boundary
			Grade	Type	Size	Moist	Wet	
Profile 1 - Geric Ferralsol (Dystric, Clayic)[5]								
Ap	0-24	5YR 3/4	WE	GR	FI-ME	VFR	PL/ST	Clear
AB	-42	5YR 4/6	WE	SB	ME	VFR	PL/ST	Clear
BA	-63	2,5YR 4/8	WE/ST	SB/GR	ME/FI	VFR	PL/ST	Gradual
Bo1	-110	2,5YR 4/8	WE/ST	SB/GR	ME/FI	VFR	VPL/VST	Diffuse
Bo2	-168	2,5YR 4/8	WE/ST	SB/GR	ME/FI	FR	VPL/VST	Diffuse
Bo3	-210	2,5YR 3/6	WE/ST	SB/GR	ME/FI	FR	VPL/VST	Gradual
Bo4	-300	2,5YR 4/6	MO/ST	SB/GR	ME/FI	FR	VPL/VST	Diffuse
Bo5	-360	10R 4/8	MO/ST	SB/GR	ME/FI	FR	VPL/VST	Diffuse
Bo6	-455	10R 3/6	MO-ST/ST	SB/GR	ME/FI	FR	VPL/VST	Diffuse
Bo7	-555	10R 3/6	MO-ST/ST	SB/GR	ME/FI	FR	VPL/VST	Diffuse
Bo8	-630	10R 3/6	MO-ST/ST	SB/GR	ME/FI	FR	VPL/VST	Diffuse
Bo9	-705	10R 3/6	MO-ST/ST	SB/GR	ME/FI	FR	VPL/VST	Diffuse
Bo10	-795	10R 3/6	MO-ST/ST	SB/GR	ME/FI	FR	VPL/VST	Diffuse
Bo11	-950+	10R 3/6	MO-ST/ST	SB/GR	ME/FI	FR	VPL/VST	-
Profile 2 - Geric Ferralsol (Dystric, Clayic)								
Bo1	~60	2,5YR 3/6	MO/ST	SB/GR	ME/FI	FR	VPL/VST	Diffuse
Bo4	~330	10R 3/6	MO/ST	SB/GR	ME/FI	FR	VPL/VST	Diffuse
Bo5	~500	10R 3/6	MO-ST/ST	SB/GR	ME/FI	FR	VPL/VST	-
Profile 3 - Geric Ferralsol (Dystric, Clayic)								
Ap	0-20	5YR 3/4	WE	SB/GR	FI/VF-FI	VFR	SPL/SST	Clear
AB	-37	5YR 4/6	MO	SB	FI-ME	VFR	SPL/SST	Clear
BA	-58	2,5YR 4/8	WE/ST	SB/GR	ME/FI	FR	PL/ST	Diffuse
Bo1	-93	2,5YR 4/8	WE/ST	SB/GR	ME/FI	FR	PL/ST	Diffuse
Bo2	-142	2,5YR 4/8	WE/ST	SB/GR	ME/FI	FR	PL/ST	Diffuse
Bo3	-230	2,5YR 3/6	WE/ST	SB/GR	ME/FI	FR	VPL/VST	Gradual
Bo4	-345	10R 4/8	MO/ST	SB/GR	ME-CO	VFI	VPL/VST	Diffuse
Bo5	-450	10R 3/6	MO/ST	SB/GR	FI-ME	VFI	VPL/VST	Diffuse
Bo6	-575	10R 3/6	MO/ST	SB/GR	ME-CO	VFI	VPL/VST	Diffuse
Bo7	-680	10R 3/6	MO/ST	SB/GR	ME	FR	VPL/VST	Diffuse
Bo8	-755	10R 3/6	MO	SB/GR	ME	FR	VPL/VST	Diffuse
Bo9	-850	10R 3/6	MO/ST	SB/GR	ME-CO	FR	VPL/VST	Diffuse
Bo10	-980	10R 3/6	MO/ST	SB/GR	ME-CO	VFI	VPL/VST	Diffuse
Bo11	-1000+	10R 3/6	MO	SB/GR	ME	VFI	VPL/VST	-
Profile 4 - Geric Ferralsol (Dystric, Clayic)								
AB	~35	2,5YR 4/8	WE/ST	SB	FI-ME	FR	PL/ST	Clear
Bo1	~200	10R 3/6	MO/ST	SB/GR	ME/FI	VFI	VPL/VST	Diffuse
Bo3	~480	10R 3/6	MO/ST	SB/GR	ME/FI	VFI	VPL/VST	-

[1]Hz: horizon; [2]Soil color according to Munsell; [3]**Structure**: *Grade* = WE: weak, MO: moderate, ST: strong / *Type* = SB: subangular blocky, GR: granular / *Size* = VF: very thin, FI: thin, ME: medium, CO: coarse; [4]**Consistence**: *moist* = VFR: very friable, FR: friable, FI: firm, VFI: very firm / *wet (soil plasticity)* = SPL: slightly plastic, PL: plastic, VPL: very plastic; *wet (soil stickiness):* SST: slightly sticky, ST: sticky, VST: very sticky; [5]Soil classification according to IUSS Working Group WRB (2015).

Table 3. Morphological description of the soils developed in the transient landform

Hz[1]	Depth (cm)	Color[2]	Structure[3]			Consistence[4]		Boundary
			Grade	Type	Size	Moist	Wet	
Profile 5 - Geric Ferralsol (Dystric, Clayic)[5]								
Ap	0-24	5YR 3/4	WE	SB/GR	FI-ME	FI	SPL/SST	Clear
AB	-47	5YR 4/6	WE	SB	ME	FI	PL/ST	Clear
Bo1	-82	2,5YR 4/6	MO/ST	SB/GR	FI-ME/FI	FR	PL/ST	Diffuse
Bo2	-110	2,5YR 4/8	MO/ST	SB/GR	FI-ME/FI	FR	PL/ST	Diffuse
Bo3	-178	2,5YR 4/8	MO/ST	SB/GR	FI-ME/FI	FR	VPL/VST	Diffuse
Bo4	-276+	2,5YR 4/8	MO-ST/ST	SB/GR	ME/FI	FI	VPL/VST	-
Profile 6 - Geric Ferralsol (Dystric, Clayic)								
Ap	0-28	5YR 3/4	WE	GR	FI-ME	FR	PL/ST	Clear
A2	-42	5YR 3/4	MO	SB	FI-ME	FR	PL/ST	Gradual
AB	-66	5YR 4/6	WE-MO	SB	FI-ME	VFR	PL/ST	Gradual
Bo1	-113	2,5YR 4/8	WE-MO	SB	FI-ME	VFR	VPL/VST	Diffuse
Bo2	-165	2,5YR 4/8	WE-MO	SB	FI-CO	VFR	VPL/VST	Gradual
Bo3	-198	2,5YR 4/8	MO-ST	SB	FI-ME	VFR	VPL/VST	Gradual
Bo4	-247+	2,5YR 4/8	MO-ST	SB	FI-ME	VFR	VPL/VST	-
Profile 7 - Gibbsic Ferralsol (Dystric, Clayic)								
Ap	0-22	5YR 4/4	MO	G	FI-ME	FI	PL/ST	Clear
AB	-43	5YR 4/6	WE	BS	FI	FI	PL/ST	Gradual
BA	-60	5YR 4/8	MO/ST	BS/G	ME/FI	FR	PL/ST-VST	Gradual
Bo1	-112	5YR 4/6	WE/ST	BS/G	ME/FI	FR	PL/VST	Diffuse
Bo2	-140	5YR 4/6	WE/ST	BS/G	ME/FI	FR	PL/VST	Clear
BC	-270+	5YR 4/6	MO/ST	BS/G	FI-ME/FI	VFR	PL/ST	-
Profile 8 - Geric Ferralsol (Dystric, Clayic)								
Ap	0-14	7,5YR 3/4	MO	GR	VF-FI	VFR	LPL/SST	Clear
A2	-30	7,5YR 3/4	MO	SB	FI-ME	FI	VPL/VST	Clear
AB	-46	5YR 4/6	MO	SB	ME	FI	VPL/VST	Clear
BA	-67	5YR 4/6	MO/ST	SB/GR	ME/FI	FR	PL-VPL/ ST-VST	Gradual
Bo1	-112	5YR 4/6	MO/ST	SB/GR	ME/FI	FR	VPL/VST	Diffuse
Bo2	-152	5YR 4/6	MO/ST	SB/GR	ME/FI	FR	VPL/VST	Diffuse
Bw3	-185	5YR 4/6	MO/ST	SB/GR	ME/FI	FR	VPL/VST	Gradual
BC	-225+	5YR 4/6	MO/ST	SB/GR	FI-ME/FI	VFR	PL/ST	-

[1]Hz: horizon; [2]Soil color according to Munsell; [3]**Structure**: *Grade* = WE: weak, MO: moderate, ST: strong / *Type* = SB: subangular blocky, GR: granular / *Size* = VF: very thin, FI: thin, ME: medium, CO: coarse; [4]**Consistence**: *moist* = VFR: very friable, FR: friable, FI: firm, VFI: very firm / *wet (soil plasticity)* = SPL: slightly plastic, PL: plastic, VPL: very plastic; *wet (soil stickiness):* SST: slightly sticky, ST: sticky, VST: very sticky; [5]Soil classification according to IUSS Working Group WRB (2015).

The clay fraction varied from 665 to 917 g kg^{-1} and from 404 to 600 g kg^{-1} while sand fraction from 45 to 180 g kg^{-1} and from 155 to 507 g kg^{-1} in soils developed in the relict and transient landforms, respectively (Tabs. 4 and 5). There was a slight variation of particle size distribution in depth for all soil profiles, but in general the clay and sand content was relatively homogeneous. All soils are clayey or very clayey, but soils developed in the transient landform

have higher sand content than those in the relict ones, mainly P5 and P6, which sand content is even greater than its correlates belong to the same landform (i.e., P7 and P8) (Tabs. 4 and 5).

Table 4. Particle size distribution and chemical attributes of the soils developed in the relict landform

Horizon	Depth	Clay	Silt	Sand	pH	pH	ΔpH	S[1]	Al^{3+}	CEC[2]	V[3]	C[4]
	(cm)	g kg^{-1}			H_2O	KCl		$cmol_c$ kg^{-1}			%	g kg^{-1}
Profile 1 - Geric Ferralsol (Dystric, Clayic)												
Ap	0-24	752	146	102	6.12	5.39	-0.73	7.58	0.42	13.24	57.24	47.49
AB	-42	873	75	52	4.97	4.39	-0.58	0.99	0.43	7.33	13.46	19.45
BA	-63	880	70	50	5.48	4.77	-0.71	0.83	0.48	5.21	15.87	13.94
Bo1	-110	901	51	48	4.83	4.93	0.10	0.42	0.42	4.48	9.42	12.71
Bo2	-168	917	32	51	4.91	5.20	0.29	1.48	0.39	4.64	31.90	11.18
Bo3	-210	898	54	48	4.84	5.73	0.89	0.48	0.40	2.88	16.65	8.42
Bo4	-300	902	50	48	5.02	6.10	1.08	0.44	0.39	2.28	19.14	7.20
Bo5	-360	904	51	45	5.72	6.52	0.80	0.50	0.28	1.08	46.46	5.05
Bo6	-455	914	41	45	5.89	6.57	0.68	0.32	0.22	0.36	89.02	4.14
Bo7	-555	892	62	46	5.89	6.54	0.65	1.50	0.25	1.82	82.40	3.52
Bo8	-630	900	46	54	5.98	6.51	0.53	0.31	0.25	0.91	34.03	2.91
Bo9	-705	897	43	60	5.98	6.48	0.50	0.29	0.29	0.89	32.40	1.68
Bo10	-795	884	58	58	5.94	6.39	0.45	0.18	0.32	0.86	20.73	2.30
Bo11	-950+	872	68	60	5.99	6.07	0.08	0.18	0.30	1.46	12.11	1.68
Profile 2 - Geric Ferralsol (Dystric, Clayic)												
Bo1	~60	740	133	127	5.1	5.4	0.4	0.1	0.0	2.8	2.0	n.d.
Bo4	~330	809	78	113	5.7	6.4	0.7	0.0	0.0	0.3	4.6	n.d.
Bo5	~500	794	81	125	5.8	6.5	0.6	0.0	0.0	0.2	11.4	n.d.
Profile 3 - Geric Ferralsol (Dystric, Clayic)												
Ap	0-20	686	193	120	6.87	5.95	-0.92	8.08	0.41	12.46	64.85	29.26
AB	-37	866	35	98	5.73	5.15	-0.58	2.31	0.38	7.95	29.05	19.45
BA	-58	844	59	97	5.59	5.08	-0.51	0.93	0.43	6.15	15.07	15.78
Bo1	-93	848	54	97	5.92	5.50	-0.42	0.87	0.39	5.27	16.57	15.78
Bo2	-142	849	69	82	5.42	5.98	0.56	0.21	0.39	3.25	6.52	11.49
Bo3	-230	867	71	62	4.92	6.32	1.40	0.18	0.33	2.48	7.18	8.73
Bo4	-345	882	67	51	5.78	6.88	1.10	0.27	0.20	0.85	31.38	7.81
Bo5	-450	899	53	48	6.07	6.98	0.91	0.18	0.23	0.90	19.90	7.05
Bo6	-575	891	57	52	6.11	6.69	0.58	0.16	0.22	0.86	18.16	2.60
Bo7	-680	845	91	64	5.83	5.95	0.12	0.34	0.39	1.60	21.41	5.36
Bo8	-755	784	126	90	5.66	6.21	0.55	0.51	0.36	1.31	39.08	1.99
Bo9	-850	833	73	94	6.16	6.13	-0.03	0.22	0.39	1.14	19.49	1.38
Bo10	-980	815	90	95	6.31	6.04	-0.27	0.10	0.34	1.24	8.25	2.30
Bo11	-1000+	785	95	120	6.12	5.97	-0.15	0.13	0.37	1.59	8.18	1.68
Profile 4 - Geric Ferralsol (Dystric, Clayic)												
AB	~35	665	156	180	5.4	4.6	-0.9	0.1	0.1	6.2	1.9	n.d.
Bo1	~200	779	86	136	4.7	5.5	0.8	0.1	0.0	2.7	3.7	n.d.
Bo3	~480	728	156	115	5.2	6.2	1.0	0.0	0.0	0.7	3.5	n.d.

[1]S: sum of exchangeable bases; [2]CEC: cation exchange capacity at pH 7; [3]V: base saturation status; [4]C: Organic carbon content. n.d.: not determined.

Table 5. Particle size distribution and chemical attributes of the soils developed in the transient landform

Horizon	Depth	Clay	Silt	Sand	pH	pH	ΔpH	S[1]	Al^{3+}	CEC[2]	V[3]	C[4]
	(cm)	g kg^{-1}			H_2O	KCl		$cmol_c$ kg^{-1}			%	g kg^{-1}
Profile 5 - Geric Ferralsol (Dystric, Clayic)												
Ap	0-24	511	144	345	5.90	4.99	-0.91	4.68	0.50	9.62	48.64	27.11
AB	-47	531	145	324	5.99	4.87	-1.12	1.57	0.46	5.55	28.30	15.78
Bo1	-82	565	128	307	5.95	5.34	-0.61	0.80	0.44	3.36	23.83	10.88
Bo2	-110	583	113	304	5.55	5.90	0.35	0.79	0.39	2.25	35.24	7.51
Bo3	-178	582	109	309	5.65	6.19	0.54	0.46	0.33	1.48	30.97	6.89
Bo4	-276	600	89	311	5.39	6.29	0.90	0.44	0.26	1.06	41.30	3.83
Perfil 6 - Geric Ferralsol (Dystric, Clayic)												
Ap	0-28	405	89	507	6.15	5.09	-1.06	2.07	0.44	5.41	38.22	13.02
A2	-42	404	112	484	4.86	4.25	-0.61	0.43	0.47	4.47	9.71	11.18
AB	-66	460	71	469	4.86	4.28	-0.58	0.47	0.34	4.05	11.58	7.81
Bo1	-113	458	99	443	5.25	5.47	0.22	0.40	0.40	2.24	17.90	5.36
Bo2	-165	459	81	460	4.87	5.78	0.91	0.52	0.43	1.76	29.53	4.75
Bo3	-198	449	91	460	4.53	5.82	1.29	0.32	0.44	1.56	20.55	4.14
Bo4	-247	475	83	443	4.25	5.71	1.46	0.24	0.39	1.34	18.10	3.83
Profile 7 - Gibbsic Ferralsol (Dystric, Clayic)												
Ap	0-22	470	287	243	6.59	5.76	-0.83	4.27	0.40	7.45	57.32	24.05
AB	-43	491	266	243	5.16	4.47	-0.69	0.84	0.28	4.74	17.70	12.41
BA	-60	468	309	224	5.53	5.11	-0.42	1.43	0.40	4.19	34.19	9.65
Bo1	-112	518	253	229	6.82	6.32	-0.50	2.01	0.33	2.73	73.65	8.42
Bo2	-140	492	264	245	6.29	6.34	0.05	1.32	0.33	2.22	59.50	6.59
BC	-270	n.d.	n.d.	n.d.	5.06	6.04	0.98	1.11	0.36	1.91	58.21	n.d.
Profile 8 - Geric Ferralsol (Dystric, Clayic)												
Ap	0-14	585	226	189	5.7	4.8	-0.8	3.92	0.44	9.48	41.34	26.81
A2	-30	577	257	166	5.9	5.1	-0.9	3.52	0.36	7.62	46.22	20.99
AB	-46	581	270	149	5.9	5.1	-0.8	2.04	0.41	7.28	28.07	15.78
BA	-67	580	274	146	5.8	5.1	-0.7	1.51	0.40	4.63	32.59	13.02
Bo1	-112	589	267	144	5.9	5.8	-0.1	1.36	0.34	2.74	49.70	9.65
Bo2	-152	581	275	144	5.0	5.7	0.7	0.46	0.32	1.76	26.05	8.12
Bo3	-185	567	284	149	4.8	5.8	1.0	0.39	0.33	1.71	23.01	5.97
BC	-225	569	271	160	5.3	6.1	0.8	1.00	0.34	1.62	61.62	n.d.

[1]S: sum of exchangeable bases; [2]CEC: cation exchange capacity at pH 7; [3]V: base saturation status; [4]C: Organic carbon content. n.d.: not determined.

pH in water and KCl solution varied from 4.7 to 6.9 and from 4.2 to 7.0 in soils developed in the relict landform, respectively, and from 4.3 to 6.8 and from 4.3 to 6.3 in soils developed in the transient landform, respectively. The values were relatively similar between all soil profiles. However, ΔpH, which is the difference between pH in KCl and water, changed from negative to positive values in depth in all soil profiles, indicating soils behave like an anion exchanger downwards. In addition, ΔpH changed from 755 cm onwards to negative in

P3 and it was close to zero in the deepest horizon of P1, indicating an inverse change in net charge (Tabs. 4 and 5). Cation Exchange Capacity (CEC) ranged from 0.18 to 13.24 $cmol_c\ kg^{-1}$ and from 1.1 to 9.6 $cmol_c\ kg^{-1}$ in soils developed in the relict and transient landforms, respectively. The higher values of CEC were found in the upper sola and a trend to decrease in depth was observed. A similar trend was also noticed for the sum of exchangeable bases, which values predominated below 50% for all soil profiles, except in P7, which presented values above 50% from 60 cm onwards (Tabs. 4 and 5). In addition, an abrupt increase in the sum of exchangeable bases was observed between 360 and 555 cm in P1, which is associated with the highest values of pH in KCl. The organic carbon content varied from 1.4 to 47.5 $g\ kg^{-1}$ and from 3.8 to 27.1 $g\ kg^{-1}$ in soils developed in the relict and transient landforms, respectively. The highest values were observed in the most superficial horizons, with a trend to decrease in depth for all soil profiles (Tabs. 4 and 5).

4.3.2. XRD patterns and crystallographic properties of kaolinite and gibbsite

The XRD patterns of the deferrated oriented slides samples from all soil profiles are shown in Figs. 2 and 3, with assigned mineral contributions. The mineralogical composition of the clay fraction was quite similar within and between the soil profiles, indicating the presence of kaolinite, gibbsite, anatase, and rutile. However, the peak intensity was slightly different, suggesting that the soil samples do not have the same proportions of minerals. According to the XRD patterns, the peak intensity of kaolinite and gibbsite indicated a similar desilication trend in depth for all soil profiles in the relict landform. The XRD patterns showed a trend of greater amounts of gibbsite in the upper sola and a decrease in depth associated with the higher proportion of kaolinite, which can be observed more evidently in P1 and P3, which samples were collected in greater depth (Fig. 2). For all soils developed in the transient landform, the peak intensity of gibbsite was also higher than kaolinite (Fig. 3). Indeed, an inversion of the peak intensity of kaolinite and gibbsite was not observed in depth for such soils, suggesting the predominance of gibbsite in the entire profile. Furthermore, the peak intensity of gibbsite was higher and kaolinite was lower in XRD patterns of the soils developed in the transient landform than those in the relict ones, suggesting thus a higher amount of gibbsite in soils developed in the transient landform (Figs. 2 and 3).

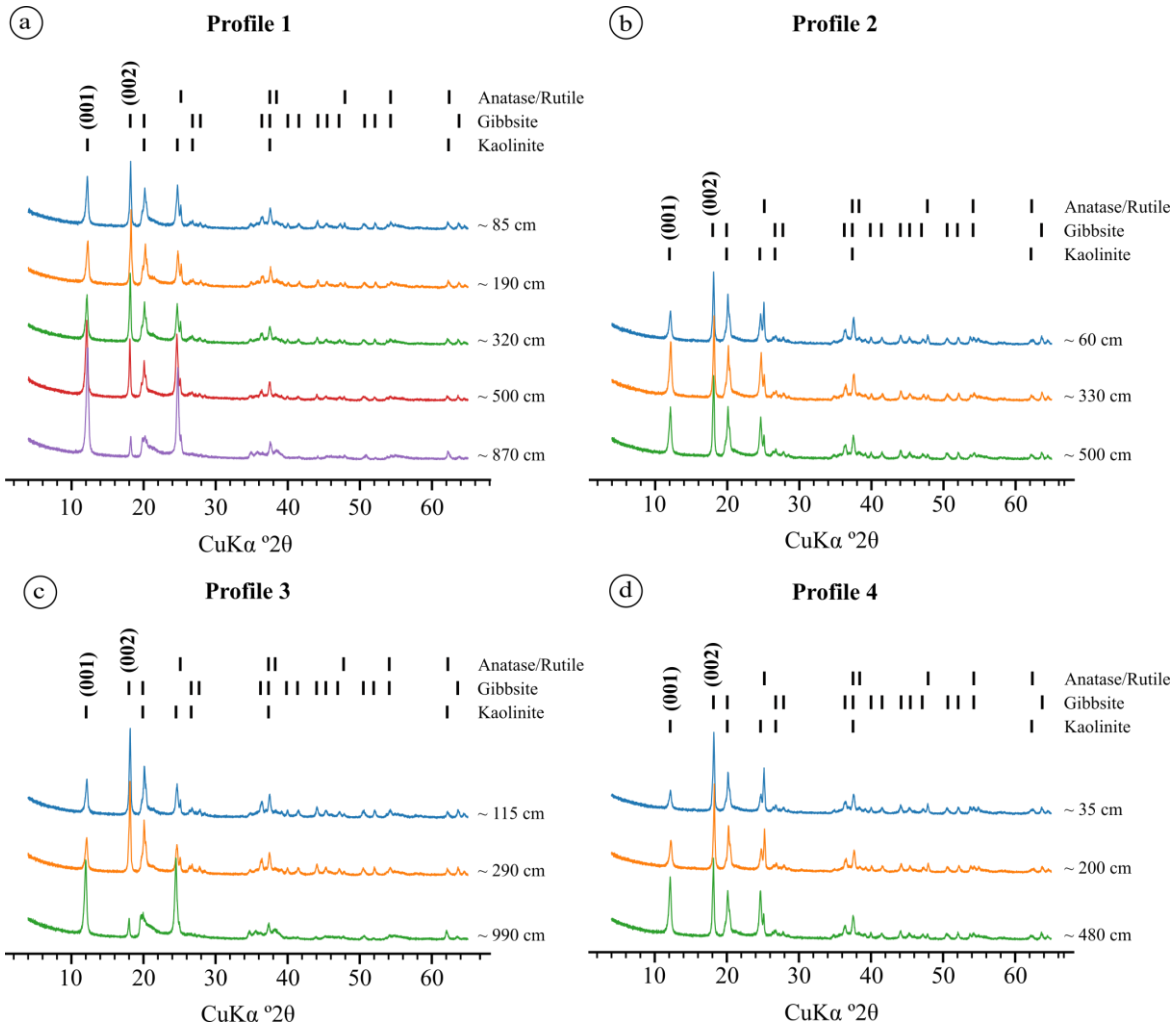

Figure 2. XRD patterns of the deferrated clay fraction samples from soils developed in the relict landform. (a) Profile 1 – P1; (b) Profile 2 – P2; (c) Profile 3 – P3; and (d) Profile 4 – P4. The d(hkl) corresponds to the d-spacing according to Bragg's Law. The location of the soil profiles is provided in Fig. 1b.

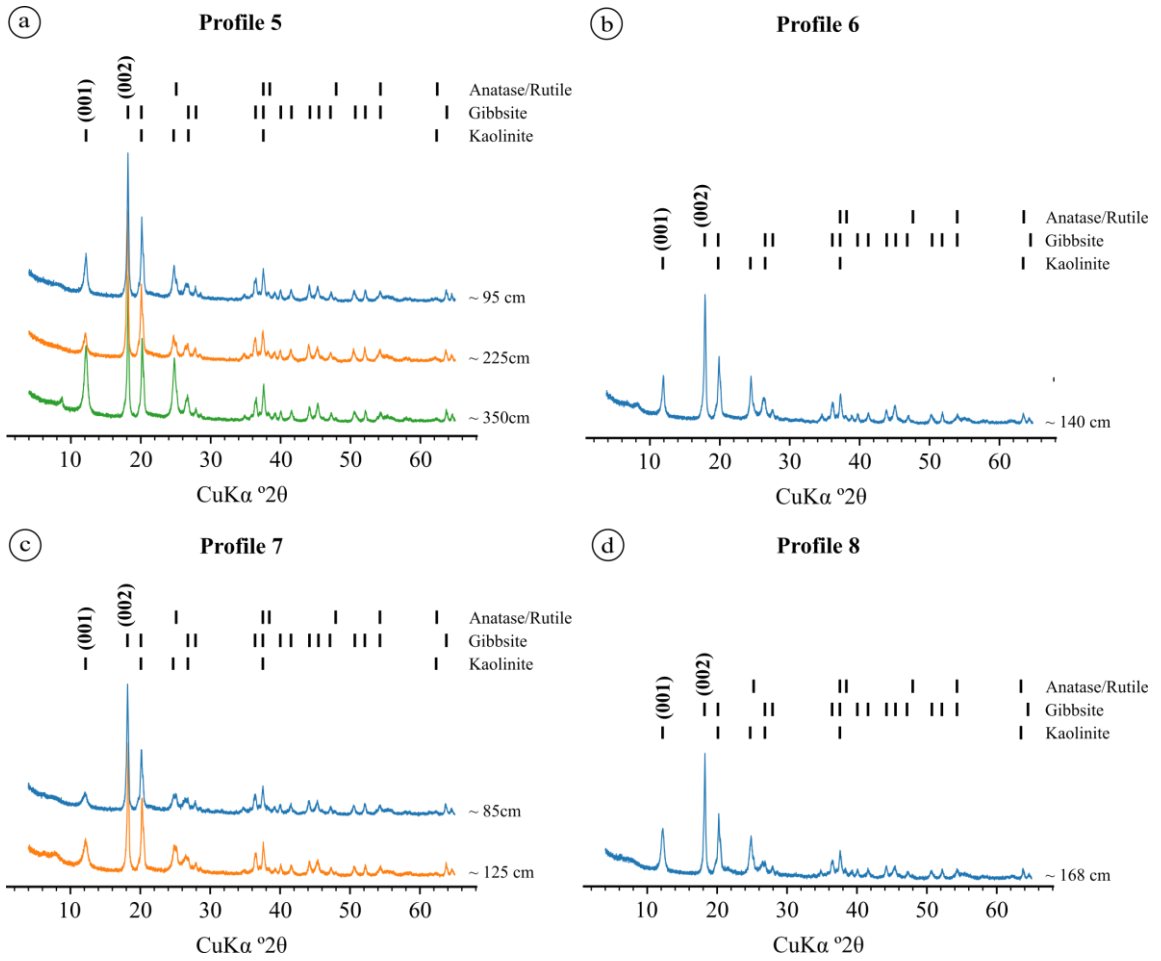

Figure 3. XRD patterns of the deferrated clay fraction samples from soils developed in the transient landform. (a) Profile 5 – P5; (b) Profile 6 – P6; (c) Profile 7 – P7; and (d) Profile 8 – P8. The d(hkl) corresponds to the d-spacing according to Bragg's Law. The location of the soil profiles is provided in Fig. 1b.

The (001) value of kaolinite ranged from 0.72 to 0.74 nm and it was slightly different between the XRD patterns of soil samples. The asymmetry index of the (001) reflection of kaolinite varied within and between soil profiles, with values ranging from 0.0 to 0.4. The highest values were observed for the most superficial as well as the deepest horizons. Therefore, a trend of variation of the asymmetry index of kaolinite was not observed (Figs. 2 and 3). The WHH values of (001) reflection of kaolinite ranged from 0.35 to 0.42 °2θ and from 0.43 to 0.81 °2θ for the XRD patterns of soils developed in the relict and transient landforms, respectively. The WHH values were similar between the soil profiles developed in the relict landform, but quite different from those soils developed in the transient landform for which broader basal reflection was observed (Tab. 6).

Table 6. Crystallographic properties of the kaolinite and gibbsite estimated from XRD patterns for the studied soil profiles

Depth (cm)	(001) kaolinite					(002) gibbsite		
	d[1]	WHH[2]	MCD[3]	ANL[4]	Asymmetry index	d	WHH	MCD
	nm	°2θ	nm			nm	°2θ	nm
Profile 1 - Geric Ferralsol (Dystric, Clayic)								
~85	0.73	0.39	20.60	28.30	0.2	0.49	0.25	32.85
~190	0.72	0.40	20.12	27.76	0.4	0.49	0.23	34.33
~320	0.73	0.39	20.68	28.30	0.1	0.49	0.24	33.31
~500	0.73	0.36	22.11	30.17	0.2	0.49	0.22	36.83
~870	0.73	0.35	22.58	31.12	0.2	0.49	0.21	38.11
Profile 2 - Geric Ferralsol (Dystric, Clayic)								
~60	0.73	0.40	20.13	27.49	0.1	0.49	0.24	34.01
~330	0.73	0.38	20.85	28.58	0.1	0.49	0.24	33.18
~500	0.73	0.39	20.28	27.70	0.0	0.49	0.25	32.85
Profile 3 - Geric Ferralsol (Dystric, Clayic)								
~115	0.73	0.40	20.19	27.64	0.3	0.49	0.24	33.30
~290	0.73	0.39	20.52	28.03	0.1	0.49	0.24	34.03
~990	0.74	0.39	20.54	27.77	0.0	0.49	0.22	36.31
Profile 4 - Geric Ferralsol (Dystric, Clayic)								
~35	0.73	0.42	18.99	26.08	0.1	0.49	0.24	33.69
~200	0.72	0.41	19.56	27.01	0.1	0.49	0.24	33.50
~480	0.73	0.39	20.72	28.36	0.3	0.49	0.25	32.73
Profile 5 - Geric Ferralsol (Dystric, Clayic)								
~95	0.73	0.54	14.90	20.41	0.2	0.49	0.25	31.58
~225	0.73	0.57	14.00	19.07	0.2	0.49	0.26	31.51
~350	0.73	0.58	13.73	18.85	0.1	0.49	0.26	30.90
Profile 6 - Geric Ferralsol (Dystric, Clayic)								
~140	0.73	0.43	18.55	25.40	0.2	0.49	0.28	28.99
Profile 7 - Gibbsic Ferralsol (Dystric, Clayic)								
~85	0.73	0.81	9.84	13.42	0.0	0.49	0.27	29.82
~125	0.73	0.79	10.15	13.95	0.1	0.49	0.28	28.89
Profile 8 - Geric Ferralsol (Dystric, Clayic)								
~168	0.73	0.55	14.63	20.18	0.0	0.49	0.28	28.95

[1] d: d-spacing according to Bragg's Law; [2] WHH: Width at Half Height; [3] MCD: Mean Coherent Domain; [4] ANL: Average Number of Layers.

The WHH is inversely related to the sizes of coherently diffracting regions and thus lower values suggest larger MCD sizes, according to Scherrer's formula (Klug and Alexander, 1954). The MCD sizes considering the (001) reflection of kaolinite ranged from 18.99 to 22.58 nm and from 9.84 to 18.55 nm in soils developed in the relict and transient landforms, respectively. The largest MCD sizes of kaolinite were observed in the deepest horizon of P1 (~870 cm), while the smallest one was observed in the most superficial horizon of P5 (~85 cm),

which value was less than half of that observed in the deepest horizon of P1. The MCD sizes of kaolinite tended to increase or be similar in depth in soils developed in the relict landform and decrease in those developed in the transient ones, at least in P5 and P7 (Tab. 6). The ANL of kaolinite in soils developed in the relict landform was between 26.08 and 31.12 while those in the transient landform ranged from 13.42 to 25.40, indicating kaolinite with higher ANL in soils developed in the relict than transient landforms. The values of ANL tended to increase in depth in P1 and P4, similar to the MCD sizes, while similar values between soil horizons were observed in P2 and P3. The lowest ANL values of kaolinite were observed in P5, which are lower than those of soils belonging to the same landform and quite lower than those in the relict landform (Tab. 6).

The (002) values of gibbsite were 0.49 nm for XRD patterns of all soil samples. The WHH values ranged from 0.21 to 0.25 °2θ and from 0.25 to 0.28 °2θ for XRD patterns of soils developed in the relict and transient landforms, respectively. Therefore, the WHH values were slightly higher for the XRD patterns of soils developed in the transient than relict landforms. The MCD sizes ranged from 32.73 to 38.11 nm and from 28.89 to 31.58 nm in soils developed in the relict and transient landforms, respectively (Tab. 6). The MCD sizes of gibbsite were larger in soils developed in the relict landform and showed an increase in depth in P1 and P3, but an opposite trend was observed in P2 and P4. Instead, for the soils in the transient landform, the MCD sizes of gibbsite were relatively lower and decreased slightly in depth (Tab. 6).

4.3.3. Dehydroxylation temperature and amounts of kaolinite and gibbsite

The dehydroxylation temperature (DT) of kaolinite ranged from 480.2 to 494.1ºC and from 474.8 to 485.0ºC in soils developed in the relict and transient landforms, respectively (Tab. 7). There was a trend to increase the DT value of kaolinite in depth in all soil profiles developed in the relict landform, with higher values for samples collected in greater depth (~870 cm in P1 and ~990 cm in P7). No trend of DT values of kaolinite was observed for soils in the transient landform, as for some of them the DT value increased and for others, it decreased in depth. The lowest DT values of kaolinite were observed in P7 followed P8, values that were even lower than their counterparts which belong to the same landform (i.e., P5 and P6) (Tab. 7).

Table 7. Dehydroxylation temperature and estimation of the amounts of kaolinite and gibbsite by thermogravimetric and differential thermal analysis for the studied soil profiles

	Kaolinite		Gibbsite		
Depth (cm)	Dehydroxylation temperature ºC	Amounts %	Dehydroxylation temperature ºC	Amounts %	Kt/(Kt+Gb)
Profile 1 - Geric Ferralsol (Dystric, Clayic)					
~85	485.4	56.6	267.0	32.9	0.63
~190	482.4	52.0	265.4	32.7	0.61
~320	483.4	42.9	264.8	31.1	0.58
~500	485.4	52.1	265.9	29.2	0.64
~870	490.8	72.9	257.0	9.7	0.88
Profile 2 - Geric Ferralsol (Dystric, Clayic)					
~60	481.7	38.4	269.4	37.2	0.51
~330	482.4	45.1	266.4	36.0	0.56
~500	483.4	38.6	266.8	35.1	0.52
Profile 3 - Geric Ferralsol (Dystric, Clayic)					
~115	482.9	42.5	268.4	37.2	0.53
~290	484.2	44.0	268.6	38.1	0.54
~990	494.1	71.9	257.5	9.4	0.88
Profile 4 - Geric Ferralsol (Dystric, Clayic)					
~35	480.8	37.8	267.9	35.4	0.52
~200	480.2	36.6	268.7	37.2	0.50
~480	483.1	37.6	267.2	33.3	0.53
Profile 5 - Geric Ferralsol (Dystric, Clayic)					
~95	481.4	32.5	270.7	38.1	0.46
~225	483.8	38.0	272.3	42.6	0.47
~350	482.3	38.9	270.4	40.1	0.49
Profile 6 - Geric Ferralsol (Dystric, Clayic)					
~140	484.1	36.1	270.9	38.4	0.48
~180	485.0	30.9	271.3	39.4	0.44
Profile 7 – Gibbsic Ferralsol (Dystric, Clayic)					
~85	479.4	43.3	271.4	39.5	0.52
~125	474.8	39.7	269.5	39.4	0.50
Profile 8 - Geric Ferralsol (Dystric, Clayic)					
~168	480.6	31.7	269.8	35.7	0.47

The DT value of gibbsite ranged from 257.0 to 269.4ºC and from 269.5 to 272.3ºC in soils developed in the relict and transient landforms, respectively (Tab. 7). In general, there was a downward decrease in the DT value of gibbsite in soils developed in the relict landform, a trend that was inverse to that observed for kaolinite. The lowest DT values of gibbsite were found for samples collected in greater depth (i.e., ~870 cm in P1 and ~990 cm in P7). The DT

value of gibbsite in soils developed in the transient landform was higher than that observed in soils developed in the relict landform. However, no trend of DT values was observed in depth, thus being similar to that observed for kaolinite (Tab. 7).

The amounts of kaolinite varied from 36.6 to 72.9% and from 30.9 to 43.3% in soils developed in the relict and transient landforms, respectively. While gibbsite varied from 9.4 to 38.1% and from 35.7 to 42.6% in soils in the relict and transient landforms, respectively (Tab. 7). The higher amounts of kaolinite were observed in P1 and the lowest ones in P8. There was a trend to increase in depth the amounts of kaolinite in P3. However, the same trend was not observed in the other soil profiles developed in the relict landform, because, for instance, a decrease follows by an increase in the amounts of kaolinite in depth was observed in P1. An opposite trend was observed in P2, where an increase followed by a decrease in the amount of kaolinite was observed. In addition, the amounts of kaolinite were similar between the soil horizons of P4, while, although the slight differences, the amounts of gibbsite tended to decrease in depth in soils developed in the relict landform (Tab. 7). The amounts of kaolinite in depth were similar to P1 and P3, with more than 70% in the deepest horizons (~870 cm in P1 and ~990 cm in P3) and values close or below 50% in the upper horizons. Lower amounts of kaolinite in P2 and P4 were observed, with values of ~40% in all soil horizons. A lower amount of gibbsite was observed in the deepest horizons of P1 and P3, with values lower than 10%. Instead, similar amounts were observed in the other horizons of soils developed in the relict landform, with values close to 35% (Tab. 7).

A variation of the amounts of kaolinite and gibbsite was observed in depth in soils developed in the transient landform. There was a decrease in the amounts of kaolinite accompanied by a slight increase in depth in the amounts of gibbsite in P6 and P7. Instead, in P5, there was an increase of kaolinite in depth while a decrease and then an increase of the amounts of gibbsite in depth were observed. Although such differences, the amounts of kaolinite and gibbsite were quite similar between the soil horizons and profiles, with values nearly 35% for both clay minerals, similar to those observed in the upper sola of soil profiles developed in the relict landform. No predominance of one over the other was observed in soils developed in the transient landform (except in P7), as observed for the soils in the relict landform (Tab. 7).

4.3.4. XRD patterns of the iron concentration samples and crystallographic properties of goethite and hematite

The XRD patterns indicated that goethite, hematite, and anatase are present in the clay fraction of all soils, and zircon is present only in soils developed in the transient landform. Similar to that observed for the XRD patterns of the deferrated samples, the peak intensity is slightly different between the soil horizons and thus different proportions of minerals may exist in depth. Indeed, the peak intensity was higher for goethite than hematite in the upper sola for all soil profiles developed in the relict landform. However, a decrease of the peak intensity of goethite was noticed in depth, which can be observed more clearly in ~870 cm in P1 and ~990 cm in P7, suggesting a downward increase of amounts of hematite in P1, P2, and P4, and a predominance of hematite over goethite in the deepest horizon of P3. In addition, the peak intensity of hematite was very low for soil samples from the transient landform, and thus the peaks of goethite were predominant, except for P5, which the peak intensity of both minerals was roughly similar (Figs. 4 and 5).

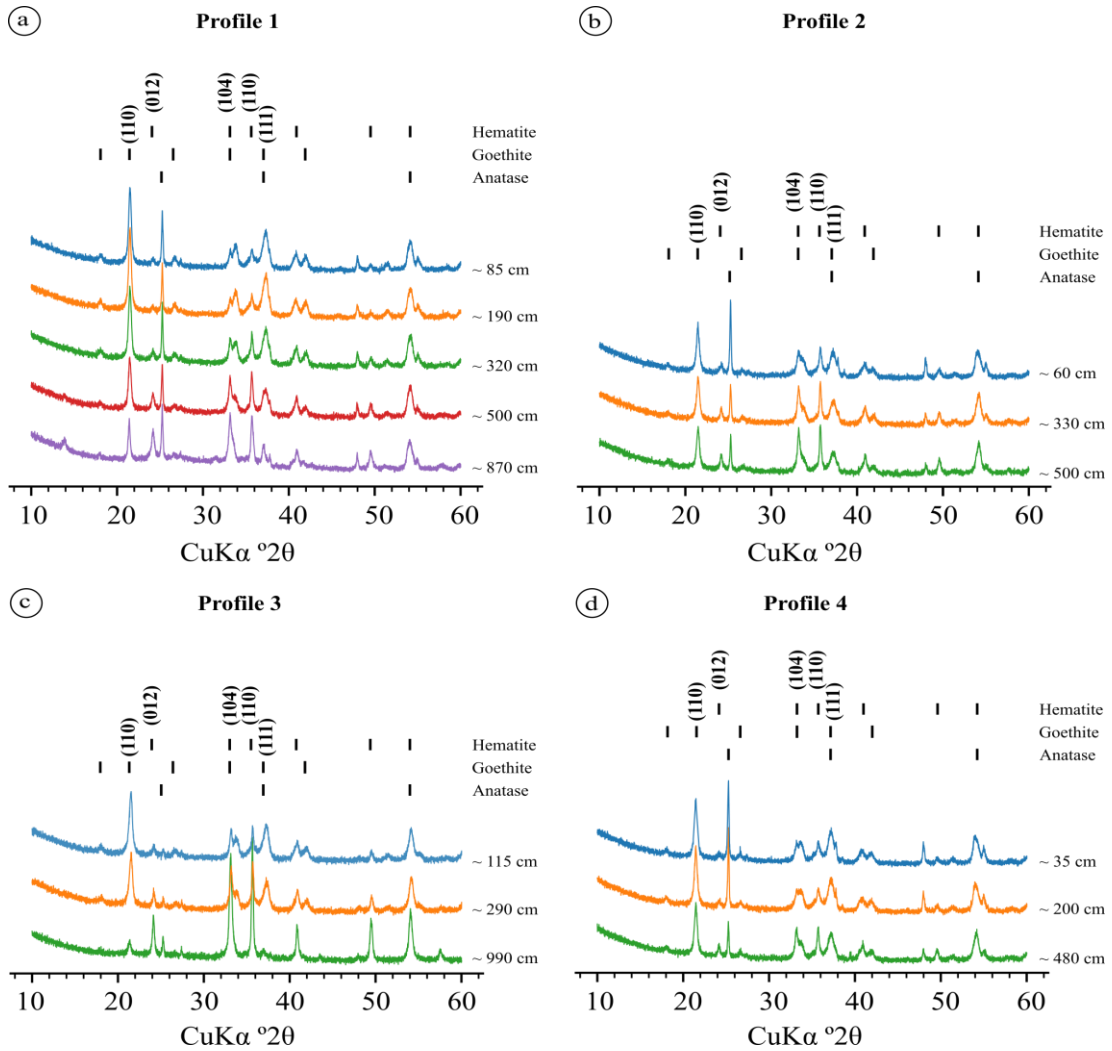

Figure 4. XRD patterns of the iron concentration samples from soils in the relict landform. (a) Profile 1 – P1; (b) Profile 2 – P2; (c) Profile 3 – P3; and (d) Profile 4 – P4. The d(hkl) corresponds to the d-spacing according to Bragg's Law. The location of the soil profiles is provided in Fig. 1b.

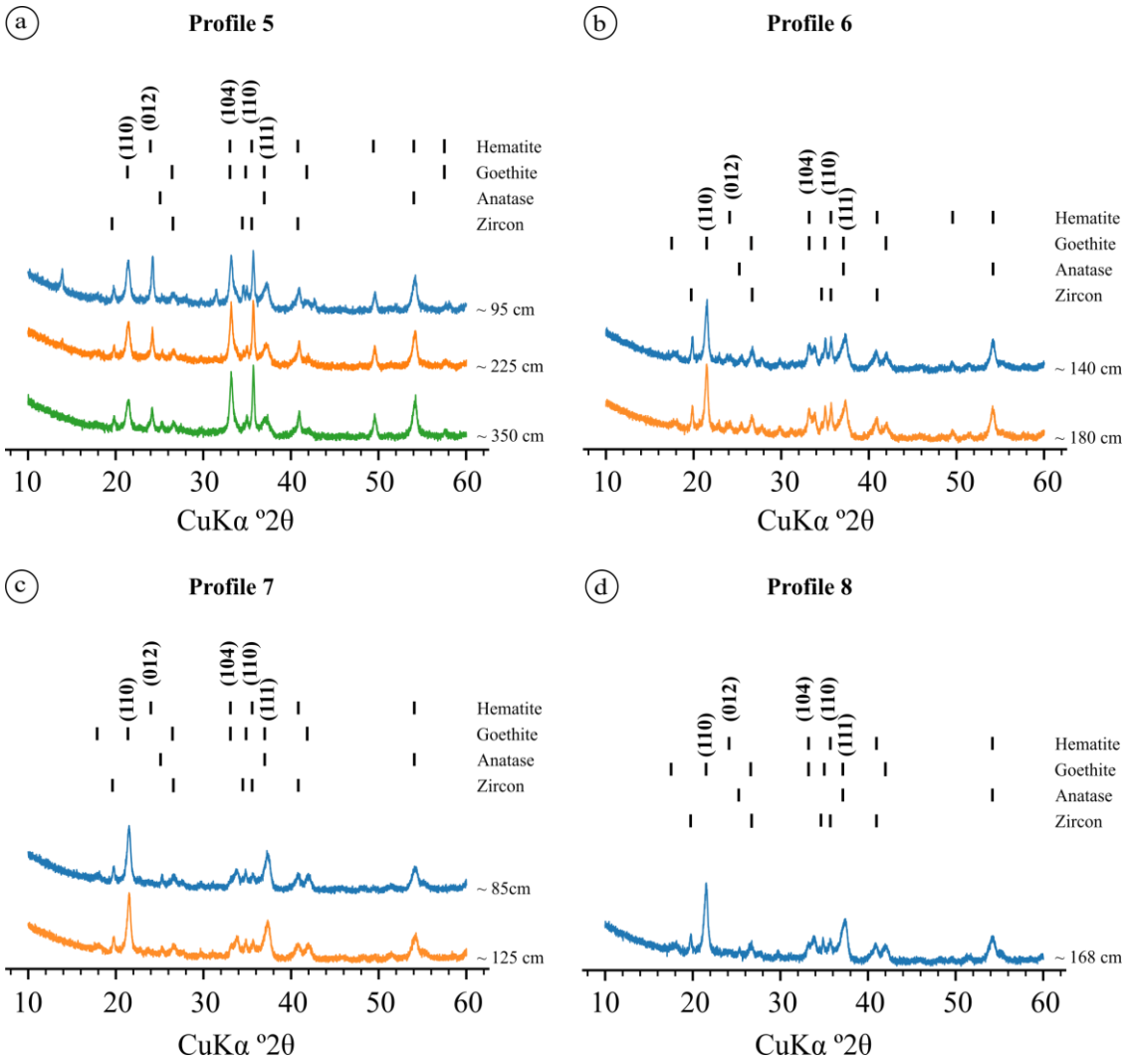

Figure 5. XRD patterns of the deferrated clay fraction samples from soils developed in the transient landform. (a) Profile 5 – P5; (b) Profile 6 – P6; (c) Profile 7 – P7; and (d) Profile 8 – P8. The d(hkl) corresponds to the d-spacing according to Bragg's Law. The location of the soil profiles is provided in Fig. 1b.

The (110) value of goethite ranged from 0.41 to 0.42 nm between the XRD patterns of soil samples, with the higher value for the sample from the deepest horizon of P1. A variation of the (104) peak of hematite was not observed, which was 0.27 nm for all XRD patterns (Tab. 8). The WHH values of (110) reflection of goethite ranged from 0.30 to 0.47 °2θ and from 0.41 to 0.52 °2θ for the XRD patterns of soils developed in the relict and transient landforms, respectively. There was a sharp variation of the WHH values between soil horizons and also between soil profiles in both landforms. The lower WHH values were observed for XDR patterns of soil samples from the relict than transient landforms, except for P6, which values were similar to those observed for thicker soils (Tab. 8). The MCD sizes considering the (110) reflection of goethite ranged from 17.05 to 27.21 nm and from 15.68 to 19.51 nm in soils

developed in the relict and transient landforms, respectively. The largest MCD sizes of goethite were observed in P1, mainly in the deepest horizon (~870 cm), while the smallest MCD sizes were observed in the upper sola of P5. The MCD sizes of goethite tended to increase in depth in the thickest soils developed in the relict landform (i.e., P1 and P3), suggesting an upward replacement of goethite with larger to smaller MCD sizes. Instead, similar values of the MCD sizes of goethite were observed between the soil horizons of the other soil profiles (Tab. 8). The WHH values of (104) hematite ranged from 0.27 to 0.57 °2θ and from 0.42 to 0.71 °2θ for XRD patterns of soils developed in the relict and transient landforms, respectively. The MCD sizes of hematite ranged from 13.81 to 31.02 nm and from 11.63 to 19.53 nm in soils developed in the relict and transient landforms, respectively (Tab. 8). The MCD sizes of hematite were larger in soils developed in the relict landform and showed a downward decrease in P1 and P3, but an opposite trend was observed in P2 and P4. The smallest MCD sizes of hematite were observed in the deepest horizon of P1 and the largest one in the deepest horizon of P4. For the soils developed in the transient landform, the MCD sizes of hematite were relatively smaller and, in general, slightly increased in depth (Tab. 8).

Table 8. Crystallographic properties of the goethite and hematite estimated from XRD patterns for the studied soil profiles

Depth (cm)	(110) goethite			(104) hematite			Al-substitution		Gt/ (Gt+Hm)	Fe_2O_3
	d[1]	WHH[2]	MCD[3]	d	WHH	MCD	Gt[4]	Hm[5]		
	nm	°2θ	nm	nm	°2θ	nm	mol %			%
Profile 1 - Geric Ferralsol (Dystric, Clayic)										
~85	0.41	0.38	21.09	0.27	0.40	20.77	33.3	6.4	0.94	4.7
~190	0.41	0.40	20.42	0.27	0.41	20.11	32.6	6.3	0.98	5.3
~320	0.41	0.40	20.47	0.27	0.40	20.96	33.6	7.1	0.85	4.8
~500	0.41	0.40	20.46	0.27	0.43	19.45	33.1	6.0	0.63	5.1
~870	0.42	0.30	27.21	0.27	0.57	14.62	21.3	8.4	0.23	5.2
Profile 2 - Geric Ferralsol (Dystric, Clayic)										
~60	0.41	0.44	18.39	0.27	0.36	23.19	28.3	7.7	0.91	8.2
~330	0.41	0.44	18.32	0.27	0.28	30.14	31.6	8.0	0.91	7.6
~500	0.41	0.43	18.61	0.27	0.28	30.10	30.8	8.2	0.85	8.8
Profile 3 - Geric Ferralsol (Dystric, Clayic)										
~115	0.41	0.47	17.05	0.27	0.29	28.87	30.7	4.6	1.00	7.7
~290	0.41	0.47	17.19	0.27	0.58	14.41	32.7	6.3	0.70	7.7
~990	0.42	0.41	19.79	0.27	0.4	20.85	17.3	2.6	0.03	7.8
Profile 4 - Geric Ferralsol (Dystric, Clayic)										
~35	0.41	0.45	18.14	0.27	0.49	17.02	28.2	9.8	0.80	7.6
~200	0.41	0.45	18.15	0.27	0.60	13.81	28.9	9.5	0.67	6.2
~480	0.41	0.43	18.74	0.27	0.27	31.02	30.6	7.4	1.00	8.0
Profile 5 - Geric Ferralsol (Dystric, Clayic)										
~95	0.41	0.51	15.80	0.27	0.42	19.53	30.3	8.1	0.60	8.3
~225	0.41	0.52	15.68	0.27	0.46	18.09	30.4	8.1	0.50	10.5
~350	0.41	0.52	15.71	0.27	0.45	18.43	29.9	8.4	0.44	11.8
Profile 6 - Geric Ferralsol (Dystric, Clayic)										
~140	0.41	0.43	19.03	0.27	0.52	16.05	31.7	6.5	0.70	8.1
~180	0.41	0.41	19.51	0.27	0.48	17.40	31.9	6.7	0.70	9.1
Profile 7 - Gibbisic Ferralsol (Dystric, Clayic)										
~85	0.41	0.50	16.10	0.27	0.71	11.63	33.6	2.4	0.77	6.5
~125	0.41	0.50	16.15	0.27	0.56	14.84	33.2	3.1	0.89	7.4
Profile 8 - Geric Ferralsol (Dystric, Clayic)										
~168	0.41	0.51	15.89	0.27	0.46	17.88	33.3	5.5	0.97	8.0

[1] d: d-spacing according to Bragg's Law; [2] WHH: Width at Half Height; [3] MCD: Mean Coherent Domain; [4] Gt: Goethite; [5] Hm: Hematite.

Al-substitution varied from 17.3 to 33.6% and from 29.9 to 33.6% in goethite, and from 2.6 to 9.8%, and from 2.4 to 8.4% in hematite of soils developed in the relict and transient landforms, respectively. The largest Al-substitution in goethite was frequently observed in the upper sola, except in P2 and P4, which an inverse trend was observed. The lowest values were observed in the deepest soil horizons of P1 and P3, which values were lower than 22%. There was a sharp variation of Al-substitution in hematite, but no clear trend was observed in the soil

profiles. There was an upward decrease in P1 and P2 and an upward increase in P4, which belongs to the same landform, although different slope positions (Tab. 8).

According to Gt/(Gt+Hm) ratio calculated from XRD patterns, there is a predominance of goethite in all soil profiles, except in the deepest horizon of the thickest soil profiles (i.e., P1 and P3). Gt/(Gt+Hm) ratio suggests that the deepest horizons of P1 have ~23% of goethite while the deepest one of P3 has less than 1% of goethite (Tab. 8). Nevertheless, peaks with very low intensity corresponding to hematite were observed in the XRD pattern of P3 (Fig. 4). Different from its correlates, XRD patterns of P5 showed an increase in the proportion of hematite in depth, but even so, a predominance of goethite was still observed (Tab. 8).

4.4. Discussion

The soils developed in the relict landform (i.e., P1, P2, P3, and P4) are much deeper (at least twice) than those in the transient ones (i.e., P5, P6, P7, and P8). It was not observed the contact with the underlying material in P1 and P3 (A + B horizons >15 m), but P2 and P4 are underlying ferruginous duricrusts. The soils developed in the transient landform in contrast are shallower (<5 m) and no evidence of lithological discontinuity was observed, suggesting that they are developed from the underlying bedrock. The relative homogeneity of the particle size distribution observed in depth for all soil profiles is associated with the strong degree of weathering and synergic action of fauna in the soil homogenization (bioturbation), as also were reported for other Ferralsols worldwide (e.g., Chauvel et al., 1983; Macedo and Bryant, 1987; Lepsch and Buol, 1988; Muggler et al., 2007; Ferreira et al., 2011; Jouquet et al., 2015; Freitas et al., 2021). Although soils are developed in different landforms with contrasting age range and parent materials, the chemical attributes of all soil profiles indicate that they are highly weathered, which is evidenced by the silt/clay ratio <0.6, presence of low-activity clays, low base saturation status, the sum of exchangeable bases plus Al^{3+} of less than 1.5 $cmol_c\ kg^{-1}$ clay, and net positive charge in most sub-horizons B (Tabs. 4 and 5), confirming the geric properties (IUSS Working Group WRB, 2015). However, the geric properties were not observed in P7, due to the predominant net charge close to zero or negative, and a higher sum of exchangeable bases plus Al^{3+} (Tab. 4).

The mineralogy of the clay fraction of all soil profiles is dominated by kaolinite, gibbsite, hematite, goethite, anatase/rutile, and accessory minerals (i.e., zircon in the soils developed in the transient landform) (Figs. 2, 3, 4 and 5), similar to that observed in others Ferralsols developed over different parent materials, climates, and landscape positions in the

intertropical zone (e.g., Curi and Franzmeier, 1984; Vidal-Torrado et al., 1999; Fritsch et al., 2005; Muggler et al., 2007; Mathian et al., 2020). The variation of the basal spacing and broadening of the (001) reflection of kaolinite is not related to the interstratification with 2:1 clay mineral, considering that the Asymmetry Index (AI) of this plan was low (Tab. 6). Therefore, it may be related to different crystal size, degree of stacking disorder, or isomorphic substitution of Al^{3+} by Fe^{3+} in octahedral sheet, which induces a decrease in the interplanar spacing due to reduced mineral ordering, as frequently reported for kaolinites from different zones of highly weathering profiles (e.g., Janot and Gilbert, 1973; Herbillon et al., 1976; Didier et al., 1983; Tardy and Nahon, 1985; Singh and Gilkes, 1992; Balan et al., 2005; Fritsch et al., 2011).

It is frequently reported that soils with a predominance of gibbsite instead of kaolinite are found mostly in Brazilian ancient landscapes under tropical climate conditions (e.g., Curi and Franzmeier, 1984; Motta et al., 2002; Gomes et al., 2004; Reatto et al., 2008; Rolim Neto et al., 2009; Freitas et al., 2021). According to the XRD patterns of the soil samples from the relict landform, the mineralogy of clay fraction is predominated by gibbsite instead of kaolinite in the upper sola. However, an inversion in the peak intensity was observed in depth, indicating the predominance of kaolinite downwards, which was more evident in P1 and P7, which soil samples were collected in greater depth (Fig. 2). According to the TG-TDA (Tab. 7), the amounts of kaolinite increase from the top to the bottom accompanied by a decrease in the amounts of gibbsite in soils developed in the relict landform. However, the amounts of gibbsite do not exceed the amounts of kaolinite as suggested by the XRD patterns (Fig. 2) and proposed by several studies carried out in soils developed at the Brazilian Central Plateau (Motta et al., 2002; Gomes et al., 2004; Reatto et al., 2008; Rolim Neto et al., 2009). The estimation of the relative amounts of minerals in clay fraction via XRD patterns can be misleading, because many factors in addition to the amounts of minerals may affect the intensity of the diffraction peaks, such as crystallite size, degree of structural order, preferred orientation, etc (Klug and Alexander, 1954; Brown and Brindley, 1980; Dixon and Weeds, 1989). Moreover, as many studies have been carried out in the first two meters of soils, the variation of amounts of kaolinite and gibbsite is not frequently reported for Ferralsols developed in the Brazilian Central Plateau, except for a few studies as Macedo and Bryant (1987). Therefore, the generalization that Ferralsols developed in Brazilian ancient landscapes correspond to soils with a predominance of gibbsite must be reconsidered. In addition, further investigation using more appropriate techniques and deeper sampling are needful, because many of them are still prevail in the upper sola (up to 200 cm) (e.g., Gomes et al., 2004; Reatto et al., 2008; Rolim Neto et al., 2009).

The peak intensity of gibbsite from the XRD patterns is much more intense than the peak of kaolinite in all soils developed in the transient landform (Fig. 3). However, the amounts of both minerals were roughly similar according to the TG-TDA (Tab. 7). It was expected to observe a difference in the proportion of kaolinite and gibbsite, because the relict landform is much older and has thicker soils than the transient ones (Marques et al., 2021). Indeed, the soils developed in the relict landform have fewer amounts of gibbsite than those in the transient landform (Tab. 7). Differences in peak intensity of kaolinite and gibbsite from XRD patterns were observed by Reatto et al. (2008) for selected samples of Ferralsols belonging to the same landform (<1,000 elevation) reported here as transient landform, but at different elevations and hillslope positions. The XRD patterns of the samples analysed by those authors indicated a higher intensity of kaolinite peaks for soils developed in higher and flat positions (~920 m elevation and <1% slope gradient) and gibbsite for lower and backslope position (~760 m elevation and 7% slope gradient). The authors justified these variations by the local topographic location, which would influence the volume of water percolating in soils. However, greater water percolation and consequently higher losses of Si are commonly reported to occur on soils developed in the flatter positions of the landscape, rather than those developed in more steep positions. Therefore, a greater occurrence of gibbsite is expected under free drainage conditions, lower Si activity, and even pedoenvironment with Al-rich solutions whereas high amounts of kaolinite tend to occur in a less strongly leaching environment (e.g., Didier et al., 1985; Trolard and Tardy, 1987).

The MCD sizes of kaolinite have been reported to range from 11 to 51 nm and 9 to 26 nm in highly weathered soils developed in Australia and Brazil, respectively (Singh and Gilkes, 1992; Melo et al., 2001). Similar results of the MCD sizes of kaolinite were found in our study in soils developed in both landforms, with smaller MCD sizes of kaolinite in soils developed in the transient landform (ranging from 9.84 to 18.55 nm) and larger size (ranging from 18.99 to 22.58 nm) in soils in the relict landform, with an overall trend to increase in depth (Tab. 6). The MCD sizes of gibbsite were also larger in soils developed in the relict landform and smaller in those in the transient landform, suggesting that kaolinite and gibbsite with large MCD sizes coexist in the soil horizons of Ferralsols (Tab. 6). However, the amounts and the DT value of gibbsite in the deepest horizon of the thickest soil profiles (i.e., P1 and P3) were very low (i.e., <10% of gibbsite and DT <260 ºC) (Tab. 7), and thus lead us to question whether the result could be misleading due to the limitations of the XRD patterns.

Several authors have observed that the DT of kaolinite depends strongly on its degree of ordering. Standard kaolinites were reported to show a strong endothermic deflection in the

DTA curves at ~530-540°C for the well-ordered specimen (Smykatz-Kloss, 1974; Queiroz de Carvalho, 1983; Singh and Gilkes, 1992) and at <515°C for poorly ordered ones (Queiroz de Carvalho, 1983; Karathanasis, 2008). Singh and Gilkes (1992) reported DT of kaolinite of highly weathered soils from Australia (amounts of kaolinite ~940 g kg-1 clay) ranging from 464 to 520°C, with most values less than 500°C. Queiroz de Carvalho (1983) obtained DT of kaolinite from ferralitic soils ranging from 470 to 550°C whereas Melo et al. (2001) found values from 497 to 518°C, with predominant values above 500°C, for Brazilian kaolinite-rich soils (i.e., containing more than 50% of kaolinite in the clay fraction).

According to our results, it was possible to observe that with decreasing of WHH from XRD patterns for (001) reflection of kaolinite, respectively with increasing of the MCD sizes, the DT also increase (Tabs. 6 and 7). This shows that kaolinites with larger MCD sizes must have lesser amounts of structural disorder, as also observed by Melo et al. (2001) and Balan et al. (2005) for highly weathered soils in Brazil. It is worthy to note that the DT values obtained for the samples analysed in our study were lower than those reported for standard kaolinites and even for those from highly weathered soils in Brazil (Queiroz de Carvalho, 1983; Melo et al., 2001). The variation of the DT of kaolinite, accompanied by the variation in the MCD sizes (Tabs. 6 and 7), observed in depth in soils developed in the relict landform must be related to distinct populations of kaolinites, although we do not have data to support it. According to the MCD sizes and DT values (Tabs. 6 and 7), the replacement of well-ordered kaolinites associated with less aluminous goethites by disordered ones in soils developed in the relict landform can be related to a past weathering condition, as observed for other Ferralsols in the intertropical zone (e.g., Fritsch et al., 2005; Balan et al., 2007; Muggler et al., 2007; Allard et al., 2020; Mathian et al., 2020).

The subsequent upwards dissolution of kaolinites associated with the crystallization of gibbsites and the formation of Al-rich goethites in soils developed in the relict landform can represent the present-day weathering condition (e.g., Vernet et al., 1994; Ledru et al., 1996; Pessenda et al., 1996; Oliveira et al., 2020), suggesting greater water activity and lower Si activity in the upper sola. Indeed, the upwards changes in Gt/(Gt+Hm) ratio and increase of Al-substitution (Tab. 8) can be interpreted as resulting from the yellowing or xanthization process, as already reported for other Ferralsols under humid and semi-humid tropical climate conditions (Fritsch et al., 2005; Mathian et al., 2020; Melo et al., 2020). Although no geochronological data are available to unveil the weathering periods related to the formation and transformation of such minerals, several studies have reported a similar trend for Ferralsols developed in the intertropical zone (e.g., Didier et al., 1985; Ambrosi et al., 1986; Trolard and Tardy, 1989;

Bilong et al., 1992; Nahon and Tardy, 1992; Balan et al., 2005; Muggler et al., 2007). In addition, Balan et al. (2005) pointed out that the persistence of well-ordered kaolinite in Ferralsols from the Amazon region unraveled by kaolinite dating (Allard et al., 2020; Mathian et al., 2020) may be related to its relatively slow rate of transformation, confronting the dynamical equilibrium model of kaolinite. Nevertheless, the exposure time of the surface at the Brazilian Central Plateau is expected to be older than that at the Amazon basin and therefore the persistence of kaolinite in such soils should be investigated in more detail and contrasted with studies from other intertropical regions.

According to the MCD sizes and DT values, kaolinites with a higher structural disorder or small crystal size were observed in soils developed in the transient landform, mainly in P5 (Tabs. 6 and 7). Although the peak intensity of the XRD patterns suggested that gibbsite predominates in the clay fraction of soils in the transient landform (Fig. 3), TG-DTA showed a similar proportion of both clay minerals. This may have occurred because crystals of smaller size or poorly ordered influenced the XRD patterns, since it was not observed in the XRD patterns of samples from the deepest horizons of P1 and P3, which kaolinites with larger MCD sizes and lower structural disorder was observed (Tabs. 6 and 7).

4.5. Conclusion

Ferralsols developed in distinct landforms and parent materials in an ancient landscape of the Brazilian territory have contrasting thickness. The soils developed in the relict and older landform are much thicker (>15 m) than those in the transient and younger ones (<5 m). Nevertheless, soils in both landforms are highly weathered and have chemical attributes corresponding to the geric properties in most sub-horizons B. The geric properties are frequently related to soils predominating gibbsite and iron oxides/oxyhydroxides, but our results support the occurrence of geric properties even in soil horizons with 29% of gibbsite, 52% of kaolinite and 5% of iron oxides, in an intense but not total ferralitization stage. Soils developed in the transient landform have relatively similar amounts of kaolinite and gibbsite in depth, which amounts of gibbsite were roughly higher than those in soils developed in the relict landform. Highly disordered kaolinites and with small MCD sizes, and gibbsites more crystalline were observed in soils developed in the transient landform, implying no clear trend with the exposure time of the surface. In contrast, an upward replacement of kaolinites with large MCD sizes and well-ordered associated with less aluminous goethite by kaolinites with smaller MCD sizes and disordered was observed in the thicker soil profiles developed in the

relict landform. In addition, such replacement also accompanied an increase in the amounts of gibbsite with small MCD sizes and the formation of Al-rich goethites in the upper sola. Our study shows that such differences between soils are influenced more due to distinct weathering conditions prevailing at the present time of their formation and the different parent materials than the exposure time of the surface.

References

Allard, T., Pereira, L., Mathian, M., Balan, E., Bueno, G.T., Falguères, C. Nascimento, N., 2020. Dating kaolinite from the Neogene Içá Formation and overlying laterites, Central Amazonia, Brazil: Constraints for a stratigraphic correlation. Palaeogeography, Palaeoclimatology, Palaeoecology 554, 109818. https://doi.org/10.1016/j.palaeo.2020.109818.

Ambrosi, J.P., Nahon, D., Herbilon, A.J., 1986. The epigenetic replacement of kaolinite by hematite in laterite. Petrographic evidence and the mechanisms involved. Geoderma 37, 283-294. https://doi.org/10.1016/0016-7061(86)90030-3.

Balan, E., Allard, T., Fritsch, E., Sélo, M., Falguères, C., Chabaux, F., Pierret, M., Calas, G., 2005. Formation and evolution of lateritic profiles in the middle Amazon basin: Insights from radiation-induced defects in kaolinite. Geochimica et Cosmochimica Acta 69, 2193–2204. https://doi.org/10.1016/j.gca.2004.10.028.

Balan, E., Fritsch, E., Allard, T., Calas, G., 2007. Inheritance vs neoformation of kaolinite during lateritic soil formation: a case study in the middle Amazon Basin. Clays Clay Miner. 55, 253-259. https://doi.org/10.1346/CCMN.2007.0550303..

Beauvais, A., 2009. Ferricrete biochemical degradation on the rainforest–savannas boundary of Central African Republic. Geoderma 150, 379–388. https://doi.org/10.1016/j.geoderma.2009.02.023.

Bilong, P., Belinga, S.E., Volkoff, B., 1992. Séquence d'évolution des paysages cuirassés et des sols ferrallitiques en zone forestière tropicale d'Afrique centrale. Place des sols à horizon d'argile tachetée. C. R. Acad. Sci. Paris 314, 109-115.

Cordani, U.G., Ramos, V.A., Fraga, L.M., Cegarra, M., Delgado, I., Souza, K.G., Gomes, F.E.M., Schobbenhaus, C., 2016. Tectonic map of South America=Mapa tectónico de América del Sur=Mapa tectônico da América do Sul. http://rigeo.cprm.gov.br/xmlui/handle/doc/16750. (accessed 23 August 2021)

Bitom, D., Volkoff, B.,1991. Mise en évidence de deux modes de microstructuration dans une couverture de sols ferrallitiques rouges du Sud-Cameroun. Science du Sol, 29, 289-300.

Braun, O.P.G., 1971. Contribuição à geomorfologia do Brasil Central. Revista Brasileira de Geografia 32, 3–39.

Brown, G., Brindley, G.W., 1980. X-ray diffraction procedures for clay minerals identification, in: Brindley, G.W., Brown, G. (Eds.), Crystal structures of clay minerals and their X-ray identification. Mineralogical Society, London, pp. 305–359.

Chauvel, A., Pedro, G., 1978a. Genèse de sols beiges (ferrugineux tropicaux lessivés) par transformation des sols rouges (ferrallitiques) de Casamance (Sénégal). Cah. ORSTOM, sér. Pédol. 16, 231-249.

Chauvel, A., Pedro, G., 1978b. Sur l'importance de l'extrême dessiccation des sols (ultra-dessiccation) dans l'évolution pédologiquedes zones tropicales à saisons contrastées. C. R. Acad. Sci.Paris, Ser. D 286, 1581–1584.

Chauvel, A., Soubies, F., Melfi, Al., 1983. Ferrallitic soils from Brazil: formation and evolution of structure. Sei. Géol., Mém. 72, 37 – 46.

CPRM - SERVIÇO GEOLÓGICO DO BRASIL. Mapa geológico do estado de Minas Gerais. Belo Horizonte: CPRM, 2014. Escala 1:1.000.000.

Curi, N., Franzmeier, D.P., 1984. Toposequence of Oxisols from the Central Plateau of Brazil. Soil Sci. Soc. Am. J. 48, 3411-346. https://doi.org/10.2136/sssaj1984.03615995004800020024x.

Didier, P., Nahon, D., Fritz, B., Tardy, Y., 1983. Activity of water as a geochemical controlling factor in ferricretes. a thermodynamic model in the system: kaolinite Fe-Al-oxihydroxides. Sci. Géol., Mérn. 71, 35 – 44.

Didier, P., Perret, D., Tardy, Y., Nahon, D., 1985. Equilibres entre kaolinites ferrifères, goethites alumineuses et hématites alumineuses dans les systèmes cuirasses rôle de l'activité de l'eau et de la taille des pores. Sci. Géol. Bull.38, 383-397.

Dixon, J.B., Weeds, S.B., 1989. Minerals in Soil Environments. Soil Science Society of America, Madison, WI.

FAO - Guidelines for Soil Description, 2006. Food and Agriculture Organization of the United Nations, fourth ed. Roma, Italy.

Ferreira, E.V.O., Martins, V., Inda Junior, A.V., Giasson, E., Nascimento. P.C., 2011. Ação dos térmitas no solo. Ciência Rural 41, 804-811. https://doi.org/10.1590/S0103-84782011005000044.

Ferreira, M.M., Fernandes, M., Curi, N., 1999. Mineralogia da fração argila e estrutura de Latossolos da região sudeste do Brasil. R. Bras. Ci. Solo 23, 507-514. https://doi.org/10.1590/S0100-06831999000300003.

Freitas, D.F., Ker, J.C., Silva Filho, L.A., Pereira, T.T.C., Souza, O.F.F., Schaefer, C.E.G.R., 2021. Pedogeomorphology and paleoenvironmental implications of large termite mounds at the Brazilian semiarid landscape. Geomorphology 387, 107762. https://doi.org/10.1016/j.geomorph.2021.107762.

Fritsch, E., Balan, E., Nascimento, N.R., Allard, T., Bardy, M., Bueno, G., Derenne, S., Melfi, A.J., Calas, G., 2011. Deciphering the weathering processes using environmental mineralogy and geochemistry: Towards an integrated model of laterite and podzol genesis in the Upper Amazon Basin. Comptes Rendus Geoscience 343, 188-198. https://doi.org/10.1016/j.crte.2010.11.002.

Fritsch, E., Montes-Lauar, C.R., Boulet, R., Melfi, A., Balan, E., Magat, P., 2002. Lateritic and redoximorphic features in a faulted landscape near Manaus, Brazil. Eur. J. Soil Sci. 53, 203-217. https://doi.org/10.1046/j.1351-0754.2002.00448.x

Fritsch, E., Morin, G., Bedidi, A., Bonnin, D., Balan, E., Caquineau, S., Calas, G., 2005. Transformation of haematite and Al-poor goethite to Al-rich goethite and associated yellowing in a ferralitic clay soil profile of the middle Amazon Basin (Manaus, Brazil). Eur. J. Soil Sci. 56, 575–588. https://doi.org/10.1111/j.1365-2389.2005.00693.x.

Furian, S., Barbiéro, L., Boulet, R., Curmi, P., Grimaldi, M., Grimaldi, C., 2002. Distribution and dynamics of gibbsite and kaolinite in an Oxisol of Serra do Mar, southeastern Brazil. Geoderma 106, 83-100. https://doi.org/10.1016/S0016-7061(01)00117-3.

Gee, G.W., Or, D., 2002. Particle Size Analysis, in: Dane, J.H., Topp, G.C., (Eds.), Methods of Soil Analysis, Part 4, Physical Methods, Soils Science Society of America, Book Series No. 5, Madison, pp. 255-293.

Girard, J.P., Freyssinet, P., Chazot, G., 2000. Unraveling climatic changes from intraprofile variation in oxygen and hydrogen isotopic composition of goethite and kaolinite in laterites: an integrated study from Yaou, French Guiana. Geochimica et Cosmochimica Acta 64, 409–426. https://doi.org/10.1016/S0016-7037(99)00299-9.

Gomes, J.B.V., Curi, N., Schulze, D.G., Marques, J.J.G.S.M., Ker, J.C., Motta, P.E.F., 2004. Mineralogia, morfologia e análise microscópica de solos do bioma cerrado. R. Bras. Ci. Solo 28, 679-694. https://doi.org/10.1590/S0100-06832004000400010.

Herbillon, A.J., 1980. Mineralogy of oxisols and oxic materials. In B.K.G. Theng (Eds.), Soils with Variable Charge. New Zealand Society of Soil Science, Lower Hutt. pp. 109–126.

Herbillon, A.J., Mestdagh, M.M., Vielvoye, L., Derouane, E.G., 1976. Iron in kaolinite with special reference to kaolinite from tropical soils. Clay Minerals 11, 201-220.

Herrmann, L., Anongrak, N., Zarei, M., Schuler, U., Spohrer, K., 2007. Factor and processes of gibbsite formation in Northern Thailand. Catena 71, 279-291. https://doi.org/10.1016/j.catena.2007.01.007.

Hinckley, D.N., 1963. Variability in "crystallinity" values among the kaolin deposits of the coastal plain of Georgia and South Carolina. Clays Clay Miner. 11, 229-235. https://doi.org/10.1346/CCMN.1962.0110122.

Hughes, J.C., Brown, G., 1979. A crystallinity index for soil kaolins and its relation to parent rock, climate and soil maturity. Journal of Soil Science, 30 557-563. https://doi.org/10.5433/1679-0375.2013v34n1p09.

IUSS Working Group WRB. 2015. World Reference Base for Soil Resources 2014, update 2015. International soil classification system for naming soils and creating legends for soil maps. World Soil Resources Reports No. 106. FAO, Rome.

Jackson, M.L., 1979. Soil chemical analysis - advanced course. Prentice-Hall, Madison.

Janot, C., Gilbert, H., 1973. Caractérisation de kaolinites ferrifères par spectrométrie Mössbauer. Bull. Soc. Fr. Minéral. Cristallogr. 96, 281-291. https://doi.org/10.3406/bulmi.1973.6830.

Jean, A., Beauvais, A., Chardon, D., Arnaud, N., Jayananda, M., Mathe, P.E., 2019. Weathering history and landscape evolution of Western Ghats (India) from $^{40}Ar/^{39}Ar$ dating of supergene K–Mn oxides. Journal of the Geological Society 23, 523-536. https://doi.org/10.1144/jgs2019-048.

Jouquet, P., Guilleux, N., Shanbhag, R.R., Subramanian, S., 2015. Influence of soil type on the properties of termite mound nests in Southern India. Applied Soil Ecology 96, 282–287. https://doi.org/10.1016/j.apsoil.2015.08.010.

Kämpf, N., Schwertmann, U., 1982. The 5 M NaOH concentration treatment for iron oxides in soils. Clays Clay Miner. 30, 40–408. https://doi.org/10.1346/CCMN.1982.0300601.

Karathanasis, A.D., 2008. Thermal Analysis of Soil Minerals, in: Ulery, A.L., Drees, L.R., (Eds.), Methods of Soil Analysis. Part 5. Mineralogical Methods, SSSA Book Series, Madison. pp. 161-190.

Ker, J.C., 2002. Latossolos do Brasil: uma revisão. Geonomos 5, 17-40. https://doi.org/10.18285/geonomos.v5i1.187.

King, L.C., 1956. A geomorfologia do Brasil oriental. Rev. Bras. Geogr. 18, 147–266.

Klug, H.P., Alexander, L.E., 1954. X-ray Diffraction procedures for polycrystalline and amorphous materials, second ed. John Wiley & Sons, New York.

Ledru, M.P., Braga, P.I.S., Soubies, F., Fournier, M., Martin, L., Suguio, K., Turcq, B., 1996. The last 50,000 years in the Neotropics (Southern Brazil): evolution of vegetation and climate. Palaeogeography, Palaeoclimatology, Palaeoecology 123, 239-57. https://doi.org/10.1016/0031-0182(96)00105-8.

Lepsch, I.F., Buol, S.W., 1988. Oxisol-landscape relationships in Brazil, in Beinroth, F.H., Camargo, M.N., Eswaran, H. (Eds.), Proceedings of the Eighth International Soil Classification Workshop, Brazil. Part 1: Papers. Soil Management Support Services, U.S. Dep. Agric., Washington, DC, pp. 174-189.

Macedo, J., Bryant, R.B., 1987. Morphology, Mineralogy, and Genesis of a Hydrosequence of Oxisols in Brazil. Soil Sci. Soc. Am. J. 51, 690-698. https://doi.org/10.2136/sssaj1987.03615995005100030025x.

Marques, J.J., Schulze, D.G., Curi, N., Mertzman, S.A., 2004. Major element geochemistry and geomorphic relationships in Brazilian Cerrado soils. Geoderma 119, 179-195. https://doi.org/10.1016/S0016-7061(03)00260-X.

Marques, K.P.P., Santos, M., Peifer, D., Silva, C.L., Vidal-Torrado, P., 2021. Transient and relict landforms in a lithologically heterogeneous post-orogenic landscape in the intertropical belt (Alto Paranaíba region, Brazil). Geomorphology 391, 107892. https://doi.org/10.1016/j.geomorph.2021.107892.

Mathian, M., Aufort, J., Braun, J., Riotte, J., Selo, M., Balan, E., Fritsch, E., Bhattacharya, S., Allard, T., 2019. Unraveling weathering episodes in Tertiary regoliths by kaolinite dating (Western Ghats, India). Gondwana Research 69, 89-105. https://doi.org/10.1016/j.gr.2018.12.003.

Mathian, M., Bueno, G.T., Balan, E., Fritsch, E., Nascimento, N.R., Selo, M., Allard, T., 2020. Kaolinite dating from Acrisol and Ferralsol: A new key to understanding the landscape evolution in NW Amazonia (Brazil). Geoderma 370, 114354. https://doi.org/10.1016/j.geoderma.2020.114354.

Mehra, O.P., Jackson, M.L., 1960. Iron oxide removal from soils and clay by a dithionitecitrate system buffered with sodium bicarbonate. Clays Clay Miner. 7, 317–327. https://doi.org/10.1016/B978-0-08-009235-5.50026-7.

Melo, V.F., Oliveira Jr., J.C., Batista, A.H., Cherobim, V.F., Favaretto, N., 2020. Goethite and hematite in bichromic soil profiles of southern Brazil: xanthization or yellowing process. Catena 188, 104445. https://doi.org/10.1016/j.catena.2019.104445.

Melo, V.F., Wypych, F., 2009. Caulinita e Haloisita, in: Melo, V.F., Alleoni, L.R.F. (Eds.), Química e Mineralogia do Solo. Viçosa, MG: Sociedade Brasileira de Ciência do Solo, pp. 427-504.

Melo, V.M., Singh, B., Schaefer, C.E.G.R., Novais, R.F., Fontes, M.P.F., 2001. Chemical and mineralogical properties of kaolinite-rich Brazilian soils. Soil Sci. Soc. Am. J. 65, 1324–1333. https://doi.org/10.2136/sssaj2001.6541324x.

Mitra, G.B. 1963. Structure defects in kaolinite. Z. Kristallog. 119, 161-75. https://doi.org/10.1524/zkri.1963.119.3-4.161.

Monteiro, H.S., Vasconcelos, P.M.P., Farley, K.A., 2018. A combined (U-Th)/He and cosmogenic ^{3}He record of landscape armoring by biogeochemical iron cycling. Journal of Geophysical Research: Earth Surface 123, 298–323. https://doi.org/10.1002/2017JF004282.

Motta, P.E.F., Carvalho Filho, A., Ker, J.C., Pereira, N.R., Carvalho Junior, W., Blancaneaux, P., 2002. Relações solo-superfície geomórfica e evolução da paisagem em uma área do Planalto Central Brasileiro. Pesquisa Agropecuária Brasileira 37, 869–878. https://doi.org/10.1590/S0100-204X2002000600017.

Muggler, C.C., Buurman, P., Doesburg, J.D.J., 2007. Weathering trends and parent material characteristics of polygenetic Oxisols from Minas Gerais, Brazil: I. Mineralogy. Geoderma 138, 39-48. https://doi.org/10.1016/j.geoderma.2006.10.008.

Muller, J., 1982. De la nécessité d'établir une taxonomie objective des sols ferrallitiques sur des bases phylogénétiques. Cah. O.R.S.T.O.M., sér. Pédol. 19, 43-49.

Muller, J.P., 1972. Étude macromorphologique de sols ferrallitiques appauvris en argile du Gabon. Cah. ORSTOM, sér. Pédol. X, 77-93.

Nahon, D., 1986. Evolution of iron crusts in tropical landscapes, in: Colman, S.M., Dethier, D.P. (Eds.), Rates of Chemical Weathering of Rocks and Minerals. Academic Press, New York, pp. 169-191.

Nahon, D., 2003. Altérations dans la zone tropicale. Signification à travers les mécanismes anciens et/ou encore actuels. C. R. Geoscience 335, 1109-1119. https://doi.org/10.1016/j.crte.2003.10.008.

Nahon, D., Tardy, Y., 1992. The ferruginous laterites, in: Butt, C.R.M., Zeegerds, H. (Eds.), Regolith exploration geochemistry in tropical and subtropical terrains. Handbook of exploration geochemistry. Elsevier, Amsterdam, pp. 41-55.

Norrish, K., Taylor, M., 1961. The isomorphous replacement of iron by aluminium in soil goethites. J. Soil Sci. 12, 294–306. https://doi.org/10.1111/j.1365-2389.1961.tb00919.x.

Oliveira, P.E., Raczka, M., McMichael, C.N.H., Pinaya, J.L.D., Bush, M.B., 2020. Climate change and biogeographic connectivity across the Brazilian cerrado. Journal of Biogeography 47, 396-407. https://doi.org/10.1111/jbi.13732.

Pessenda, L.C.R., Ramon Aravena, Melfi, A.J., Telles, E.C.C., Rene Boulet, Valencia, E.P.E., Tomazellos, M., 1996.The use of carbon isotopes (^{13}C, ^{14}C) in soil to evaluate vegetation changes during the Holocene in Central Brazil. Radiocarbon 38, 191-201. https://doi.org/10.1017/S0033822200017562.

Plançon, A., Giese, R.F., Snyder, R., 1988. The Hinckley Index for kaolinites. Clay Minerals 23, 249-260. https://doi.org/10.1180/claymin.1988.023.3.02.

Queiroz de Carvalho, J.B., 1983. Proposed method to assess the degree of crystallinity of kaolinite in lateritic soils, in: Melfi, A.J., Carvalho A. (Eds.), Lateritisation Processes, 2nd International Seminar on Lateritisation Processes, São Paulo, Brazil, pp. 563-568.

Reatto, A., Bruand, A., Martins, E.S., Muller, F., Silva, E.M., Carvalho Jr., O.A., Brossard, M., 2008. Variation of the kaolinite and gibbsite content at regional and local scale in Latosols of the Brazilian Central Plateau. C. R. Geoscience 340, 741–748. https://doi.org/10.1016/j.crte.2008.07.006.

Rolim Neto, F.C., Schaefer, C.E.G.R., Fernandes Filho, E.I., Corrêa, M.M., Costa, L.M., Parahyba, R.B.V., Guerra, S.M.S., Heck, R., 2009. Topolitossequências de solos do Alto Paranaíba: atributos físicos, químicos e mineralógicos. Revista Brasileira de Ciência do Solo 33, 1795-1809. https://doi.org/10.1590/S0100-06832009000600028.

Santos, H.G., Jacomine, P.K.T., Anjos, L.H.C., Oliveira, V.A., Lumbreras, J.F., Coelho, M.R., Almeida, J.A., Araújo Filho, J.C., Oliveira, J.B., Cunha, T.J.F., 2018. Sistema Brasileiro de Classificação de Solos, fifth ed. Embrapa Solos, Rio de Janeiro, 2018.

Santos, R.D., Lemos, R.C., Santos, H.G., Ker, J.C., Anjos, L.H.C., 2015. Manual de descrição e coleta de solo no campo. Sociedade Brasileira de Ciência do Solo: Viçosa.

Schulze, D.G., 1984. The influence of aluminium on iron oxides. VIII – unit-cell dimensions of Al-substituted goethites and estimation of Al from them. Clays Clay Miner. 32, 36-44. https://doi.org/10.1346/CCMN.1984.0320105.

Schwertmann, U., Fitzpatrick, R.W., Taylor, R.M., Lewis, D.G., 1979. The influence of aluminum on iron oxides. Part II. Preparation and properties of Al-substituted hematites. Clays Clay Miner. 27, 105–112. https://doi.org/10.1346/CCMN.1979.0270205.

Singh B., Gilkes, R.J., 1992. Properties of soil kaolinites from south-western Australia. Journal of Soil Science 43, 645-667. https://doi.org/10.1111/j.1365-2389.1992.tb00165.x.

Singh, B., Gilkes, R.J., 1991. Concentration of iron oxides from soil clays by 5 M NaOH treatment: The complete removal of sodalite and kaolin. Clay Miner. 26, 463–472. https://doi.org/10.1180/claymin.1991.026.4.02.

Smykatz-Kloss, W., 1974. Differential Thermal Analysis Application and Result in Mineralogy. Springer Verlag Berlin Heidelberg, New York.

Soil Survey Staff, 2014. Keys to Soil Taxonomy, 12th ed. USDA National Resources Conservation Services, Washington DC.

Tardy, Y., Kobilsek, B., Paquet, H., 1991. Mineralogical composition and geographical distribution of African and Brazilian periatlantic laterites. The influence of continental drift and tropical paleoclimates during the past 150 million years and implications for India and Australia. Journal of African Earth Sciences 12, 283-295. https://doi.org/10.1016/0899-5362(91)90077-C.

Tardy, Y., Nahon, D., 1985. Geochemistry of laterites, stability of Al-goethite, Al-hematite and Fe^{3+}-kaolinite in bauxites and ferricretes: an approach of the mechanism of concretion formation. Am. J. Sci. 285, 865-903.

Tardy, Y., Roquin C., 2000. Dérive des continents: paléoclimats et distribution des couvertures pédologiques tropicales. Bull. Assoc. Géogr. Franç. 77, 373-383. https://doi.org/10.3406/bagf.2000.2185.

Teixeira, P.C., Donagemma, G.K., Fontana, A., Teixeira, W.G., 2017. Manual de Métodos de Análise de Solo, third ed. Embrapa Solos, Rio de Janeiro.

Torrent, J., Cabedo, A., 1986. Sources of iron oxides in reddish brown soil profiles from calcarenites in Southern Spain. Geoderma 37, 57–66. https://doi.org/10.1016/0016-7061(86)90043-1.

Trolard, F., Tardy, Y., 1987. The stabilities of gibbsite, boehmite, aluminous goethites and aluminous hematites in bauxites, ferricretes and laterites as a function of water activity, temperature and particle size. Geochimca et Cosmochimica Acta 51, 945-957. https://doi.org/10.1016/0016-7037(87)90107-4.

Trolard, F., Tardy, Y., 1989. A modelo f Fe^{3+}-kaolinite, Al^{3+}-goethite, Al^{3+}-hematite equilibra in laterites. Clay Minerals 24, 1-21.

Vasconcelos, P.M., Farley, K.A., Stone, J., Piacentini, T., Fifield, L.K., 2019. Stranded landscapes in the humid tropics: Earth's oldest land surfaces. Earth and Planetary Science Letters 519, 152–164. https://doi.org/10.1016/j.epsl.2019.04.014.

Vernet, J., Wengler, L., Solari, M., Ceccantini, G., Fournier, M., Ledru, M., Soubiès, F., 1994. Feux, climats et végétations au Brésil central durant l'Holocène: les données d'un profil charbons de bois (Salitre, Minas Gerais). C.R. Acad. Sci. Paris 319, 3918-1397.

Vidal-Torrado, P., Lepsch, I.F., Castro, S.S., Cooper, M., 1999. Pedogênese em uma sequência Latossolo-Podzólico na borda de um platô na Depressão Periférica Paulista. R. Bras. Ci. Solo 23, 909-921. https://doi.org/10.1590/S0100-06831999000400018.

Walkley, A.J. Black, I.A., 1934. Estimation of soil organic carbon by the chromic acid titration method. Soil Sci. 37, 29-38.

Watanabe, T., Funakawa, S., Kosaki, T., 2006. Clay mineralogy and its relationship to soil solution composition in soils from different weathering environments of humid Asia: Japan, Thailand and Indonesia. Geoderma 136, 51-63. https://doi.org/10.1016/j.geoderma.2006.02.001.